Carbon nanotube based composite thin film coatings for stray light control space applications

A Thesis submitted

in partial fulfillment for the Degree of

Doctor of Philosophy

By

Sonia Saini

SC16D023

Department of Physics

Indian Institute of Space Science and Technology

Thiruvananthapuram, India

January 2024

CERTIFICATE

This is to certify that the thesis entitled **Carbon nanotube based composite thin film coatings for stray light control space applications** submitted by **Sonia Saini** to the Indian Institute of Space Science and Technology Thiruvananthapuram, in partial fulfilment for the award of the degree of **Doctor of Philosophy** is a *bona fide* record of research work carried out by her under my supervision. The contents of this thesis, in full or in parts, have not been submitted to any other Institution or University for the award of any degree or diploma.

Dr. Kuntala Bhattacharjee
Supervisor
Associate Professor
Department of Physics

Prof. Sudheesh Chethil
Head of Physics department

Place Thiruvanthapuram
Date January 2024

DECLARATION

I declare that this thesis entitled **Carbon nanotube based composite thin film coatings for stray light control space applications** submitted in partial fulfilment of the degree of **Doctor of Philosophy** is a record of original work carried out by me under the supervision of Dr. Kuntala Bhattacharjee, and has not formed the basis for the award of any other degree or diploma, in this or any other Institution or University. In keeping with the ethical practice of reporting scientific information, due acknowledgments have been made wherever the finding of others have been cited.

Place Thiruvanthapuram
Date January 2024

Sonia Saini
SC16D023

This thesis is dedicated to Lord Shri Krishna for giving me determination and strength.

Acknowledgement

As I approach the culmination of my thesis, I want to take a moment to convey my deepest appreciation and gratitude to my grandparents (Shri Sadhu Ram ji, Smt. Bhagwanti ji), parents (Shri Khem Chand Saini ji and Smt. Sudesh Rani), my brother Mr. Sandeep Saini, my sister-in-law Smt. Shashi Saini and the kids Ms. Prisha Saini and Ms. Kriva Saini. Their unwavering love, support, and belief in me have been the driving force behind my academic journey, and I am eternally thankful for their presence in my life. Originating from Kurukshetra (the land of Mahabharata), a land steeped in rich traditions and fortified values, they have instilled within me a profound sense of determination and resilience. Through their upbringing, I have learned the intrinsic value of hard work, perseverance, and the relentless pursuit of knowledge. I am profoundly grateful for the sacrifices they have made to provide me with the finest opportunities. Their tireless efforts to ensure that I received a quality education have indelibly shaped my academic trajectory, opening doors to a world full with endless possibilities. Their untiring faith in my abilities has been the motivation, driving my academic achievements. I carry with me the invaluable lessons and teachings from Kurukshetra. As I acknowledge Kurukshetra as the land of Mahabharata, I am filled with a deep sense of respect for the cultural and historical significance it holds. It serves as a constant reminder of the timeless wisdom and profound teachings of Gita (the blessed melody performed by Shri Krishna for Arjuna) that have shaped my consciousness and continue to resonate with me today.

I am sincerely grateful to my uncle, Shri Avatar Saini, for his firm support in my decision-making process and constant encouragement to push my limits. I am thankful to my cousins Mr. Rahul Saini and Mr. Bhushan Saini for having strong faith in my academic journey.

From my school days, I want to express my heartfelt gratitude to Mr. Neeraj Taneja (my science and mathematics' teacher) for his guidance and support during my school years. I appreciate Mr. Yash Pal Wadhwa for supporting and encouraging to participate in various extracurricular activities as well.

I'm thankful to Dr. Jaspal Hooda (my Physics mentor during 12th) whose commitment to nurturing young minds and ability to explain complex concepts with clarity have laid a strong foundation for my scientific pursuits.

I want to take a moment to extend my gratitude to Dr. Manju Singh and Mrs. Neelam Lamba (my Chemistry professors during B.Sc.) for their invaluable contribution to my academic journey. Their commitment to teaching and expertise in the field have been a constant source of inspiration. I pay a grateful gesture to Mrs. Renu Mehta and Mrs. Meenu Sharma (my Physics professors during B.Sc.) who consistently encouraged me to explore beyond the confines of traditional textbook learning and guided me towards embracing the challenges and joys of conducting experiments.

I express my deep appreciation to Dr. Amarjeet Singh, Dr. Vibhav Saraswat, Dr. Vimal Vyas and Dr. Saral Kumar Gupta for their unbiased support and guidance during my master's program

I express my heartfelt gratitude to Director IIST, Dr. S. Unnikrishnan Nair, Prof V.K. Dhadwal (Former Director), for their invaluable academic support. I extend my sincere appreciation to Prof. S Murugesh (Former Head of the Physics department) and Prof. Umesh Kadhane (Former Head of the Physics department) for their unwavering support and encouragement. I am grateful to the Head of the Physics department, Prof. Sudheesh Chethil for providing overall support.

I would like to extend my gratitude to Dr. Reshmi S., my senior. Her expertise, and mentorship have played a crucial role in shaping the trajectory of my research, and I am deeply grateful for her presence in my academic life. I am very thankful to Mr. Manu Mohan for being a supportive friend. My special thanks to Dr. Preetam Hazra and Mr. Dayal G Krishna for supporting during crucial times always.

I would like to express my sincere appreciation to my IIST friends specially Dr. Mahindra Singh Rautela, Dr. Rashi Jain and Mr. Pranav Nath for their friendship. I am honored to have such wonderful friends as part of my support system.

I express gratitude to my beloved brother, Mr. Amit Saini, for his valuable support during the challenging academic demands. His profound belief in my journey and unconditional

love have been precious. I extend my thanks to my brother Mahavir Saini and appreciate his support.

I express deep gratitude to Mr. Jiju John and Dr. M S Giridhar, scientists at the Laboratory for Electro-Optics Systems (LEOS); Indian Space Research Organization (ISRO), for their invaluable support and assistance during the course of my research. Their contribution in providing the necessary items and facilities has been instrumental in the successful completion of this thesis. I am deeply grateful to Mrs. Ashwini and Dr. Sumesh for their outstanding support at LEOS. I am thankful to Ms. Madhu Malthi for her courageous presence around. I am incredibly fortunate to have a friend like Ms. Debashree Das, who not only understands the challenges of pursuing a Ph.D. but also goes above and beyond to offer unwavering support. I want to convey my appreciation to my friends at LEOS, especially to Mr. Pratheek T K and Mr. Satish Kumar, for sharing wonderful moments of togetherness and genuine expressions of friendship.

The carbon nanotube based research work was taken up by Dr. Girish Manjunath Gouda, Scientist at LEOS-ISRO for the space applications during the year 2016-2017. My PhD supervisor Dr. Kuntala Bhattacharjee, advised me to involve in this R & D activity at LEOS based on the interactions with Dr. Girish Gouda. The activity was in the initial stages of development and I started working on single wall carbon nanotube based coatings at LEOS. I heartly thank Dr. Girish Gouda (currently Head of Thin Films Division), who helped me throughout the activity at LEOS in terms of arranging the required infrastructure, characterization facilities and setting up the laboratory dedicated to the activity. His overall support and commitment to fostering research significantly enhanced the quality of my work and helped me achieve my research objectives and successful completion of this thesis.

I am grateful to Mr. Ajit Kumar (former Head of Thin Film Division), Mr. Viswanathan (former Group Director, TMDG-LEOS), Mr. A S Lakshmiprasad (former Director LEOS) and Dr. K V Sriram (Director of LEOS), for allowing my research activity at LEOS.

I would like to express my heartfelt appreciation to my Ph.D. guide, Dr. Kuntala Bhattacharjee, for her invaluable guidance throughout the duration of my doctoral research. Her expertise, dedication, and mentorship have been instrumental in shaping my academic and research journey. I am truly grateful to Dr. Kuntala Bhattacharjee for her profound knowledge, insightful feedback, and constructive criticism that have consistently pushed me to reach new heights in my research endeavors. Her commitment to excellence and passion for the subject matter have been a constant source of inspiration. I am indebted to her for her patience, encouragement, and belief in my abilities, which have provided me with the confidence to overcome challenges and persevere in the face of obstacles. Her mentorship has not only enhanced my research skills but also nurtured my personal and professional growth.

I am grateful to Prof. Shikha Varma and all other doctoral committee members for investing their valuable time and providing constructive remarks.

I express heartfelt gratitude to Prof. Karuna Kar Nanda, Director of Institute of Physics (IOP) for all the essential support. My special thanks to authorities of IOP to provide hostel accommodation and research environment. I genuinely value the presence of Prof. Sudipto Mukherji for the delightful and joyous moments at IOP. I am thankful to Prof Biju Raja Sekhar for interactive sessions. I appreciate Scientist Asst. Ms. Ajita K Kujur for consistently supporting me during library study hours and throughout campus life with care.

Lastly, I would like to express my deepest appreciation to my advisors, mentors, colleagues, and friends, whose guidance and encouragement have been indispensable throughout this endeavor.

Sonia Saini

Contents

List of Figures

2.5. Fullerene cap removal and defect generation for an ideal SWCNT during functionalization process.

2.6.(a) Covalent and non-covalent functionalization processes description. (b) Absorption via covalent and (c) Adsorption via non-covalent bonding mechanism.

2.7.CNT bundle acid treatment (a) Intratube MWCNT depletion by ions (b) Intertube intercalation process into bundles leading to graphitic sheets oxidation by axial and longitudinal tearing.

2.8. Molecular pictorial diagram of functionalization and polymer grafting processes of fullerene capped ideal SWCNT.

3.1. Configuration of the FTIR spectroscopy instrument (image courtesy: https://www.jasco-global.com).

3.2.(a) Depicts the XPS experimental setup configuration (image courtesy: https://grimmgroup.net/), (b) Presents a fundamental diagram illustrating the principle of XPS (image courtesy: https://www.ifw-dresden.de/).

3.3.(a) Illustrates the configuration of the Raman experimental setup (imagecourtesy:https://chem.libretexts.org/), while (b) Provides a basic diagram explaining the principle of Raman spectroscopy (imagecourtesy:non-invasive glucose sensing with Raman spectroscopy, Wei-Chuan Shih et al.).

3.4.(a) Setup configuration for XRD experiment (image courtesy: X-ray diffraction (XRD) of nanoencapsulated food ingredients, Seid Reza Falsafi et al.), while (b) Fundamental diagram elucidating the principle of XRD (image courtesy: https://wiki.anton-paar.com/).

3.5. Schematic of a typical SEM set up (image courtesy: https://www.technoorg.hu/).

3.6. Experimental configuration for conducting AFM experiment (image courtesy: https://lnf-wiki.eecs.umich.edu/).

3.7.A schematic representation of the experimental setup of HRTEM with an ion gun (image courtesy: in situ transmission electron microscope observation of the formation of fuzzy structures on tungsten, M Miyamoto et al.).

3.8. Design of a 150 mm integrating sphere for optical measurements. (image courtesy: https://www.mri.psu.edu/).

4.1. Schematic of the purification process. (a) Flow chart depicting the process step by step, and (b) pictorial presentation of the oxidative attachment of the functional groups on the side walls of the CNTs and the related chemical equations involved during the purification process.

4.2. Schematic of cracking of carbon shell surrounding FeNPs by wet oxidation and removal of FeNPs and amorphous carbon transforming into a soluble ferric salt after HCl treatment.

4.3. Schematic representation of the functionalization and polymer grafting processes. The attachment of carboxyl group ($-COOH$) after the functionalization, is followed by polymer grafting process with hydrocarbon chains, $-(M-M)_n$.

4.4. Schematic representing of different stages of coating process and (b) image of in-situ hand spray coating process.

4.5. Flow chart of the work methodology followed in the study.

5.1. FTIR spectra of purified and functionalized samples. Both the spectra are normalized w.r.t. the maximum intensity of the purified sample data.

5.2. High resolution XPS spectra (a) $C1s$ and (b) $O1s$ for purified sample. (c) $C1s$, (d) $O1s$ for the functionalized sample.

5.3. XRD spectrum of the as-prepared sample.

5.4. XRD data of (a) purified, (b) functionalized and (c) coated film.

5.5. Raman spectra of as-prepared HiPCO SWCNT sample representing prominent characteristics of RBM and G peaks along with low peak feature of D band.

5.6. Raman spectra of (a) purified (b) functionalized and (c) coated film. The spectra are normalized with respect to the G peak of the purified data shown in (a).

5.7. (a) RBM vibrations directed radially outwards and (b) in-plane vibrations of G-band in SWCNTs.

5.8. D and G mode vibrations in (a) purified, (b) functionalized and (c) coated samples. The intensity of the spectra was normalized with respect to the G peak of the purified data shown in (a).

5.9. Peak fit of Raman D and G band of purified, functionalized and coated SWCNT film using Lorentz profiles. The intensity of the spectra is normalized w.r.t. the G peak of the purified data.

5.10. Peak fit of Raman D and G band of purified, functionalized and coated film using a combination of Lorentz and BWF line shapes. The intensity of the spectra is normalized w.r.t. the G peak of the purified data.

5.11. Lorentz approximated Raman $2D$ band of purified, functionalized and coated film. The intensity of the spectra is normalized w.r.t. the G peak of the purified data.

5.12. Low-frequency Raman spectra from (a) functionalized and (b) coated samples. The intensity of both spectra was normalized with respect to the G peak of the purified data.

6.1. TEM micrographs obtained from the as-prepared SWCNT sample. (a) Shows the large area image with bundled networks of SWCNTs. Amorphous carbonaceous particles are marked in (a) using arrows. (b) (c) and (d) show clear evidence of SWCNTs (marked with white arrows) within the bundled network. Presence of metal nanoparticles are observed as dark spots in (b-d).

6.2. (a) TEM image showing SWCNT strands of varying diameters in purified sample. The regions of different diameter periodicities are marked using white rectangles on the image. (b) Shows the line profiles taken across each such rectangular region. Diameter periodicity of the SWCNT bundles within the rectangles is marked in the profiles. (c) Evidence of SWCNTs in the bundles and (d) FFT of the SWCNT bundle shows the hexagonal symmetry of the *sp*2 hybridized carbon atoms.

6.3. TEM investigations of the purified sample. (a) Large-scale image showing sparse bundle network of SW and MW CNTs with rare presence of impurity particles. (b) MWCNTs from the marked area in (a). (c) Presence of MWCNTs with varying diameters (marked within black squares). (e) High-resolution TEM image of an MWCNT with graphitic (002) plane stacking. The (002) layer spacing of ~0.34 nm is marked in (e). Inset of (e) is the FFT from the selected area [marked as a rectangle in the image].

6.4. TEM investigations of the purified sample. Gross reduction in catalytic metal nanoparticles after a systematic purification process is observed. (a) and (b) Catalytic tearing induced by metal nanoparticles in the SWCNT bundles shown by white arrows; (c) curling of SWCNTs; and (d) evidence of ring formation.

6.5. (a)–(c) TEM micrographs depicting formation of CNS from GS. (d) Cross-sectional view of CNS revealing rolling of GS inside.

6.6. (a and b) Catalyst metal nanoparticle induced axial tearing of CNS. (c) Stress and strain induced tearing of CNS.

6.7. (a)-(c) TEM images of merging of SWCNT bundles. (d) Periodicities of the merged SWCNTs.

6.8. The presence of SWCNT bundles (a, b) and MWCNTs (c, d) in the functionalized data. Twisted SWCNT bundles can be seen in (a). SWCNTs with enlarged diameter (b). Attachment of functional groups is visible as protrusions on the walls of the nanotubes [marked by arrows, (c), (d)].

6.9. TEM micrographs of the functionalized sample. (a) Evidence of GS and CNS. (b) MWCNTs with amorphous side walls. (c) Longitudinal exfoliation of SWCNT bundles and formation of `Y' like junctions. (d, e) Nanoscrolls which are short after conducting the functionalization process and

List of Tables

Abstract

Research on carbon materials such as carbon nanoscrolls (CNS), graphitic sheets (GS), carbon nanotubes (CNTs) etc. based thin films with low light reflectance has received paramount importance in order to have high absorber coatings for stray light control applications. CNS, a one dimensional (1D) helical form of carbon has received enormous attention recently due to their unique structure, superior properties and potential applications. In this work, radial merging of high pressure carbon monoxide (HiPCO) single-walled carbon nanotube (SWCNT) bundles and emergence of CNS are reported following a reflux action involving wet oxidation, HCl wash and annealing at 900°C. We also report a successful demonstration of developing stable thin films comprised of carbon nanomaterials on the aluminium (Al) substrate which exhibits low reflectance of the order of 2-3% in the visible and near-infrared (NIR) spectral band. Changes in structural and chemical compositions to the originally procured SWCNT samples have been analyzed after each subsequent processing step. Spectroscopy, microscopy and microstructural studies demonstrate the emergence of CNS and multi-walled carbon nanotubes (MWCNTs) in the samples due to the sequential chemical processing of the sample. Here, a simple solution based oxidative route for successful merging and exfoliation of SWCNT bundles and subsequent formation of CNS are demonstrated and discussed in view of Fourier transform infrared (FTIR) spectroscopy, X-ray photoelectron spectroscopy (XPS) and transmission electron microscopy (TEM) studies. TEM and scanning electron microscopy (SEM) studies reveal the formation of CNS via curling and folding of the graphene sheets. Microstructural investigations like SEM and atomic force microscopy (AFM) confirm the evidence of microcavities and pores on the film surface. These cavities and pores contribute significantly to the observed low reflectance value of the CNT, CNS compound films by trapping the incident light. Fundamental space environmental simulation tests (SEST) performed on the coated films show promising results with reflectance values almost unaltered in the visible and NIR spectral band which demonstrate the durability of these films as potential candidates to be used in extreme space environmental conditions. The paper describes the preparation, characterization, and testing of the blended CNT and CNS coatings for low-light scatter applications. Direct evidence of emergence of CNS from SWCNTs via synthesis of GS through a simple oxidative is reported for the first time.

CHAPTER 1

INTRODUCTION

This chapter discusses the importance of the carbon nanotubes (CNTs) and other low dimensional structural derivatives of carbon and provides an overview of the work carried out in this thesis. Exceptional properties of carbon nanomaterials which make them highly promising for a diverse array of technological applications including stray light control space research is addressed.

1.1. Overview of literature

Invention of carbon nanotubes (CNTs) by S. Iijima [1] is one of the most important experimental events that has changed the dynamics of the nanomaterials research completely, both in fundamental and applied fronts. Currently, CNTs serve human kind by providing a range of applications in different fields including biomedical to energy storage [2–4]. The first evidence of the existence of CNTs was noticed in 1952, when two Russian scientists, L. V. Radushkevich and V. M. Lukyanovich observed clear images of carbon nanofilaments of 50 nm diameter [5]. However, this discovery went unnoticed as it was published in Russian in a journal with limited circulation. Similar studies were also carried out by Bacon et al. [6,7], Howard G. Tennent et al. [8]. In 1991, the experimental evidence of multi walled carbon nanotubes (MWCNTs) was observed by Japanese scientist, S. Iijima, during his transmission electron microscopy (TEM) studies [1]. He defined them as allotropes of carbon with a hollow cylindrical-tube-shaped structure. Later on, during 1993, Iijima et al. [9], and Bethune et al. [10] independently detected single walled carbon nanotubes (SWCNTs). The helical arrangement of carbon hexagons in CNTs was studied using electron diffraction by Iijima et al. [11]. P. M. Ajayan et al. [12] focused on purification methods of the CNTs and introduced various oxidation techniques to make these inert one-dimensional (1D) structures active and applicable. Fully collapsed CNTs as ribbons or flatten tubes were observed due to localized stress and strain resulting into kinked or twisted structures under external mechanical forces [13].

Iijima's groundbreaking discovery [1] holds immense significance, as it brought CNTs to the forefront of the entire scientific community's attention. Since then, research on CNTs has accelerated and have been investigated in diverse fields and areas. The uniqueness of these materials resides in their structure-dependent properties, which can be adjusted by altering and controlling the architecture either during the synthesis process or through post-synthesis methods, depending on specific needs and applications.

CNTs, classified in two different forms as single walled (SW) and multi walled (MW), are rolled graphene structures comprised of sp^2 hybridized hexagonal carbon atom lattice known for its significant surface area and very large diameter-to-length aspect ratio [14].

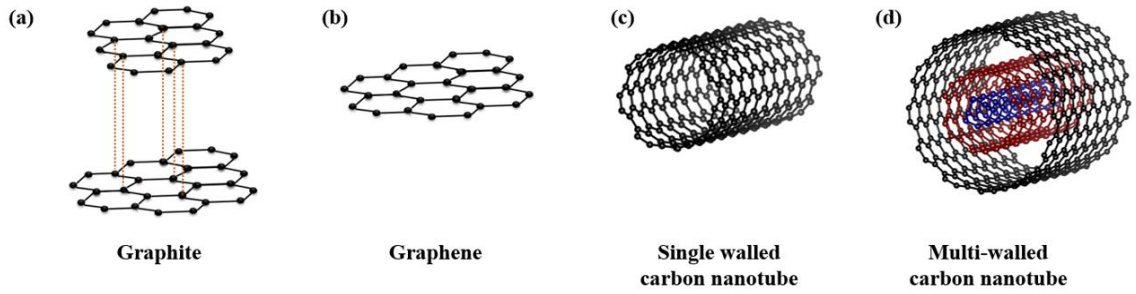

Figure 1.1: Schematic representation of CNTs emerging from graphite (a) graphite comprised of two layers of graphene, (b) single layer graphene, (c) SWCNT, and (d) MWCNT.

A SWCNT is a hollow long cylinder of a graphite sheet, whereas a MWCNT is a group of coaxial SWCNTs shown in Figure 1.1 [15]. However, in reality, a perfectly formed nanotube composed of solely a hexagonal network is unattainable due to the presence of pentagonal and heptagonal structures at the points of curvature and bends in the atomic arrangement of carbon atoms. The hexagonal network of a nanotube typically consists of both three σ and one π orbital structures within the plane [16]. The curvature or turning points in the nanotube's configuration cause a redistribution of π-electrons, which promotes the rehybridization of σ-π bonds [16]. This, in turn, causes a slight shift of the mixed electron cloud out-of-plane, resulting in greater electron delocalization. This curvature effect leads to quantum confinement and the formation of capped structures over the ends of CNTs, which incorporate topological irregularities like pentagons and heptagons within the hexagonal lattice [16]. These enclosed structures confer greater mechanical strength and heightened electrical, thermal, chemical, and biological reactivity when compared to graphite [15], [17].

One of the most coveted applications of CNTs and other graphitic materials is their utility as black absorber coatings for stray light mitigation in baffles/vanes, and as traps to

blackbodies and thermal detectors. The parasitic background signal, coming from numerous sources in any optical devices affects the proper functioning of the component. The CNTs and other low dimensional structural hybrids of carbon that are characterized by uniform low reflectance over a broad spectral range are considered the best suitable candidates for stray light control applications. The nature of the blackest coatings relies not only on the intrinsic properties of these structures but also on the morphology, light-trapping ability, density, thickness and disorder in the coated films. The physics of such coatings can be well described by considering a medium with an index near unity so that incoming light is not immediately reflected and there is sufficient depth for light photons to be absorbed eventually.

The work presented in this thesis addresses the optical nature of the stable thin film coatings comprised of random network of functionalized low dimensional structural derivatives of carbon and polymer conjugate for stray light control space applications. The optical nature of CNTs and graphene is well studied, however, for sustainable stray light control space applications, we required a facile, cost-effective technique to fabricate carbon thin film coatings. This was performed by considering high pressure carbon monoxide (HiPCO) SWCNTs as a building block to synthesize different carbon nanomaterials such as MWCNTs, graphene sheets (GS), carbon nanoscrolls (CNS), twisted CNTs and `Y' and `T' junctions. We chose SWCNTs over MWCNTs due to the fact that SWCNTs consist of just one layer of graphene sheets that is easier for chemical modifications and tailoring the properties. MWCNTs with their multiple walls, exhibit greater structural stability and as a result, functionalization becomes comparatively difficult. Intercalation is mostly employed to bind the functional groups into the MWCNTs [18], [19]. That is why we preferred to work with SWCNTs.

Structure and properties of different carbon nanomaterials are briefly discussed below.

1.2. Structure

1.2.1. Graphene

Graphene is typically perceived as a two-dimensional (2D) nanostructure, characterized by a flat sheet composed of carbon atoms arranged in a hexagonal or honeycomb lattice. It serves as the fundamental building block for a range of other carbon allotropes of zero, one, and three dimensional (0D, 1D, and 3D). To illustrate, it can be folded into spherical fullerenes (0D), rolled into cylindrical CNTs and CNS (1D), or layered to form graphite (3D). The molecular arrangement of graphite involves multiple layers of graphene, each of which is made up of a hexagonal lattice of sp^2 hybridized carbon atoms that are firmly bonded together by covalent bonds [16]. The bonds connecting the layers are characterized by weak van der Waals (vdWs) forces [16].

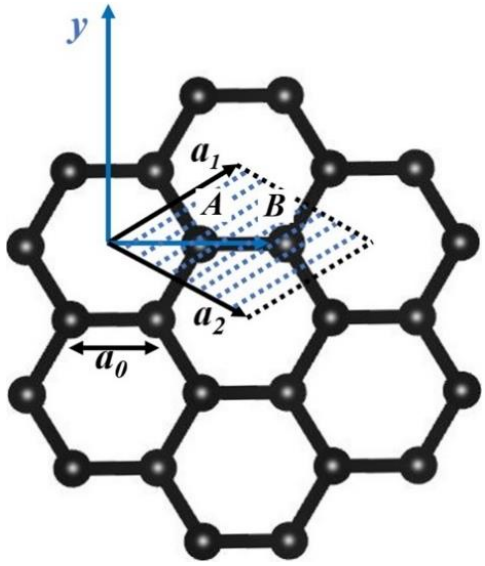

Figure 1.2: Graphene lattice structure with vectors a_1 and a_2 representing the unit cell. Two carbon atoms in the unit cell are represented as A and B. (recreated from [16]).

The primitive unit cell of graphene consists of two atoms labeled as A and B [Figure 1.2]. The lattice vectors of monolayer graphene are defined as the vectors that connect equivalent points in neighboring unit cells [16]. Equation 1.1 gives these 2D lattice vectors, in terms of the sp^2 $C-C$ bond length in graphene a_0 [16]:

Mathematically, graphene lattice vectors can be defined as

$$a_1 = \begin{pmatrix} \frac{\sqrt{3}a}{2} \\ \frac{a}{2} \end{pmatrix}; \qquad a_2 = \begin{pmatrix} \frac{\sqrt{3}a}{2} \\ -\frac{a}{2} \end{pmatrix} \quad \text{where} \quad |a_1| = |a_2| = a = \sqrt{3}a_0. \qquad (1.1)$$

The accepted values for the bond length and lattice constant are $a_0 = 1.42$ Å and $a = 2.46$ Å [16].

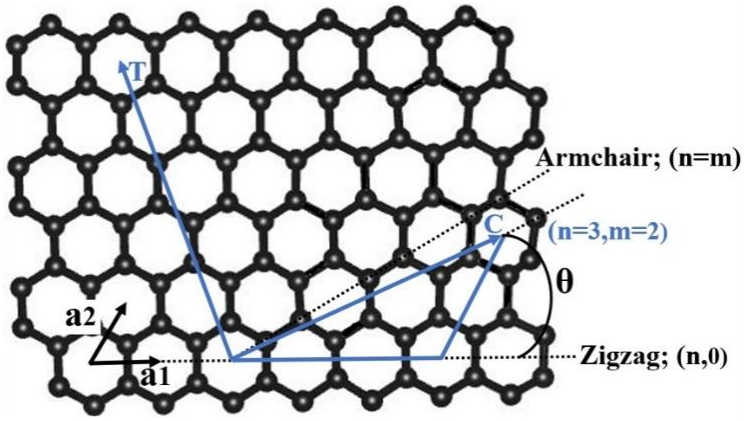

Figure 1.3: The representation of the graphitic lattice vectors a_1 and a_2 in a graphene sheet, denoting various rolling planes that form specific types of SWCNTs. (recreated from [16]).

The reciprocal lattice of a crystalline material can be obtained by taking the Fourier transform of its real space lattice [3]. The real space lattice is characterized by its periodicity, which is determined by the lattice vectors a_1 and a_2 [Figure 1.3]. On the other hand, the reciprocal lattice is characterized by its periodicity, which is determined by the reciprocal lattice vectors $b_1$and b_2 [Equation 1.2], and is expressed in units of wave vector k [16]. The reciprocal lattice plays a crucial role in dictating the manner in which waves and particles with wave-particle duality characteristics propagate through materials [16].

The reciprocal lattice vectors $b_1$and b_2 for the graphene lattice are defined using the relations:

$$a_1 . b_1 = 2\pi, \qquad a_1 . b_2 = 0 \text{ , etc.}$$

Mathematical representation of graphene reciprocal lattice vectors is [16]:

$$b_1 = \begin{pmatrix} \frac{2\pi}{\sqrt{3}a} \\ \frac{2\pi}{a} \end{pmatrix}; \qquad b_2 = \begin{pmatrix} \frac{2\pi}{\sqrt{3}a} \\ -\frac{2\pi}{a} \end{pmatrix}. \qquad (1.2)$$

1.2.2. CNTs

CNTs are cylindrical nanostructures of rolled-up graphene sheets. CNTs exist in two main forms: SWCNTs, composed of a single cylindrical layer, and MWCNTs (as mentioned earlier), consisting of multiple concentric layers. CNTs are renowned for their exceptional mechanical strength, high electrical conductivity, and outstanding thermal properties [19,20].

1.2.2.1. SWCNTs

A SWCNT is defined by a chiral vector (C_h) that encircles the nanotube once and is perpendicular to its axis. It is an important vector to determine key properties and structure of a SWCNT [16].

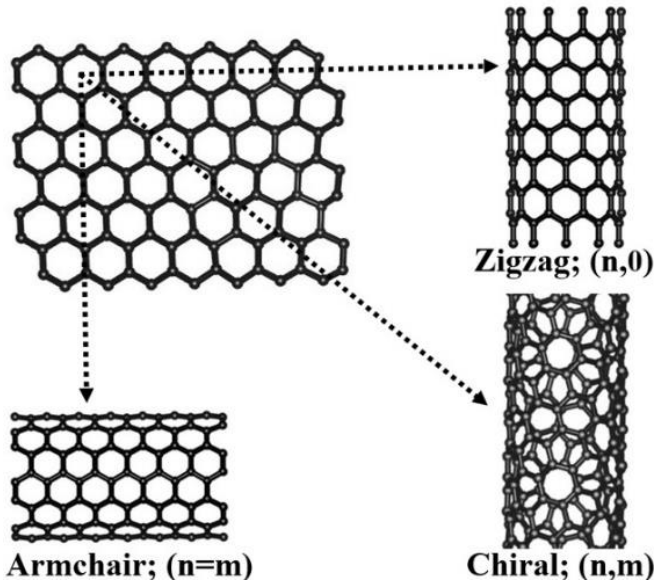

Figure 1.4: Various possible (*n, m*) values result in different forms of SWCNTs.

For the graphene lattice forming the tube to be continuous, the C_h must consist of integers (n, m) multiples of the graphene lattice vector a_1 and a_2, as given in Equation (1.1). The diameter d_t of SWCNT can also be attained from the chiral vector C_h [16].

Relation between the C_h and the d_t of a SWCNT is given by [16]:

$$C_h = na_1 + ma_2$$

$$d_t = \frac{|C_h|}{\pi} = \frac{a}{\pi}\sqrt{n^2 + m^2 + nm}$$

$$cos\,\theta = \frac{C_h.a_1}{|C_h||a_1|} = \frac{2n+m2}{2\sqrt{n^2+m^2+nm}} \quad ;$$

where n and m are constants.

θ is the angle between a_1 and C_h.

Different SWCNTs can be classified based on various n and m values as [Figure 1.4]:

a) Armchair: (n, n).

b) Zigzag: $(n, 0)$.

c) Chiral: (n, m) where $(0 < m < n)$.

Another lattice vector of a SWCNT is the translation vector, T [Figure 1.5], which is the shortest vector in the axial direction and runs perpendicular to C_h (i.e., parallel to the SWCNT axis). T begins and ends on a lattice point, which is an integer multiple of the graphene lattice vectors [Equation 1.3] [16]. These integers (n, m) completely describe the structure of the SWCNT [16].

Mathematically, T can be written as:

$$T = t_1 a_1 + t_2 a_2 \qquad (1.3) \quad \text{where}$$

$$t_1 = \frac{2m + n}{p}, t_2 = -\frac{2n + m}{p} and$$

p is the greatest common divisor of $(2m + n)$ and $(2n + m)$.

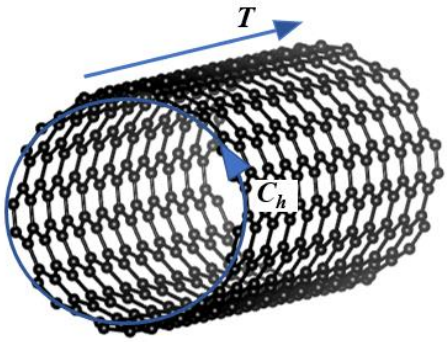

Figure 1.5: A (9,9) armchair SWCNT structure with representation of the chiral vector (C_h) and translation vector (T) [16].

1.2.2.2. MWCNTs

MWCNTs are elongated, hollow cylindrical nanostructures of many rolled graphene sheets. Their diameters range in nm, and they can grow to lengths of several cm, resulting in aspect ratios that can vary for a large range. The thickness of MWCNT walls remains relatively uniform along their axis, giving rise to a straight inner channel [21]. Accessing this channel directly from the outside is hindered because pristine MWCNTs have sealed ends in the form of half fullerene spheres. Nevertheless, it is possible to reach this inner channel by employing techniques such as oxidation, milling, or ion beam treatment to open the nanotube [21].

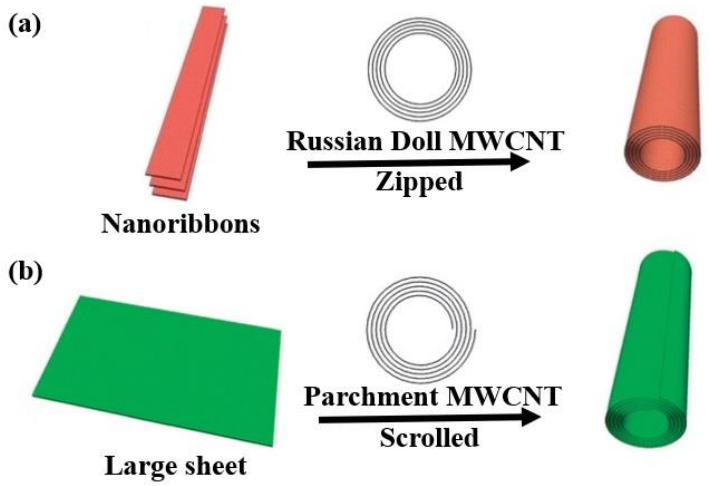

Figure 1.6: (a) Representation of Russian Doll and (b) Scroll / Parchment MWCNTs [22].

MWCNTs can be described by two models: the Russian Doll model [22], where sheets of graphene are arranged in concentric cylinders within larger-walled nanotubes [Figure 1.6(a)] and second is the Parchment or Scroll model [22], which resembles rolling a single sheet of graphite around itself, much like rolling a sheet of paper [Figure 1.6(b)]. In Russian-doll-like structure, each individual SWCNT forms one of the layers of the MWCNT. The separation between these layers, or walls, measures approximately 0.34 nm, which is slightly larger than the spacing between sheets in graphite i.e., 0.335 nm

[23]. A key distinction between MWCNTs and SWCNTs lies in their mechanical properties: MWCNTs are characterized as stiff and rod-like structures, whereas SWCNTs exhibit flexibility [23].

1.2.3. CNS

Though, extensive studies on CNTs have delved to understand these structures better, however, certain domains within the realm of carbon nanostructures remain ripe for significant research endeavors. An illustrative instance is the study of various properties of other low dimensional carbon 1D structures beyond CNTs, e.g., CNS that serve as a compelling case in point. This material was first discovered in 2004 [24] and the formation involves the rolling of a GS into a scroll-shaped structure.

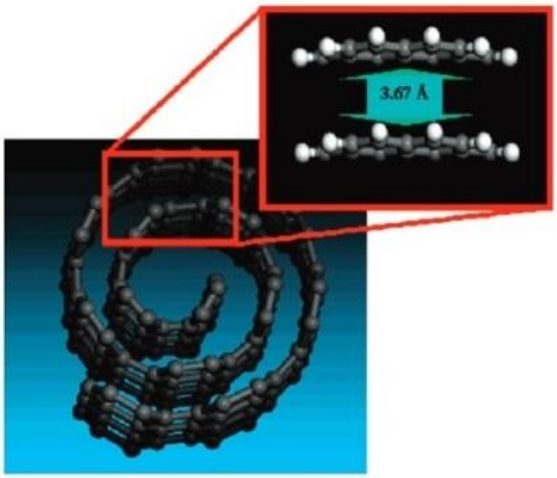

Figure 1.7: CNS-model system with highlighting the two curved graphene layers (image courtesy: Benjamin et. al. [25]).

\

CNS possesses a critical characteristic that its interlayer spacing precisely matches the vdWs diameter of carbon [25,26], measuring 0.34 - 0.367 nm [Figure 1.7], [23], while its inner diameter must exceed 1 nm to maintain stability [23]. Difference between

parchment model of MWCNT and CNS is in the diameter tunability according to the requirement. The inner diameter of a stable MWCNT is usually around 0.4 nm to few nm and the outer diameter can be several nm (10 - 20 nm [27]) depending on the number of walls in the structure. On the other hand, inner diameter of CNS is 1 nm for stable configuration and the outer diameter can vary to several μm [25,28]. For the attachment of large functional groups, CNS is more preferable than MWCNTs.

1.2.4. Junctions

The branch heads or the sidewise-heads of the functionalized CNT bundles are known as T and Y junctions [Figure 1.8] or interconnects. These junctions can be fabricated through multiple means, such as chemical vapor deposition (CVD), fusion of two intersecting nanotubes using a high-temperature electron beam, or by applying irradiation techniques to convert neighbouring tubes into a Y or T shaped structure [29,30].

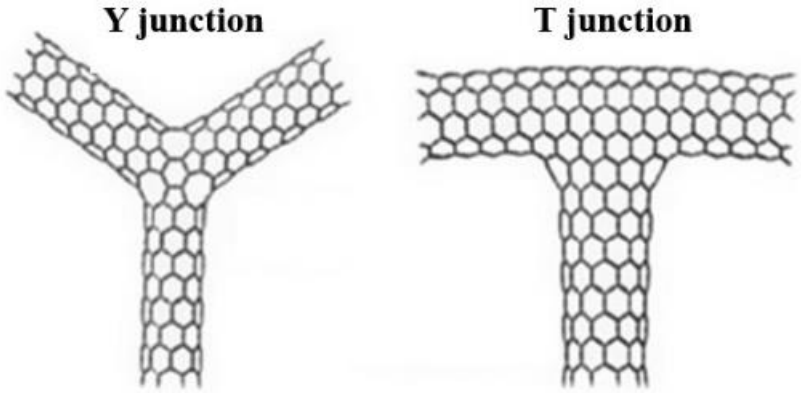

Figure 1.8: Schematic representation of Y and T junctions [25].

They serve as essential building blocks for advanced quantum and nano-electronic devices, enhancing the performance by exploring nanoscale quantum phenomena and extending their utility beyond electronics [29,30]. They contribute to fundamental research by illuminating nanomaterial behavior at junctions and defects, advancing our

understanding of CNTs and inspiring innovative applications in emerging technologies [29,30].

1.2.5. Twisted CNTs

Twisted CNTs represent a compelling avenue of research, as their synthesis, often achieved through nitrogen doping, introduces a unique structural twist to the traditional CNT arrangement. Nitrogen-rich compounds, commonly used as precursors during synthesis or functionalization, induce this twisting effect [Figure 1.9], altering both the electrical and mechanical properties of the nanotubes [31–33]. The introduction of nitrogen atoms creates localized states in the band structure, influencing electrical conductivity, while the twisted structure enhances mechanical flexibility and toughness [31–33]. These tailored electronic properties are particularly useful in transistors and sensors. The ongoing exploration of the twisted CNTs drive advancements in both fundamental understanding and practical utilization [31–33].

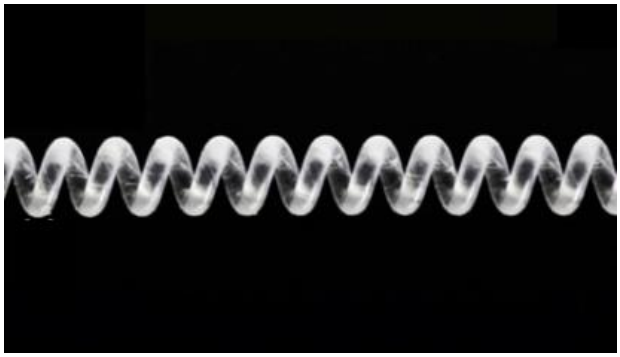

Figure 1.9: A Twisted CNT [33].

1.3. Properties of carbon nanomaterials

1.3.1 Graphene and CNTs

Graphene's covalent bonding mechanism is such that out of a carbon atom's four valence electrons, three participate in forming strong σ-bonds with neighboring atoms, while the fourth valence electron contributes to the creation of weak π-bonds between neighbouring atoms in the graphene layer [16]. The σ-bonds require enormous energy to break contributing to remarkable strength of graphene [16], whereas the electrons in the π-bonds are weakly bound and are highly mobile through the graphene layer [16]. These electrons are accountable for the astonishing electrical properties of graphene [16]. However, both the σ-bonds and the π-bonds are covalent bonds [34].

CNTs being the sp^2 hybridized rolled 1D structures of graphene with high aspect ratio and flexible σ and π-bonds that exhibit unique mechanical, electrical, optical and chemical characteristics have inspired researchers from various fields to undertake thorough investigations. We will discuss below various properties of graphene and CNTs briefly.

1.3.1.1. Chemical properties

Graphene's exceptional chemical stability, characterized by robust *C-C* bonds, imparts resistance to most chemical reactions, acids, and bases. While graphene itself is chemically inert, its edges and defects can render highly reactive sites through functionalization, enabling tailored modifications and facilitating chemical reactions. Tailored graphene is sensitive to gases finding applications in gas sensors, serves as an excellent catalyst support, interacts with biological molecules for applications in biotechnology, and provides corrosion protection, making it a versatile material with diverse industrial and scientific uses [31,35]. Chemical properties of CNTs can vary depending on their specific structure, surface functionalization, and the presence of defects or impurities. The strong covalent *C-C* bonds in the hexagonal lattice of graphene forming CNTs are highly stable and can withstand harsh chemical conditions without breaking or undergoing significant degradation. The delocalized π-electrons in CNTs make it difficult for external chemical species to interact with and disrupt the electronic structure of CNTs. CNTs exhibit remarkable resistance to oxidation due to sp^2 hybridized

carbon atoms that have a strong affinity for electrons, making them less susceptible to oxidation reactions. Additionally, the tightly packed carbon hexagons in CNTs hinder the diffusion of oxygen molecules, further enhancing their resistance to oxidation [36,37]. This property makes them useful for applications such as catalyst supports, sensors, and electrodes [36,38,39]. However, challenges remain in controlling and manipulating the chemical properties of CNTs for practical applications.

1.3.1.2. Thermal properties

Symmetric lattice structure of graphene allows phonons (vibrations of atomic lattice) to move efficiently through it with an impressive thermal conductivity even at ambient temperature. In presence of imperfections, graphene becomes a promising material for thermal management applications in electronics and nanoelectromechanical systems (NEMS). Additionally, 2D nature and light weight single-atom thickness of graphene contribute to its exceptional heat dissipation properties, which are crucial in the development of advanced thermal materials and nanoscale heat spreaders. CNTs possess an exceptionally high thermal conductivity, surpassing all known materials. With a low thermal expansion coefficient, they resist thermal stress and shock, making them desirable for high-temperature applications [37]. The anisotropic thermal conductivity of CNTs enables efficient heat conduction in one direction while blocking it in another, which is valuable for thermal interface materials. Their significant diameter-to-length ratio facilitates absorption and effective storage of thermal energy [28]. CNTs are efficient conductors of heat along their length and can display thermal rectification behavior. With high thermal stability and unique electronic structure, CNTs act as good catalysts for thermal reactions, including energy conversion and storage. They are being researched for high-performance thermoelectric devices, converting waste heat into electricity, enhancing energy efficiency [40].

1.3.1.3. Mechanical properties

Due to strong *C-C* bonds, graphene possesses 100 times more tensile strength than steel, exceptional mechanical properties, ranking them among the strongest materials. Graphene is incredibly stiff and light weight due to its one-atom thick configuration which is ideal for strengthening any composites. It also exhibits impressive flexibility and elasticity, rebounding after deformation, enabling applications like flexible electronics. The Young's modulus of 11 CNTs showed an average value of 1.8 TPa [32] with the lowest value recorded as 0.40 TPa, while the highest value as 4.15 TPa [32], [41]. As a results, the Young's modulus of CNTs is comparable to that of graphite ~ 1 TPa and can potentially be even higher, especially for small SWCNTs [42]. CNTs also exhibit exceptional resistance to deformation when subjected to an external force with a stiffness of ~1 TPa [41,43,44]. With such high stiffness, CNTs have the ability to undergo elastic deformation and return to their original shape once the load is removed. This unique property, known as resilience, makes CNTs valuable in applications where flexibility and durability are of crucial considerations. CNTs can be incorporated into composite materials to enhance their strength, stiffness, and durability. Their exceptional stiffness allows for the development of lightweight yet strong structures and their resilience ensures that the materials can withstand cyclic loading without compromising on performance and ensuring longevity and reliability of the systems. Bending strength of MWCNTs with a larger diameter reveals an average value of 14.2 ± 0.8 GPa [36,41,45–48] which is considerably higher than the standard bending strength of 1 GPa observed in graphite fibers [49]. The remarkable bending strength of CNTs is attributed to their exceptional flexibility with useful applications in NEMS [36,43]. Also, high fracture toughness can resist crack propagation and fracture, indicating substantial enhancements in fracture toughness, ranging from 50% to 200%, when compared to the matrix material [36,43]. These improvements are observed for moderate CNT volume fractions ranging from 1% to 10% [50] for uses where resistance to impact or mechanical damage is important [36,43]. The integration of these mechanical characteristics renders CNTs an excellent material choice for high-performance composite applications, energy storage devices, and sensors.

1.3.1.4. Electrical properties

Pristine graphene possess efficient electron transport via ballistic phenomena in which electrons can travel long distances without scattering. It is due to the absence of impurities and the strong *C-C* bonds in the lattice of graphene [15]. Additionally, graphene is a promising candidate for quantum hall conductivity applications. The electrical conductivity of CNTs can vary depending on their structure, purity, and alignment. Individual CNTs have demonstrated remarkable conductivities, reaching levels as high as $10^8\ S/m$ [50]. This surpasses the conductivity of standard metallic conductors such as copper (Cu), which typically has a conductivity of $5.8 \times\ 10^7\ S/m$ [51]. CNTs can be either metallic or semiconducting depending on their chirality. Semiconducting nanotubes have a bandgap that allows them to act as electronic switches [51], similar to the behavior of conventional semiconductor materials such as silicon. The electrical conductivity of SWCNTs ranges from 10^2 to $10^6\ S/cm$, while MWCNTs typically exhibit conductivities of 10^3 to $10^5\ S/cm$ [52]. Electrical conductance of CNTs can be altered by defects or impurities, doping (intentional introduction of foreign atoms), and the degree of CNT bundling and temperature, with CNTs often exhibiting lower conductivity at higher temperatures due to increased thermal vibrations.

Overall, graphene and CNTs possess excellent electrical properties, and their unique combination of high conductivity, mechanical strength, and low weight makes them promising materials for various electronic and electrical applications such as electrostatic discharge [53], electromagnetic interference prevention [40], transistors, interconnects and sensors etc. [54–57]. However, challenges remain in scaling up the production of graphene and CNTs and integrating them into practical electronic devices.

1.3.1.5. Optical properties

Optical properties of graphene are exceptional owing to 2D hexagonal lattice structure. It is almost completely transparent, absorbing only about 2.3% of visible (Vis) light, remaining highly transparent in the Vis spectrum. However, it is a strong absorber of light

in the ultraviolet (UV) and near-infrared (NIR) regions. This tunable absorption across a wide range of wavelengths makes graphene valuable for applications like photodetectors and modulators.

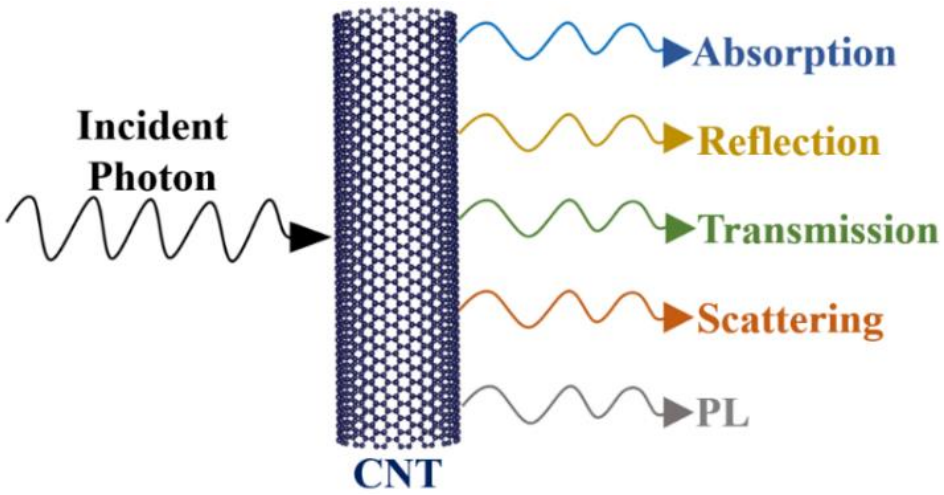

Figure 1.10: Different ways of interaction of photon with CNT.

Moreover, graphene exhibits a pronounced optical $Kerr$ effect, which means it can alter the refractive index of a material in response to intense light, enabling applications in nonlinear optics for signal processing and ultrafast laser technologies. When a photon interacts with a CNT, several processes can occur e.g., absorption, reflection, transmission, scattering, radiative and non-radiative processes [Figure 1.10] etc., however, it's essential to acknowledge that the particular interaction of photons with CNTs may differ based on their structure, diameter, chirality, and the energy of the incident photons. Experimental techniques and theoretical models are used to study and characterize these interactions in detail.

Absorption

If the energy of the incoming photon aligns with the energy gap between electronic energy levels within the CNT, absorption can occur, causing an electron transition from a lower energy state to a higher one. The dispersion relation [Figure 1.11] plays a crucial

role in understanding the absorption properties of CNTs by determining the allowed transitions between the valence and conduction bands [58] which is influenced by the chirality indices (*n, m*) and the related electronic properties [58].

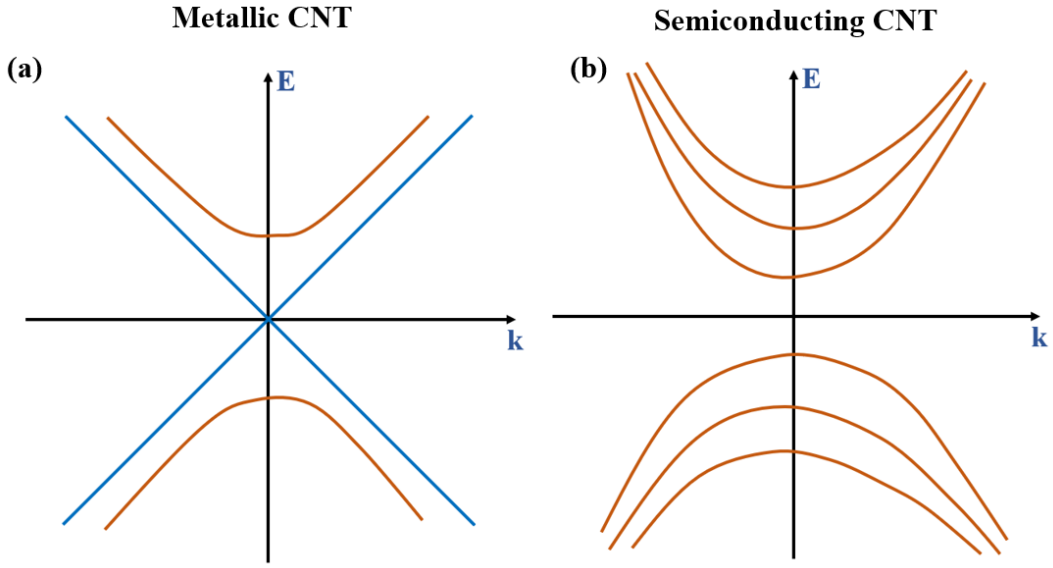

Figure 1.11: Dispersion relation for the 1D electronic energy band structure of (a) a metallic CNT, and (b) a semiconducting CNT. At Fermi level, there is a nonzero DOS for metallic CNTs, however, undoped semiconducting CNTs exhibit a band gap, resulting in a vanishing DOS near the Fermi energy (E_F).

Metallic CNTs exhibit a linear dispersion relation near the Fermi level, while semiconducting CNTs have a finite bandgap [Figure 1.11(a, b)]. Absorption spectra in CNTs can be tailored by selecting the appropriate chirality (*n, m*) and bandgap [58], as well as the wavelength of the incident light. Presence of Van Hove singularities (VHS) arising from the quantized energy levels of electrons and holes in the density of states (DOS) of 1D CNTs enhance the absorption of photons at specific energies [58]. CNTs can absorb light across a wide spectral range, from UV-Vis-NIR and different electronic transitions can be possible according to the selection rule [59,60] depending on the chirality indices (*n, m*) of the nanotube. The key selection rule for CNTs is the conservation of the axial momentum component, $\Delta k = k - k'$, where k and k' are the

wave vectors of the initial and final states, respectively [59,60]. The transitions that satisfy this momentum conservation are only allowed.

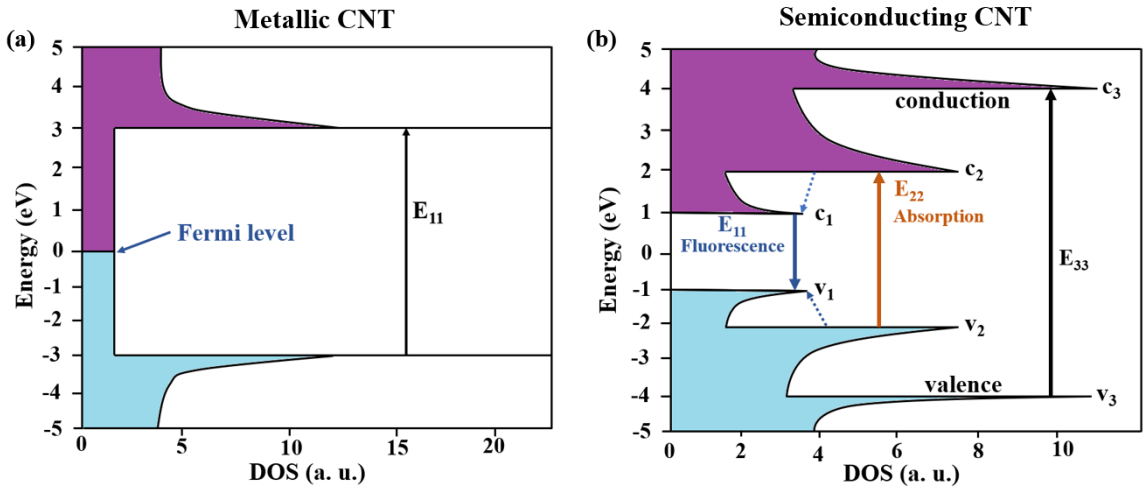

Figure 1.12: Schematic of DOS in (a) a metallic CNT, (b) a semiconducting SWCNT: sharp maxima as VHS and dominant optical absorption/emission indicated by arrows.

Figure 1.12 illustrates the potential electronic transitions from the valence band to the conduction band, along with the corresponding energy level assignments. For example, the transition from the valence band (v_1) to the conduction band (c_1) is represented by E_{11}. Similarly, E_{22} and E_{33} indicate the second and third level electronic transitions, respectively. Also, doping or functionalization of the CNTs affect the absorption properties by altering the electronic structure and energy levels [58]. This has implications for various applications, including photovoltaics, photodetectors, and optical sensors [59–63]. Understanding and controlling the absorption properties of CNTs are crucial for harnessing their potential in various optoelectronic applications.

Reflection

CNTs can exhibit both specular and diffuse reflection depending on incident angle, wavelength of light, and surface characteristics of the nanotubes. In general, CNTs have a low reflectance in the Vis and near NIR regions due to their high absorption coefficient

[64]. The reflection behavior of CNTs can be further influenced by their alignment and orientation. Aligned arrays of vertically aligned CNTs, for example, tend to exhibit low reflectance due to enhanced light trapping and multiple scattering within the nanotube forest structure [65]. Additionally, surface modifications by introducing functional groups or coatings onto the CNT surface can alter the surface roughness and refractive index, leading to changes in the reflection characteristics. The presence of defects, impurities, or structural disorders within the nanotubes introduce scattering, potentially influencing the reflectance behavior of CNTs. For stray light control light applications, it is desirable to make CNT based films with high absorbance i.e., low reflectance.

Transmission

Depending on the wavelength and energy of the incident photons, some photons can pass through the CNTs and emerge on the other side when the photon energy is below the bandgap of the nanotube. CNTs can be transparent to light from Vis to NIR regions. The transparency is particularly prominent for SWCNTs with small diameters [58] owing to their larger energy gap between the electronic energy levels [58]. As the diameter increases, the energy gap decreases, leading to reduced transparency and increased absorption. Longer and aligned CNT arrays can enhance the optical transmission properties [65] by providing a larger path length for light transmission and reducing the chance of absorption or scattering. Aligned arrays can facilitate the transmission of light through the ordered nanotube structure, minimizing the scattering and maximizing the transmission efficiency [65]. The optical transmission of CNTs can be modified by defects, surface coatings or functionalization. Coatings or functional groups can alter the refractive index or surface roughness, influencing the transmission properties [65]. Additionally, presence of defects and functionalization can introduce absorption or scattering centers that can affect the overall transmission behavior.

Scattering

Scattering in CNTs refers to the process by which incident photons or other particles interact with the nanotubes and undergo a change in direction, energy, or momentum. Scattering phenomena in CNTs play a significant role in determining their optical, electrical, and thermal properties. Rayleigh scattering occurs when incident photons interact with CNTs and scatter without a change in wavelength. It is the predominant scattering mechanism in CNTs for photons with energies much lower than the electronic bandgap. Rayleigh scattering is responsible for the weak scattering of Vis and NIR light in CNTs. Raman scattering serves as a potent spectroscopic approach utilized for the examination of vibrational modes and structural properties of CNTs [54]. When photons interact with CNTs, they induce Raman scattering, resulting in the emission of photons with different energies (wavelengths). Phonon scattering involves the interaction of incident particles, such as electrons or photons, with phonons (vibrational modes) in CNTs [54]. Phonon scattering determines the thermal conductivity of CNTs. Various scattering mechanisms, such as $Umklapp$ scattering and boundary scattering, can contribute to the reduction of thermal conductivity in CNTs [54]. The presence of impurities, defects, or structural disorders in CNTs can introduce scattering centers, leading to the scattering of incident particles. Impurity and defect scattering can affect the electrical conductivity, carrier mobility, and optical properties of CNTs. Electron-phonon scattering involves the scattering of electrons by phonons in CNTs [55] which plays a crucial role in determining the electrical conductivity and carrier mobility in CNTs [55]. Understanding and controlling scattering mechanisms in CNTs provide valuable insights into the fundamental properties and behavior of CNTs, enabling their optimization for specific applications. For instance, in optoelectronic devices, minimizing scattering can enhance the efficiency of light absorption and emission.

Photoluminescence

Photoluminescence (PL) properties of CNTs depend on structural characteristics (diameter, chirality, defects) and the environment and it is the characteristic of the semiconducting CNTs. Excitons (electron-hole pairs) are formed in CNTs due to their

1D structure and vanishing DOS near band edges. Different chiralities emit light at various wavelengths from UV to NIR. The precise determination of optical transition energies, such as E_{11} and E_{22}, for a diverse set of identified SWCNTs [56], has posed challenges to theoretical models of nanotube electronic structure. Defects in the CNTs create additional electronic states within the bandgap and modify the emission. PL quantum yield varies due to defect levels, environmental interactions through temperature, pressure etc., and excitation conditions and finds applications in optoelectronics, sensors, and bioimaging [49,51,57–59,66].

Overall, CNTs possess a very distinctive optical nature that define them highly captivating for numerous applications in the field of optics and photonics. Nonetheless, there are still hurdles to overcome in terms of effectively controlling and optimizing the properties for practical uses.

1.3.2. CNS, Junctions and other twisted structures

The characteristics of CNS closely resemble those of CNTs in most aspects, with the exception being their response to axial compression and torsion. Under these conditions, CNS tend to be more vulnerable to bending. The primary distinction between CNS and CNT lies in their structural topology, with CNS exhibiting an open-end topology, whereas CNTs having closed-end topology [27]. The Young's modulus for armchair CNS converges at approximately 1042 GPa, whereas for zigzag CNS, it converges to around 1036 GPa [25]. The orientation of the hexagonal rings concerning the direction of the applied load can inherently impact the results since deformation is reliant on orientation. CNS contributes in opto-electronic applications immensely in a similar way of CNTs. In the UV-Vis range, CNS display higher absorbance due to their significant curvature in comparison to CNTs and amorphous carbon sheets. Within the spectral range of approximately 300 nm (4.13 eV) to 800 nm (1.55 eV), CNS exhibits nearly twice the absorbance of CNTs and amorphous carbon layers, while maintaining consistent reflectivity [67]. Calculated reflectivity and refractive index curves further reveal a shared spectral profile among CNS, CNTs, and carbon sheets across the UV-Vis-NIR

range, with the majority of incident light absorption occurring between 1240 nm (1 eV) and 310 nm (4 eV) [68]

T / Y junctions are majorly found in the modified or functionalized CNTs due to attachment of oxygen rich functional groups, e.g., hydroxyl, carboxyl, epoxy etc. that increase the dispersion of CNTs and make these junctions. Their unique structure, electronic and optical properties are pivotal in nanotechnology and materials science, offering tunable absorption and emission spectra upon excitation, making them versatile for custom nanophotonic and light-emitting devices. The electrical properties of the junctions are highly tunable according to the extent of functionalization of the CNTs and the polymer grafting of these interconnects provide good adhesion applications [29,68].

1.4. Importance of carbon nanomaterials for space research and applications

Carbon nanomaterials such as CNTs, GS, CNS, twisted CNTs and junctions have generated significant interest, playing a vital role in reducing reflection and enhancing light absorption in adverse space environments for spacecraft applications. Their exceptional light-absorbing properties span across a wide range of wavelengths, including UV to infrared (IR) regions, which is very effective for absorbing incident radiation in space [22,64,65]. With large surface area and unique electronic structures, CNTs and CNS enable efficient light absorption, minimizing reflection and scattering and enhancing the darkness of the coated films. This results in low reflectance values, ensuring minimal reflection of the incident light and thereby improved light absorption, which is crucial for minimizing stray light in spacecraft settings [22,64,65]. These coatings can be applied to various spacecraft substrates, including metals, polymers, and ceramics, using different synthesis and deposition techniques. This kind of flexibility ensures compatibility and adaptability in diverse spacecraft components [22,64,65]. Moreover, carbon nanomaterials like CNTs exhibit excellent thermal stability and their

optical properties remain intact even under the extreme temperature conditions in space [22,64,65] ensuring long-term reliable performance.

These paintings can be used for solar energy harvesting, for thermal management and sensing, for aerospace applications and in optical devices, that contribute to improved scientific observations, accurate measurements, and protection of sensitive onboard components by reducing unwanted reflections and enhancing overall performance of various optical systems and instruments [22,64,65]. Fabrication of lightweight and strong composites is possible due to high strength-to-weight ratio that can also sustain in high temperatures [69]. By harnessing the light-absorbing capabilities of low dimensional structural hybrids of carbon, researchers and engineers are constantly working to develop efficient and customizable coatings for a wide range of practical uses.

1.5. Conclusion

In this chapter, we have given a general overview on the structure and properties of different low dimensional structural hybrids of carbon. Research on carbon nanomaterials and stray light control applications have withstand a remarkable progress; however, many challenges need to be addressed before their full potential can be practically realized. These challenges include improving the scalability of production methods, enhancing the purity of the material, and developing efficient ways of integrating them into devices.

CHAPTER 2

Experimental Methods

This chapter discusses the production, purification, functionalization and polymer grafting process of the CNTs. After giving a general introduction, we discuss the HiPCO process, purification, and functionalization followed by fabrication of stable composite thin film coatings comprised of low dimensional structural hybrids of carbon. This was achieved by using an appropriate solvent and binder via grafting polymer onto the functionalized carbon structures that involved inter- and intra- tube intercalation of CNTs by different functional groups and ions.

2.1. Introduction

There are several techniques available for production of SWCNTs, including arc discharge (AD), laser ablation (LA), CVD, and HiPCO dissociation etc. Iijima employed the AD method to produce MWCNTs which involved generating an AC plasma arc between two graphite electrodes at high temperatures of around 3000-4000°C in an inert atmosphere, causing the sublimation of carbon [1]. The sublimated graphite containing CNTs is then deposited on the negative electrode, as well as on the walls of the chamber where the process is carried out [1]. These structures turned out to be MWCNTs, which he described in his groundbreaking 1991 Nature paper [1]. In order to obtain SWCNTs, the electrodes were doped with catalyst particles such as Ni-Co, Co-Y, or Ni-Y [10,70,71]. The resulting CNTs in the product are typically intertwined and have varying lengths [10,70,71]. This research played a pivotal role in popularizing CNTs and establishing their significance across various scientific and technological domains.

Later Guo et al. [72,73] used the LA technique for CNT production in 1995. In this process, a high-power laser was used to vaporize carbon from a graphite target containing 1.2% of Co/Ni with 98.8% of graphite component at 1200°C in a quartz tube furnace under an argon (Ar) atmosphere (~500 Torr) [72,73]. Metal particles are added to the graphite targets as catalysts to generate SWCNTs, similar to the AD technique. The quantity and quality of CNTs produced are controlled by many factors, such as the amount and type of catalysts, laser power and wavelength, temperature, pressure, type of inert gases, and fluid dynamics near the carbon target [72,73]. Ar is used as a carrier gas to transport the vapors from the high-temperature chamber into a cooled collector positioned downstream [72,73]. The nanotubes self-assemble from the carbon vapors and condense on the walls of the flow tube. This method is effective in producing both MWCNTs and SWCNTs, with SWCNTs having a diameter distribution of about 1.0-1.6 nm. The purity of CNTs produced through this method is approximately 90%, which is higher than that produced by the AD method.

While AD and LA methods played important roles in the early discovery and exploration of CNTs, CVD has emerged as a preferred method for large-scale production, control

over CNT properties, high purity, and compatibility with various applications and deposition techniques. This makes CVD highly significant for industrial applications and diverse scientific and technological fields. CVD process involves the removal of all moisture-containing gases from the furnace chamber to prevent oxidation reactions, followed by purging of hydrocarbon precursor gases along with an inert gas such as helium (He) or Ar [74,75]. The furnace is then heated to a temperature range of approximately 600-1200°C to vaporize and decompose the gases, resulting in the reaction between the reactive species from the gases and the catalyst, which produces the deposition of nanotubes on the substrate [74,75].

Additionally, HiPCO process is mainly used for the production of SWCNTs, which is a specialized form of CVD holding significant advantages over conventional CVD techniques. This method also allows for precise control over the length and diameter of the CNTs, enabling tailored properties for specific uses with large-scale CNT production. It is compatible with different carbon feedstocks, offering versatility in precursor materials and expanding the possibilities for synthesizing CNTs with desired characteristics. Since, our work relies on the HiPCO SWCNTs, it requires a more comprehensive discussion.

2.2. HiPCO technique of SWCNT production

The HiPCO technique is a gas-phase method for synthesizing SWCNTs with high-yield that was developed at Rice University in the early 1990s [76,77]. Under high-pressure (30-50 atm) and high-temperature (900-1100℃), SWCNTs are grown in the presence of iron nanoparticles (FeNPs) and a flow of carbon monoxide (CO) gas. The FeNPs react with the CO gas to form iron pentacarbonyl [$Fe(CO)_5$] in the reaction zone of the chamber [77]. Upon heating, [$Fe(CO)_5$] decomposes, which condense into large catalytic Fe clusters that act as nucleation sites for the growth of SWCNTs [76,78] [Figure 2.1]. The growth process is governed by gas-phase CO disproportionation,

involving the redox reaction of a chemical equilibrium mixture of CO and carbon dioxide (CO_2) at a given temperature.

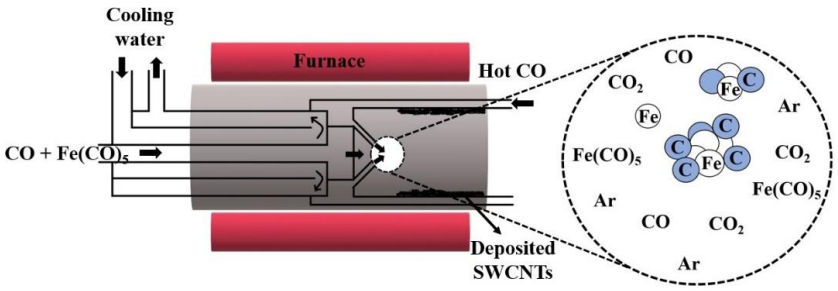

Figure 2.1: HiPCO process diagram depicting inside chamber reaction.

This is known as the Boudouard reaction [Equation 2.1] [77]. This disproportionation of CO leads to the formation of CO_2 and SWCNTs.

$$CO(g) + CO(g) \rightarrow CO_2(g) + C_{SWCNT}(s) \qquad (2.1)$$

2.2.1. Merits of HiPCO

The production of SWCNTs using HiPCO is currently a popular method due to its high yield offering several merits that contribute to its popularity and effectiveness. The resulting product in this process is a mixture of metallic and semi-metallic SWCNTs. There are several advantages of the HiPCO process that doesn't rely on pre-made catalyst particles, unlike other CVD techniques [76,78]. The main advantages of HiPCO process are briefly discussed below.

2.2.1.1. Purity

The carbon source used in this process is a high-purity CO gas source, which ensures minimal impurities in the resulting nanotubes [79]. This is crucial for many applications where impurities can adversely affect the desired properties and performance of SWCNTs.

2.2.1.2. Yield

The HiPCO method can generate a large quantity of nanotubes within a short span of time [80]. The high yield is desirable for industrial-scale production and commercial applications that require a substantial supply of SWCNTs.

2.2.1.3. Length and diameter control

One can easily control the length and diameter distribution of SWCNTs in this process by adjusting the reaction parameters, such as temperature, pressure, and catalyst composition. It is possible to manipulate the growth kinetics and control the resulting nanotube dimensions [81]. This control is valuable for tailoring the properties of SWCNTs to meet specific application requirements.

2.2.1.4. Catalyst versatility

The HiPCO method utilizes a variety of catalysts to facilitate the growth of SWCNTs. Transition metal catalysts like Fe, Co and Ni can be employed to achieve different types of SWCNTs (metallic or semiconducting) with specific electronic properties depending on the desired application requirements [82].

2.2.1.5. Scalability

The HiPCO method is scalable, meaning it can be readily adapted for large-scale production. The process can be conducted in a continuous-flow reactor system, enabling the synthesis of SWCNTs in significant quantities [76] which is crucial for meeting the demand of SWCNTs in industrial applications.

2.2.1.6. Compatibility with functionalization

SWCNTs produced by HiPCO are compatible with post-synthesis functionalization. The resulting nanotubes have open ends and defects, making them more reactive and flexible to chemical modifications [82]. Functionalization allows for the introduction of various functional groups, enabling tailored properties and facilitating integration into specific applications.

2.2.1.7. Aspect ratio

A high aspect ratio (length-to-diameter ratio) [83] of HiPCO SWCNTs is very useful for reinforcing composite materials, providing enhanced mechanical strength and stiffness to the composite structure [82].

These advantages make the HiPCO method a valuable technique for generating SWCNTs with diameter ranging from 0.7-1.2 nm for applications in electronics, energy storage, sensing, and nanocomposites [78,84]. Nonetheless, the practical use of the as-synthesized SWCNTs in devices is often challenging due to the presence of amorphous carbon impurities and metal catalyst particles, which necessitate a post-synthesis purification process. Additionally, when subjected to heat treatment, SWCNTs with similar chiral angles experience a gradual increase in diameter as a result of merging into a larger tube [85,86].

2.3. Purification

2.3.1. Importance of purification

Typically, raw SWCNTs obtained from various synthesis methods tend to form aggregates and are held together by vdWs forces [87], resulting in bundled tubes with varying diameters and chiralities, each exhibiting diverse properties [88]. As a result, these bundles or agglomerates have poor dispersibility in solvents and matrices [89]. Also, attachment of residual catalyst particles to the nanotubes, as well as production of amorphous carbonaceous materials during the synthesis process potentially impact the properties and performance of the HiPCO SWCNTs [90]. Purification techniques involving acid treatment and thermal oxidation effectively remove these catalyst residues and eliminate amorphous carbon, leading to a clean and pure CNT product [91,92].

Sonication or surfactant treatment during purification can help disperse and separate the CNTs, and thus improving their integration into applications [93]. Purification via selective functionalization or centrifugation can be employed to separate and isolate specific nanotube entities [89], as well as to transform CNTs into other low dimensional

carbon structures [94]. After purification, these CNTs have improved purity, better-defined properties, and enhanced compatibility for the target applications [84,94].

2.3.2. Different approaches of purification

The purification process involves a series of thermal and acid wash steps. During the thermal treatment, carbon shells are oxidized to produce CO_2 and the metallic particles form oxides [95]. The oxides are then removed by acid wash that transforms them into corresponding salts. Salts are drained by multiple deionized (DI) water wash.

There are three primary techniques for the purification of SWCNTs: (a) physical separation, (b) liquid-phase oxidation, and (c) gas-phase oxidation. Physical separation involves the use of various dispersion techniques to suspend SWCNTs in a surfactant-based solution and then separate them through filtration, centrifugation, or chromatography [95]. However, this method is not suitable for the purification of large SWCNT aggregates [95]. Liquid-phase oxidation involves the treatment of raw soot samples with strong oxidative agents such as $HCL, H_2O_2/HCl, HNO_3$, HNO_3/H_2SO_4, and $KMnO_4$, $HNO_3/H_2SO_4/H_2O_2$ [80,96]. The selection of oxidative agents depends on the metal impurities present in the as-prepared sample. However, acid treatments can cause partial destruction of SWCNT structures, with oxygen-containing functionalities attaching to the defective sites on the outer walls [80,96]. Gas-phase oxidation is another method that is used to remove amorphous carbon impurities at high temperatures in the presence of different gaseous oxidizing agents, such as air, CO_2, H_2O vapor, ozone, H_2S, and $Cl_2/\ H_2$ [95]. This method is more controllable than liquid-phase oxidation and is more effective at removing amorphous carbon impurities. Surface oxides are formed by accommodating oxygen atoms at the free edges of the sp^2 hybridized graphene sheets, stabilizing the dangling bonds in SWCNTs [97]. Liu et al. [98] have reported a multi-step purification process for SWCNTs produced by catalytic CVD method. The process involves three key steps, beginning with the reflux of HNO_3 to remove MWCNT impurities. This is followed by ultrasonication with a $(NH_4)_2S_2O_2/\ H_2SO_4$ solution to

obtain length-controlled SWCNTs, and finally a high-temperature NH_3 treatment to successfully restore the SWCNT structure [98].

2.3.2.1. Purification process for HiPCO SWCNTs

The oxidative chemical purification method is commonly used for the HiPCO SWCNTs, resulting highly pure SWCNT networks with only around 0.3% Fe impurities compared to the as-prepared sample which usually contains more than 20% of Fe impurities [78]. However, this purification process may significantly alter the CNT structure by unraveling or chopping of the tubes into smaller segments [81,99–101]. To remove carbonaceous contaminants, various oxidative processes like gas phase reactions or thermal annealing in air or oxygen are used, while acid treatments are used to eliminate catalyst particles [102,103]. A general flow chart of the purification process is shown in Figure 2.2.

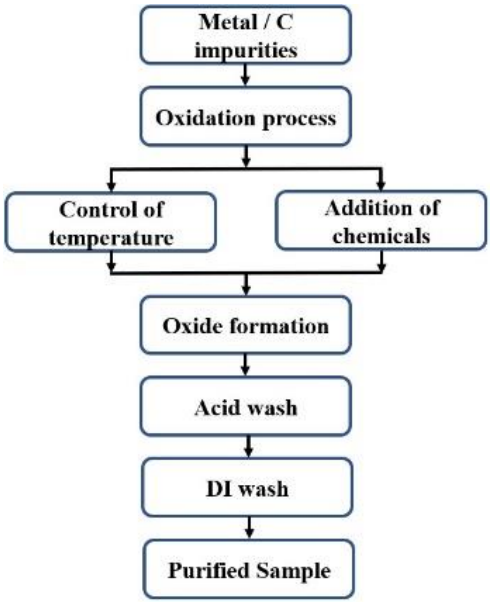

Figure 2.2: Pictorial representation a purification process involving basic steps.

Mackeyev et al. [104] have presented a novel method for purifying HiPCO SWCNTs contaminated with Fe catalyst impurities, which involves the use of liquid bromine as an oxidizing agent. This method has shown a ten-fold increase in nanotube purity without causing significant damage to the SWCNTs shown by NIR-PL and absorbance measurements [104]. The bromine ions interact with the SWCNTs, oxidize the metallic Fe impurities to their corresponding bromide salts which are then washed away with diluted HCl [104]. The resulting iron content in the purified sample remains between 2.8-3.6% by weight [104], but an additional purification step involving HCl/HNO_3 wash further reduces it to 1.6-1.8% [104].

Hu et al. [105] reported a comprehensive assessment of the purification process for electric arc-generated SWCNTs, utilizing HNO_3 treatment. HNO_3 being a potent oxidizing agent, efficiently dissolved the metal catalyst of the SWCNTs [105], attacked amorphous carbon, intercalated SWCNTs, and disrupted large SWCNT bundles, at the cost of significant structural destruction [105]. Purification process for as-grown soot of SWCNTs produced by AC method was performed using microwave, followed by acid treatments [106]. The most favorable outcomes were attained for the air-oxidized (350°C for 1 hour) and 3M HNO_3 acid-treated sample (100°C for 1 hour) [106]. There are also reports on heat treatment of SWCNTs [85,86] to manipulate their structure by reducing strain energy [107].

2.4. Functionalization

CNTs do not readily interact with other atoms or molecules in their bare state due to π-electron cloud which is undistorted. However, when the π-electron cloud is distorted due to formation of defects or dislocations via chemical reactions, functional groups can be attached to the outer walls or ends of the CNTs, making them suitable for specific applications. This process is known as functionalization. However, the insolubility of as-prepared CNTs in water or organic solvents has posed challenges to functionalization [108].

As a result, functionalization of CNTs is of significant importance due to its ability to modify the surface properties and to enhance the interaction of CNTs with other materials or environments which are otherwise inherently insoluble in most solvents. Functionalization allows introduction of various functional groups or molecules on the CNT surface, improve their solubility, promote dispersion in different matrices, such as polymers, metals, or composites and facilitate processing and integration of CNTs for various applications [109]. By introducing compatible functional groups by covalent or non-covalent interactions, functionalization helps in enhancing the interfacial adhesion between CNTs and the surrounding matrix or other materials leading to stronger bonding and improved load transfer between CNTs and the matrix [110]. This is particularly important for applications that require high mechanical strength or electrical conductivity. Also, the electronic, optical, and chemical properties of CNTs can be tuned by attaching different functional groups, for example, altering the bandgap of semiconducting CNTs [36]. Functionalization also enables integration of CNTs into biological systems allowing interactions with biological molecules, cells, or tissues [111]. This opens up possibilities for biomedical applications like drug delivery, bioimaging, biosensing, and tissue engineering etc. [111]. Functionalized CNTs have also shown promise in areas such as water purification, gas sensing, and catalysis [36] by selectively adsorbing or reacting with specific pollutants, facilitating their removal from water or air [112]. Also, stability and oxidation resistance of CNTs can be improved by introducing protective functional groups or coatings to make them more resistant to environmental factors, such as oxidation, moisture, or temperature, thereby extending their lifespan and improving their durability [28].

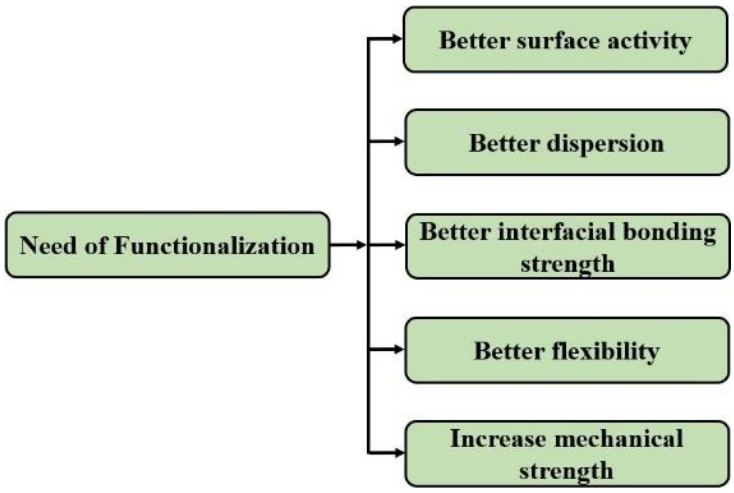

Figure 2.3: Flowchart depicting several significant aspects of the functionalization process.

Hence, functionalization plays a crucial role in tailoring the properties of CNTs, improving processability, compatibility with other materials as shown in Figure 2.3, and enabling a wide range of applications across various fields as discussed above [108].

2.4.1. Different functionalization processes

Functionalization can be achieved through various processes, namely covalent bonding, non-covalent interactions, endohedral filling, and functionalization through intercalation [Figure 2.4] [113].

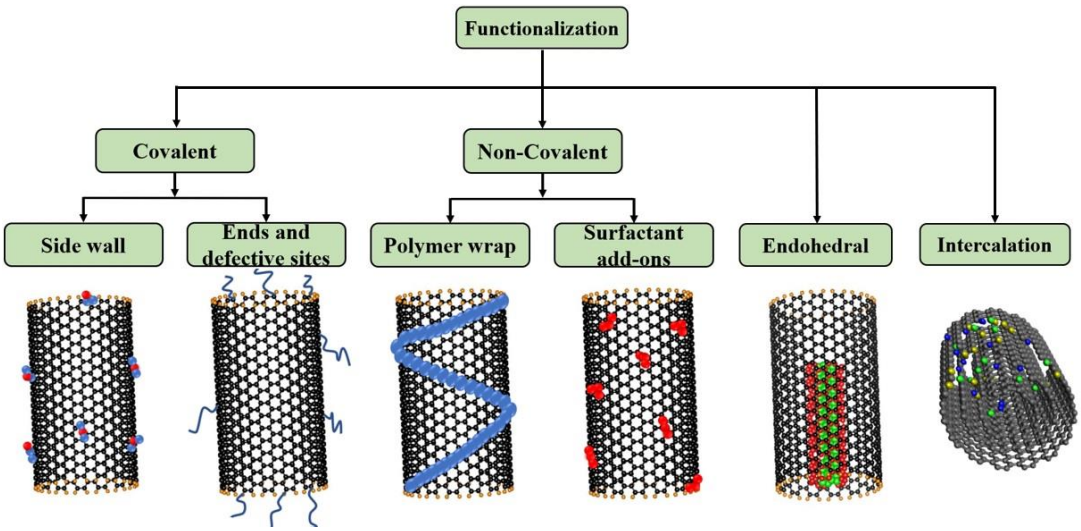

Figure 2.4: Pictorial representation of different methods of functionalization.

2.4.1.1. Covalent

Covalent functionalization involves attachment of chemical entities to the tubular structure of CNTs via covalent bonds, where at least one pair of electrons is shared between the CNT and the introduced chemical entity [113]. It mainly occurs at defects on the side walls and open ends of the CNTs which destroys the sp^2 network and converts it to sp^3 hybridization [113]. This process improves the dispersibility of the CNTs and increases their reactivity, allowing for fine tuning of the physicochemical properties for specific applications. Thus, covalent functionalization provides a pathway to assemble advanced functional materials, including nanotube-based composites or hybrids [113]. However, precise control during covalent functionalization is required to maintain integrity of the CNTs, as excessive destruction will transform the CNTs into amorphous carbon materials. In terms of opto-electronic properties, covalent functionalization via organic reactants is preferred. Carboxylic ($COOH$) groups are mainly attached to the ends of CNTs to avoid steric hindrance, while other functionalities such as carbonyl ($C = O$), hydroxyl (COH), and ether ($-R - O - R'$) make bonds at defective sites on the surface.

Covalent modification provides a more robust anchoring of functional entities, making CNTs suitable for specific applications [113].

The sensitivity and stability of modified CNTs are determined by the charge transfer properties of the attached functional groups [114]. The degree of covalent bonding of these functional groups results in a slight transfer of charge from the CNT to the carboxyl groups [114]. The magnitude of this charge transfer is directly proportional to the electronegativity of the atom attached to the defective site, which attracts the electron cloud towards itself upon formation of the chemical bond. Therefore, functional groups containing oxygen atoms exhibit greater ability to withdraw electron density towards the functional group attachment [114]. In the case of small diameter CNTs, the density of the rehybridized σ-π electron cloud on the surface is very high, making the binding energy for functional groups to find defects and attach themselves to CNTs also very high. Hence, the binding energy of the functional groups follows an inverse relationship with the diameter of the tube [114].

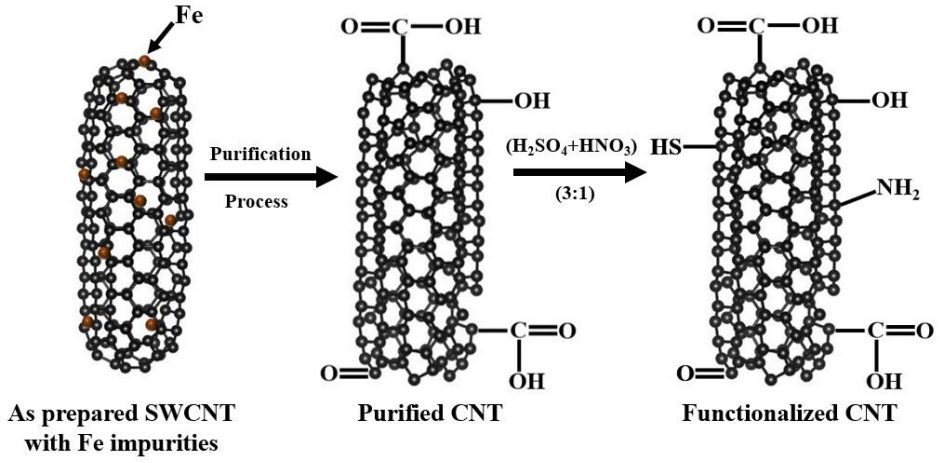

Figure 2.5: Fullerene cap removal and defect generation for an ideal SWCNT during functionalization process.

Figure 2.5 depicts the removal of the fullerene cap from SWCNTs and attachment of $COOH, C=O, COH, (-R-O-R')$, amino $(-NH_2)$ and bisulphide ion $(-HS)$ groups

at both ends and at the defective sites of the tube during the acid treatment. The abundance of these groups is dependent on the temperature and duration of the oxidation process [114]. A DFT investigation has been conducted on HiPCO zigzag SWCNTs with a diameter range of 0.7-1.6 nm to analyze the effects of single and pair functionalization of $COOH$ groups [114]. The most favorable binding configuration occurs when a carbon atom of the carboxyl group forms a direct bond with one of the carbon atoms in the CNT, forming $C - COOH$ bond which is perpendicular to the tube axis [114].

2.4.1.2. Non-covalent

Non-covalent functionalization relies more on strong vdWs interactions, where there is no direct exchange of electrons between the two molecular species, which typically involve long hydrocarbon chains.

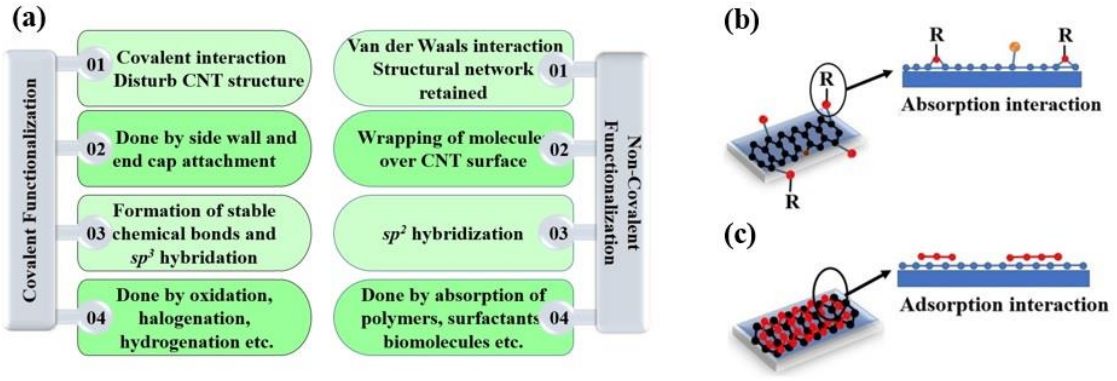

Figure 2.6: (a) Covalent and non-covalent functionalization processes description. (b) Absorption via covalent and (c) Adsorption via non-covalent bonding mechanism.

Figure 2.6(a) represents a comparative study between covalent and non-covalent features, while Figure 2.6 (b) and (c) show absorption via covalent and adsorption via non-covalent interactions respectively. The hydrocarbon chains exhibit strong adsorption properties by experiencing a strong vdWs attraction [Figure 2.6(c)] and are adsorbed onto the surface of CNTs through vdWs, π-stacking, electrostatic, or hydrophobic forces. For applications

requiring strong surface interactions, the covalent approach is more effective than the non-covalent method.

Endohedral filling

In another type of functionalization, the oxidant is filled inside the open-ended CNTs, which is known as endohedral filling process [Figure 2.4]. Such type of functionalized CNTs are mainly used as drug delivery vehicles for bio-medical applications [115].

Intercalation by ions

Figure 2.7 illustrates the intercalation process. This involves insertion of atoms or molecules, referred as intercalants from a different chemical species between the layers of the host material [116]. For intercalation compounds to form, the intra-planar binding forces must be stronger than the inter-planar binding forces [116].

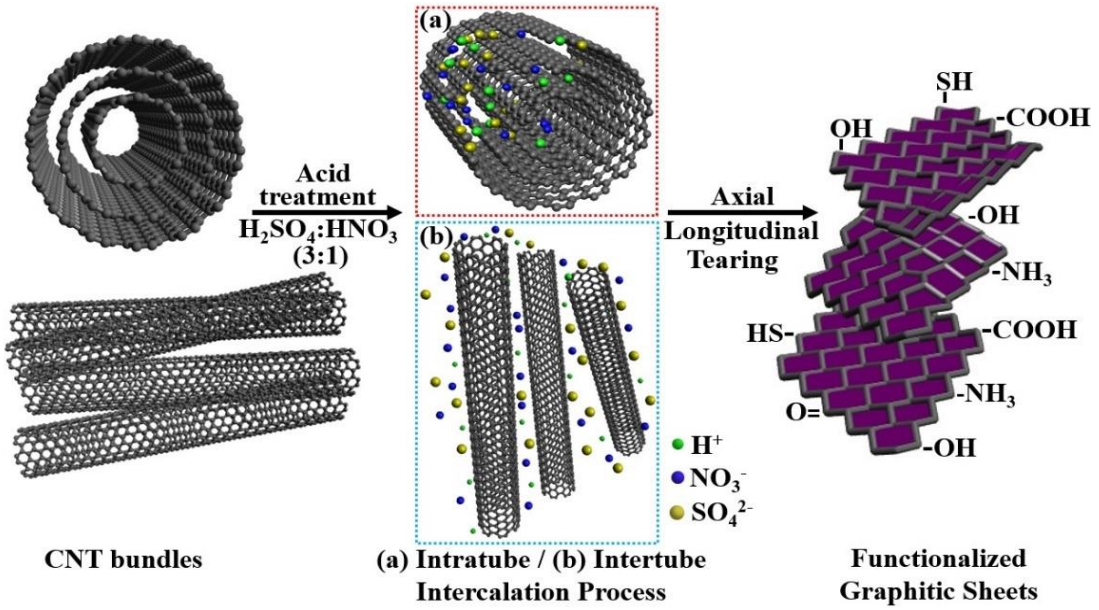

Figure 2.7: CNT bundle acid treatment (a) Intratube MWCNT depletion by ions (b) Intertube intercalation process into bundles leading to graphitic sheets oxidation by axial and longitudinal tearing.

Intercalation process is mostly associated with tearing and unzipping of the CNTs. During the intercalation process in the acidic media (H_2SO_4 and HNO_3), the purified sample undergoes effective inter- and intra- tube intercalation by hydrogen (H^+), nitrate (NO_3^-), and sulfate (SO_4^{2-}) ions, leading to axial and longitudinal unzipping of the CNTs, as shown in Figure 2.7. According to Dresselhaus et al. [116], NO_3^- can also act as an effective intercalant [116–120]. Intercalation due to H^+, NO_3^-, and SO_4^{2-} ions effectively decrease the vdWs interactions among CNT bundles, leading to the segregation of CNTs and the formation of functionalized graphene nano ribbon (GNR) or GS in the sample. Li et al. [117] reported intercalation assisted longitudinal unzipping of MWCNTs due to K^+, NO_3^-, and SO_4^{2-} ions when a combination of KNO_3 and H_2SO_4 was used. Enhanced formation of GNR or GS was observed by accelerating longitudinal unzipping of CNTs via suitable molecular intercalation. Additionally, oxygen, nitrogen and sulphur-containing functionalities can be attached to the open graphitic sheets by performing a strong acid treatment using H_2SO_4 and HNO_3 with ratio (3:1).

Unzipping mechanism is mainly assisted by the formation of ester groups ($= O - C - OR$), which leads to the distortion of β, γ-alkenes through ion attack [121,122]. This results in instability within the system, which can be mitigated by terminating the unstable ends with oxygen-containing functional groups [121,122]. The involvement of ions is critical to this process. HNO_3 is unique that can undergo self-ionization and exhibit both acidic and basic properties [121,122]. As a result, it can act as a base w.r.t. the stronger H_2SO_4. On one hand, the nitronium ion (NO^{2+}) can serve as an active reagent and initiate nitration reactions by attacking the strained aromatic sites.

$$2HNO_3 \rightleftharpoons NO^{2+} + NO_3^- + H_2O \qquad (2.1)$$

$$HNO_3 + 2H_2SO_4 \rightleftharpoons NO^{2+} + H_3O^+ + 2HSO_4^- \qquad (2.2)$$

Equation 2.1 and 2.2 are commonly referred to as the self-ionization equations. Through the intercalation of SO_4^{2-}, NO_3^- and H^+ ions, the strong vdWs attractions between the walls of CNTs begin to weaken gradually [Figure 2.7]. The process of nanotube

unzipping can be initiated by oxidants attaching to one of the internal $C-C$ bonds of the CNTs, stretching and ultimately breaking it down into a nanoribbon structure [122]. In a study conducted by Shinde et al. [123], it was found that K^+, and SO_4^{2-} ions played a crucial role in the counter-ion dependent longitudinal unzipping of CNTs, which led to the production of GNRs. The exfoliation of MWCNTs occurs through the use of $SO_4^{2-}$and NO_3^- ions as co-intercalants in conjunction with K^+ ions.

In our study, during the functionalization process with H_2SO_4 and HNO_3 in ratio (3:1), H^+, SO_4^{2-} and NO_3^- ions played a significant role in tearing the partially functionalized CNTs after purification [Figure 2.7]. This will be discussed in the following chapter.

2.5. Fabrication of thin films

Fabrication of the thin film usually represents the final step in the activity and involves a combination of two primary methods: (a) preparation of the solution to make the coatings via polymer grafting technique, and (b) making the thin films by applying polymer grafted solution using a hand spray brush.

2.5.1. Grafting of polymer as binder

Following the covalent functionalization, the next step involves wrapping or grafting a suitable polymer onto the functionalized heterogeneous carbon structures, which is known as the polymer grafting process. This also provides strong adhesion properties with the suitable substrate. However, the chemistry between the solvent and binder is critical, as poor chemistry can result in the binder settling on the surface of the substrate separately, creating a glue-like appearance and uneven coating. This will result in patches throughout the substrate with significant spatial variation of the film. This issue is easily identifiable through visual inspection. Even if the film appears dark, optical characterization, such as reflectance will have spatial dependence and will not provide a correct value. Therefore, spectral property of the coated sample is highly dependent on

adequate bonding between the solvent and the polymer binder. This requires many trials to optimize the parameters to make a well dispersed coating solution.

To achieve a well-dispersed coating solution, functionalized sample is added to the solvent containing binder. This is followed by sonication with sound waves which will dissociate any structural agglomeration in the medium and will create a well-dispersed solution.

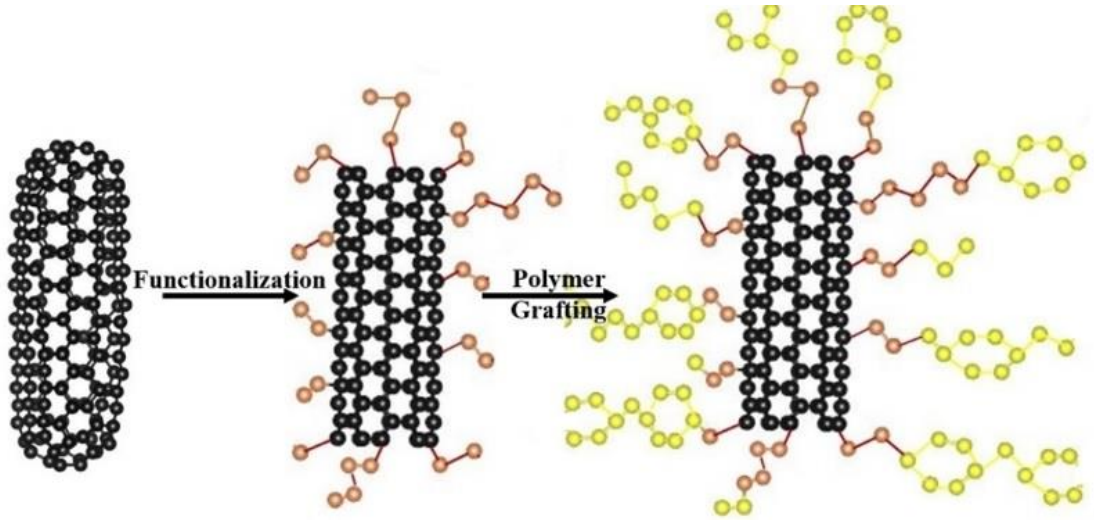

Figure 2.8: Molecular pictorial diagram of functionalization and polymer grafting processes of fullerene capped ideal SWCNT.

Figure 2.8 depicts molecular diagrams illustrating the attachment of functional groups to the purified CNT followed by attachment of binder chains to the structure.

2.6. Conclusion

In this chapter, we have outlined synthesis process, and various purification and functionalization methods in general including intercalation details. We have also highlighted the coating process and the necessity of having a suitable binder to achieve a well dispersed coating solution.

CHAPTER 3

BRIEF INTRODUCTION TO THE DIFFERENT CHARACTERIZATION TECHNIQUES

This chapter provides fundamental working principle and operation of various characterization tools used in this investigation. These tools are indispensable for comprehending the diverse facets of carbon nonmaterial based composite thin film coatings.

3.1. Introduction

Distinct characterization techniques are essential for proper assessment of the desired outcomes. The key procedural elements adhered in this study are:

3.1.1. Chemical study

3.1.2. Morphology investigations

3.1.3. Spectral analysis/reflectance measurements

3.1.4. Space environmental simulation tests

3.1.1. Chemical environment study

In a broader context, Fourier-transform infrared spectroscopy (FTIR), X-ray photoelectron spectroscopy (XPS), Raman spectroscopy and X-ray diffraction (XRD) serve as indispensable analytical tools in the realms of chemistry and materials science. FTIR allows for the precise identification of chemical functional groups and structural features of the purified and functionalized samples, making it invaluable for diverse applications. XPS focusses on surface chemistry, unveils elemental compositions and chemical states of modified samples. Raman spectroscopy excels in identifying characteristic G-band, defect induced D-band and distinguishing $2D$ band for as-prepared, purified, functionalized and coated samples through their unique vibrational spectra and provides non-destructive, versatile analysis. XRD is a powerful technique used to study the chemical environment and crystallography of the materials, particularly the crystalline solids. XRD allows us to determine the atomic arrangement providing critical insights into the chemical composition and structural properties of as-prepared, purified, functionalized and coated samples. Together, these spectroscopic techniques provide invaluable information that are essential for comprehending the intricate chemical properties of the samples.

3.1.2. Morphology study

Following the successful investigation of the chemical nature of the samples, it becomes imperative to gain insights into the morphology of the materials at various stages of purification, functionalization, and coating. We have carried out high resolution transmission electron microscopy (HRTEM), scanning electron microscopy (SEM), and atomic force microscopy (AFM) measurements to furnish us with comprehensive insights and aiding in distinguishing the effects of each treatment. For instance, HRTEM clearly reveals embedded FeNPs in the as-prepared sample, the effective removal of impurities in purified sample, the attachment of functional groups to the sidewalls of CNT-modified structures, and distinct structural evolution of SWCNTs in the processes. The SEM and AFM studies further contribute in providing information about the surface morphology of the random network of the composite films comprised of polymer grafted carbon nanostructures, revealing the nature of the surface morphology with evidence of micro cavities on the film. Such crucial information obtained on the surface morphology is important to develop our understanding on the spectral nature and the measured low reflectance value.

3.1.3. Optical absorption

The optical absorption study of CNT-based thin films for stray light control applications in space holds paramount significance. In harsh space environment, stray light control is crucial to ensure accuracy and functionality of astronomical observations and satellite-based technologies. CNT-based thin films exhibit exceptional optical absorption properties, allowing them to effectively absorb and attenuate unwanted stray light, reducing background noise and enhancing the sensitivity and precision of space-based instruments. This research not only aids in improving the quality of scientific data collected from space but also enhances the reliability and performance of communication and navigation systems critical for space exploration and satellite operations, ultimately contributing to the advancement of our understanding of the universe and the successful execution of space missions. Additionally, we conducted UV-Vis-NIR absorption

spectroscopy on our composite thin films before and after subjecting them to space environmental simulation tests (SESTs) exhibiting promising results.

3.1.4. Space environmental simulation tests (SESTs)

SESTs are of utmost importance for evaluating the performance and durability of black absorber thin films in the challenging conditions of outer space. These tests replicate the extreme environment that spacecraft and satellite components experience, including intense radiation, vacuum, and extreme temperature fluctuations. By subjecting the black absorber thin films to such simulations, namely thermal vacuum, thermal storage, humidity exposure, thermal cycling etc., we can measure their ability to maintain optimal optical absorption and thermal properties over extended periods. Reliability of such coatings is essential for effective optics used in the lower earth orbit satellites, thermal control systems, solar panels, and in other spacecraft components ensuring overall success in space missions, as well as developing space technology and research. Following exposure of the coatings to these tests, we conduct a repeat UV-Vis-NIR spectroscopy which should ideally be consistent with the results before subjecting the films to SESTs.

3.2. General introduction to the characterizations

Here we introduce the characterization techniques employed in this work and provide their general working principle.

3.2.1. FTIR

FTIR spectroscopy stands as a valuable analytical method employed for investigation of the structural and chemical attributes of materials, including CNTs [28]. This technique operates by examining the interaction between IR radiation and samples, recording frequencies of the absorbed radiation and thus providing information of vibrational alterations within the molecules. FTIR employs a Michelson interferometer, illustrated

in Figure 3.1. The setup includes a semi-transparent mirror and two mirrors, one stationary and one adjustable. A collimated light beam from the source is directed onto the semi-transparent mirror at an oblique angle, resulting in the beam being split into transmitted and reflected components. These two beams bounce off the stationary and adjustable mirrors, travel back to the semi-transparent mirror, recombine, and create an interference pattern. The precise position of the adjustable mirror, known as the optical path difference, determines the specific light interference pattern produced. To calculate the light intensity for each wavenumber, a computer swiftly executes a Fourier transform on the interference data.

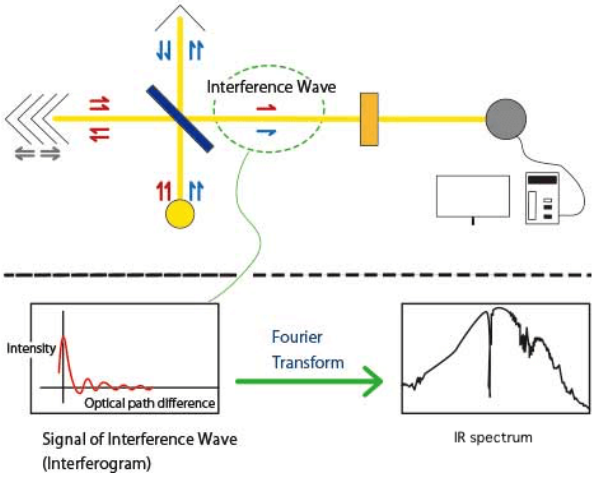

Figure 3.1: Configuration of the FTIR spectroscopy instrument (image courtesy: https://www.jasco-global.com).

FTIR can offer valuable insights into the presence of functional groups and chemical bonds on the CNT surface [124], which is crucial for diverse applications. The resultant FTIR spectrum of CNTs will manifest absorption peaks at specific wave numbers, denominated in cm^{-1}. These peaks are indicative of the vibrational frequencies associated with chemical bonds found within the CNTs and any functional groups adhering to their surface [125,126]. FTIR spectrum is used to identify the presence of functional groups and to quantify the degree of functionalization on the CNTs [37]. Valuable information about the chemical composition is collected from both the intensity

and position of the absorption peaks. In specific cases, FTIR can be employed for quantitative analysis by comparing peak intensities to calibration curves. This analytical method aids in evaluating the success of functionalization processes, assessing purity, and monitoring structural changes in CNTs.

3.2.2. XPS

XPS, also known as electron spectroscopy for chemical analysis (ESCA), is a powerful surface analysis technique used to determine the elemental composition, chemical state, and electronic structure of materials [27]. XPS can provide valuable information about the surface chemistry of CNTs [27], however, proper sample preparation is crucial for accurate analysis. CNTs should be dispersed onto a suitable substrate, such as a silicon wafer or a conductive carbon tape to obtain reliable data.

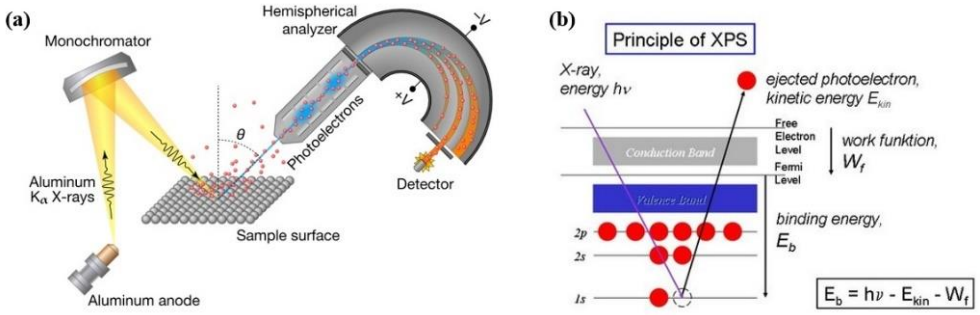

Figure 3.2: (a) Depicts the XPS experimental setup configuration (image courtesy: https://grimmgroup.net/), (b) Presents a fundamental diagram illustrating the principle of XPS (image courtesy: https://www.ifw-dresden.de/).

XPS instrument typically consist of an X-ray source that emits X-rays, an electron analyzer, and a detector. The X-rays are used to excite electrons from the sample's surface, and the energy and intensity of emitted electrons are analyzed to determine the elemental composition and chemical states. Figure 3.2(a) depicts experimental configuration and (b) represents basic principle of working.

In the XPS spectrum of CNTs, the carbon peaks are primarily observed. XPS can also detect oxygen [127] and other elements present in the sample with characteristic peaks at their respective binding energies. XPS can differentiate between sp^2 and sp^3 carbon in CNTs [28,127], that helps to understand the hybridization present. Different carbon bonding environment will result in slightly shifted carbon peaks. Also, quantitative information about the elemental composition of different functional groups attached to the tubes can be acquired by determining their chemical states. The atomic percentages of different elements are calculated based on the peak areas. XPS can be combined with ion sputtering to perform depth profiling to investigate how surface treatments penetrate into the nanotubes [128]. Peak and curve fitting techniques are used for data interpretation to extract information about chemical states.

3.2.3. RAMAN

Raman spectroscopy is a highly effective technique for exploring the vibrational properties and electronic structures of CNTs [129]. When radiation in the NIR or Vis range interacts with a molecule, various types of scattering phenomena can occur, including Rayleigh, Stokes, and anti-Stokes scattering. In all three scattering processes, an incident photon with energy hv elevates the molecule from its vibrational state to one of the countless virtual states situated between the ground and first electronic states. The specific type of scattering observed depends on how the molecule relaxes after this excitation. In Rayleigh scattering, the molecule is excited to any virtual state and subsequently returns to its original state. The photon is scattered elastically, retaining its original energy. During Stokes scattering, the molecule is excited to a virtual state and then relaxes to a higher vibrational state than its initial one. As a result, the scattered photon departs with energy $hv - \Delta E$, representing inelastic scattering. Anti-Stokes scattering occurs when the molecule begins in a vibrationally excited state. It is excited to a virtual state and subsequently relaxes to a lower vibrational state than its initial one. This results in the photon leaving with energy $hv + \Delta E$, representing super-elastic scattering.

Rayleigh scattering is the most common type of transition because it does not necessitate any changes in the molecule's vibrational state. Conversely, the anti-Stokes transition is the least common, as it requires the molecule to begin in a vibrationally excited state before the incident photon interacts with it. Due to the lower intensity of the anti-Stokes signal and the need for filters to eliminate photons with incident energies higher than the desired range. Stokes scattering is typically the primary choice for Raman measurements. Experimental configuration is shown in Figure 3.3(a) and transition diagram in (b).

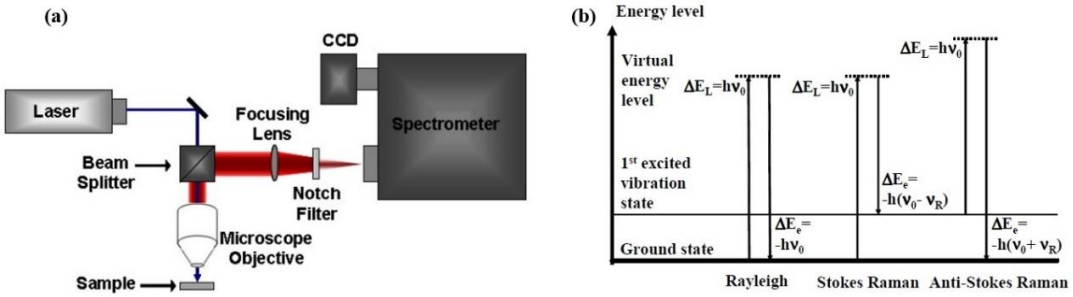

Figure 3.3: (a) Illustrates the configuration of the Raman experimental setup (image courtesy: https://chem.libretexts.org/), while (b) Provides a basic diagram explaining the principle of Raman spectroscopy (image courtesy: non-invasive glucose sensing with Raman spectroscopy, Wei-Chuan Shih et al.).

Raman spectroscopy observes the change in energy between the incident and scattered photons associated with the Stokes and anti-Stokes transitions. This is typically measured as the change in the wavenumber (cm^{-1}), from the incident light source. Raman spectroscopy analysis of CNTs is instrumental in assessing the degree of functionalization by examining the G, D, and $2D$ bands [28]. It also facilitates the investigation of structural distortions through the G band and enhances our comprehension of photon-phonon interactions by studying the $2D$ band. We conducted Raman analysis for the as-prepared, purified, functionalized and coated samples.

3.2.4. XRD

XRD is a powerful analytical technique used to investigate the crystalline structure of materials. Its fundamental principle relies on the scattering of X-rays by the atomic arrangement within a crystal lattice. The X-rays generated from a source, are collimated and directed toward the sample, which can be in the form of a powder, single crystal, or thin film. When the incident X-rays interact with the atoms in the crystal lattice of the sample, they are scattered in various directions. This scattering occurs due to the periodicity of the atomic arrangement which is similar to the diffraction of light waves passing through a narrow slit.

$$n\lambda = 2d\ sin\,\theta \qquad (3.1)$$

Bragg's law, a fundamental equation in XRD [Equation 3.1] describes the relationship between the angles at which diffraction peaks occur (θ), the wavelength of X-rays (λ), and the spacing between atomic planes (*d*). By varying the angle θ and measuring the intensity of the diffracted X-rays, a diffraction pattern is obtained.

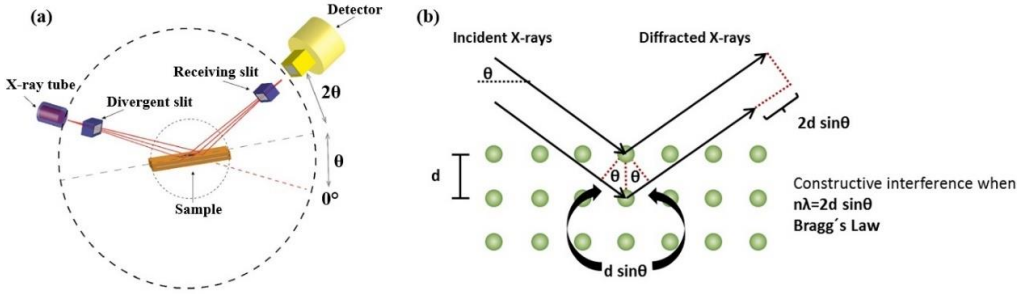

Figure 3.4: (a) Setup configuration for XRD experiment (image courtesy: X-ray diffraction (XRD) of nanoencapsulated food ingredients, Seid Reza Falsafi et al.), while (b) Fundamental diagram elucidating the principle of XRD (image courtesy: https://wiki.anton-paar.com/).

Figure 3.4(a) represents schematic diagram of a XRD set up and (b) demonstrates its working principle. The resulting diffraction pattern, often displayed as a series of peaks, serves as a unique fingerprint of the crystallographic structure of the material. By analyzing the positions and intensities of these peaks, one can identify the crystal

phase(s), determine lattice parameters, and quantify the relative amounts of different phases. MWCNTs and SWCNTs have different diffraction patterns due to their distinct structural arrangements. SWCNTs typically produce a diffraction pattern with a single peak, while MWCNTs exhibit multiple peaks due to the presence of multiple concentric shells. While assessment of the purity of CNT samples, contaminants or impurities may result in additional diffraction peaks that can be detected and analyzed. A well-ordered CNT lattice will produce sharp diffraction peaks, while defects or disorder will broaden the peaks. The impact of functionalization or chemical modifications on the CNT structures can be assessed from the changes in the diffraction patterns due to alterations in the crystal structure by chemical bonding. XRD can also reveal information about the orientation and alignment of CNTs in a material. For example, it can be used to determine if CNTs are randomly oriented or aligned along a specific axis. Changes in lattice parameters due to mechanical deformation or stress, quality control during the production process of CNTs can be ensured by XRD. XRD data can be complemented with Raman spectroscopy to gain a more comprehensive understanding of CNT properties. Raman spectroscopy provides information about vibrational modes and can be used alongside XRD for a more in-depth characterization. X-ray diffraction helps us assess the quality, purity, structural characteristics, and orientation of the carbon nanostructures for the as-synthesized, purified, functionalized and coated samples.

3.2.5. SEM

SEM is a valuable technique for characterizing CNTs and other carbon nanomaterials, allowing researchers to examine their surface morphology, alignment, and distribution. SEM images of samples are typically acquired using detectors that collect either secondary electrons or backscattered electrons. Experimental setup and basic working principle is shown in Figure 3.5.

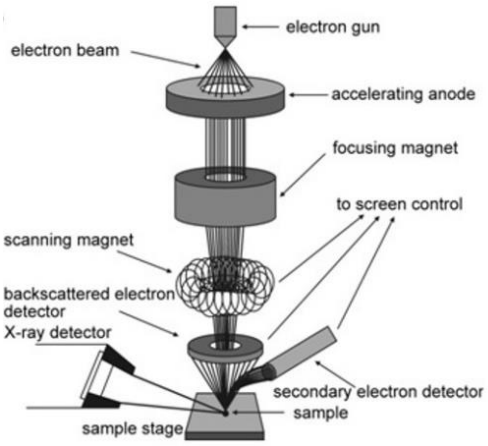

Figure 3.5: Schematic of a typical SEM set up (image courtesy: https://www.technoorg.hu/).

Some electrons of the incident beam excite secondary electrons from the sample providing information about the topography and surface characteristics. Backscattered electrons, which have higher energies than secondary electrons, are also emitted. The intensity of backscattered electrons can reveal variations in atomic number, providing compositional contrast.

To prepare CNT samples for SEM analysis, a suitable substrate, such as a silicon wafer or a conductive carbon tape is used. Drop-casting, spin-coating, or vacuum filtration are the few techniques employed for sample preparation. Coating with a thin layer of conductive material (e.g., gold or platinum) is necessary to improve electron conductivity and reduce charging effects, especially if the sample is non-conductive. CNTs are usually conductive so there is no need for extra conducting layer deposition. Energy dispersive X-ray spectroscopy (EDS) can be combined with SEM to analyze the elemental composition. EDS detects characteristic X-rays emitted from the sample when the incident electrons interact with the CNT atoms. This allows for qualitative and quantitative elemental analysis. SEM-EDS mapping can be employed to visualize the spatial distribution of elements within the CNTs or between CNTs and other materials. This is useful for studying impurities, functionalization, or catalyst particles associated with CNTs. Modern SEM instruments can achieve high-resolution imaging, enabling researchers to probe individual CNTs and investigate their structural properties, such as

diameter, length, and alignment. It's important to be aware that the high-energy electron beam used in SEM can potentially damage CNTs or induce artifacts. Therefore, a carefully choice of the beam energy, beam current, and exposure time to minimize the damage, especially for sensitive samples is required. SEM plays a crucial role in our study of CNT-based materials by providing valuable insights into their structural properties and surface attributes.

3.2.6. AFM

AFM is a versatile powerful imaging technique and widely used in scientific and engineering fields for studying surfaces and materials with high spatial resolution at the nanoscale. The experimental set up of an AFM is shown in Figure 3.6. A fine-tip, affixed to a cantilever, meticulously scans over the surface and delicately oscillates to maintain a constant force, providing precise mapping of the surface topography.

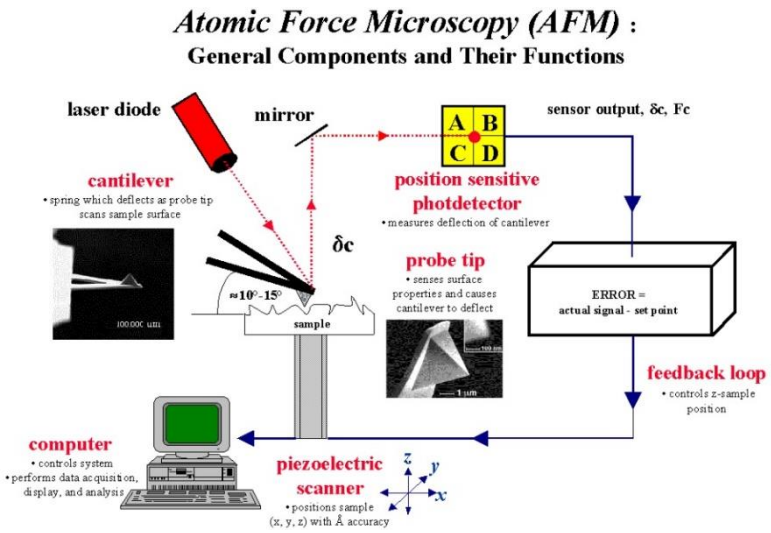

Figure 3.6: Experimental configuration for conducting AFM experiment (image courtesy: https://lnf-wiki.eecs.umich.edu/).

AFM can provide detailed information about the surface features, including roughness, height variations, adhesion forces of materials, hardness etc. Individual CNTs can be mapped, allowing precise assessment on diameter, length, and their arrangement on the

substrate. The AFM tip can be used in manipulating and positioning atoms, molecules, CNTs and other nanoscale objects with high precision for assembling nanostructures and studying molecular interactions. It can also study mechanical characteristics of the samples through force-indentation experiments. Conductive AFM (C-AFM) facilitates the spatial mapping of electrical conductivity, while it can be paired with complementary technique such as infrared spectroscopy for information on functionalization, defects, and chemical interactions at the nanoscale. In our study, AFM provides profound insights into the surface morphology of the coated films by revealing signature of micro cavities and pores on the surface, controlling immensely the spectral properties of these films.

3.2.7. HRTEM

In HRTEM, transmitted electrons interact with atoms within the sample via elastic and inelastic scattering. It is a powerful imaging mode of transmitted electrons that allow direct imaging at the atomic scale providing information on different properties of semiconductors, metals, nanoparticles and sp^2 bonded carbon e.g., CNTs, graphene etc. The resolution of HRTEM can be as low as 0.5 Å [130], making it one of the most useful tools to probe atoms and defects. Electrons that undergo inelastic scattering have a change in energy after they are transmitted through the sample, whereas elastically scattered electrons maintain their initial transmitted energy and therefore, can be more useful for the final data interpretation. The electrons that undergo elastic scattering leave the sample and move through the lenses of the microscope to form the high-resolution image as shown in Figure 3.7. Inelastically scattered electrons are not normally used in this technique but they can produce data from the sample using a technique called electron energy loss spectroscopy ($EELS$).

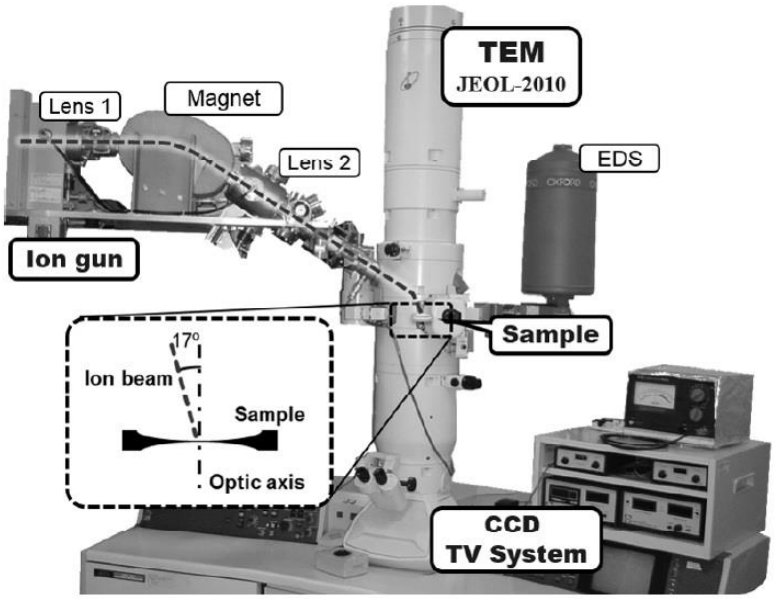

Figure 3.7: A schematic representation of the experimental setup of HRTEM with an ion gun (image courtesy: in situ transmission electron microscope observation of the formation of fuzzy structures on tungsten, M Miyamoto et al.).

HRTEM provides crucial insights of the as-prepared and purified samples, such as successful elimination of FeNPs and the emergence of nanoscrolls [28]. Additionally, micrographs of the functionalized samples reveal the attachment of functional groups and evidence of unzipping. Observations obtained on the coated films allow us to discern various low-dimensional structures [28].

3.2.8. UV-Vis-NIR absorption

UV-Vis-NIR spectroscopy stands as an effective analytical method for assessing the optical attributes, including transmittance, reflectance, and absorbance of both liquid and solid substances. Its versatility extends to the characterization of various materials employed in research and manufacturing, such as semiconductors, coatings, and glass. This technique operates within the optical spectrum spanning from 175-3300 nm. UV-Vis-NIR spectroscopy is commonly employed for quantifying analyte concentrations or monitoring the chemical transformation of a constituent within a solution. This method assesses light absorption throughout the specific optical range of interest. To execute the

analysis, a sample is introduced into a cuvette, which is then positioned along the trajectory between the optical light source and a detector. By adhering to the principle of the Beer-Lambert law [Figure 3.8], and with a consistent path length for light and a known absorption coefficient (which varies with wavelength), it is possible to ascertain the concentration of a specific compound by evaluating the light absorbed at that particular wavelength.

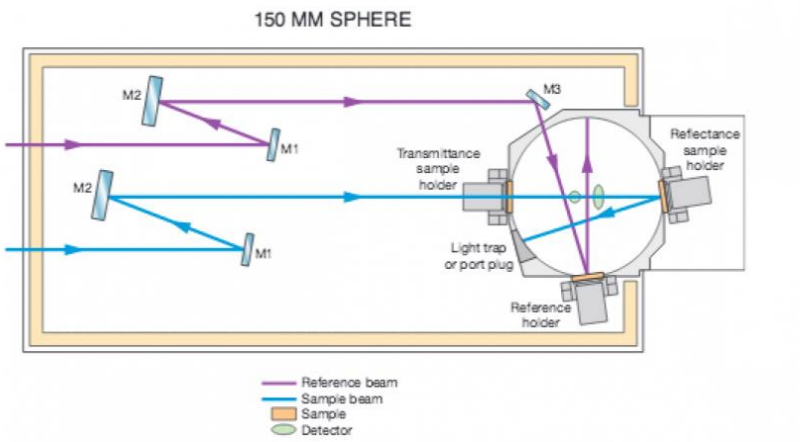

Figure 3.8: Design of a 150 mm integrating sphere for optical measurements. (image courtesy: https://www.mri.psu.edu/).

3.2.8.1. Measuring solid sample reflectance

The sample is situated behind the integrating sphere. Light from the optical source is first reflected by the sample and then by the internal surface of the integrating sphere before reaching the detector. Alongside overall reflectance, it is also possible to measure diffuse reflectance [Equation 3.2]. Specular reflectance data can be deduced by subtracting the diffuse reflectance from the overall reflectance:

$$R_{spec} = R_{overall} - R_{diff} \qquad (3.2)$$

where, R_{spec}, $R_{overall}$ and R_{diff} represent specular, total and diffused reflectance respectively.

In similar way, transmission study also can be conducted for required samples.

3.2.8.2. Calculating solid sample absorbance

Absorbance percentage is a measure of the incident beam absorbed by the sample, excluding the portion that is either reflected or transmitted [Equation 3.3]. Absorbance can be computed using the reflectance and transmittance data:

$$\%A = 100\% - \%R_{overall} - \%T_{overall} \qquad (3.3)$$

where, A, $R_{overall}$ and $T_{overall}$ represent absorption, total reflectance and total transmittance respectively.

CNTs exhibit unique optical properties in the UV, Vis and NIR regions. The absorption of CNTs in these regions is primarily governed by their electronic structure [59,125]. CNTs typically have strong UV absorption (200-400 nm) which is attributed to transitions involving the π-electron orbitals along the tube axis. The intensity of UV absorption depends on factors like CNT diameter, chirality (the specific arrangement of carbon atoms in the tube lattice), and the presence of defects or functionalization. In the visible region (400-750 nm), CNTs can exhibit distinct absorption peaks or bands. The exact position and intensity of these absorption features depend on the CNT structure. The transitions involved are associated with the electronic energy levels of CNTs. Absorption in the NIR region (750-2500 nm) is attributed to phonon resonances which involve vibrational modes of the CNT lattice and the electronic transitions are less pronounced. The absorption characteristics of CNTs can vary significantly depending on their specific structural properties and any surface modifications or functionalizations [59]. We used UV-Vis-NIR spectroscopy to study and characterize these absorption properties of carbon nanomaterials based composite thin films before and after subjecting to the SESTs [28], which can provide valuable insights into the stability and optical behavior of these materials for stray light control space applications.

3.3. Conclusion

It is very important to carry out the characterizations step-by-step. Omission of any of them may result in critical loss of information effecting our understanding. We gain insights into chemical behavior and composition through FTIR, XPS, Raman, and XRD, while, morphology examinations are effectively conducted using SEM, HRTEM, and AFM investigations. UV-Vis-NIR absorption study aid in verifying the desired absorption targets, and post-SESTs offer insights into the durability of these coatings in drastic space conditions.

CHAPTER 4

Methodology

Experimental details, techniques followed and the procedures employed in the work will be presented here.

4.1. Introduction

SWCNTs produced by HiPCO method [79,131] had a catalytic content of <0.05% Fe, diameter of 0.6-1.1 nm and length of ~400-1000 nm. The morphology of the SWCNTs was a dry black powder with carbon as SWCNTs > 96%. The synthesis method yielded nanotubes with a range of diameters and chirality, which usually contained metallic and amorphous contaminants. Therefore, post-synthesis chemical purification was required to eliminate these contaminants for further use.

4.2. Purification

We implemented a three-stage purification procedure that includes wet oxidation at 300℃, an acid treatment with concentrated HCl [132–134], and annealing at 900℃ in an inert atmosphere [100,135].

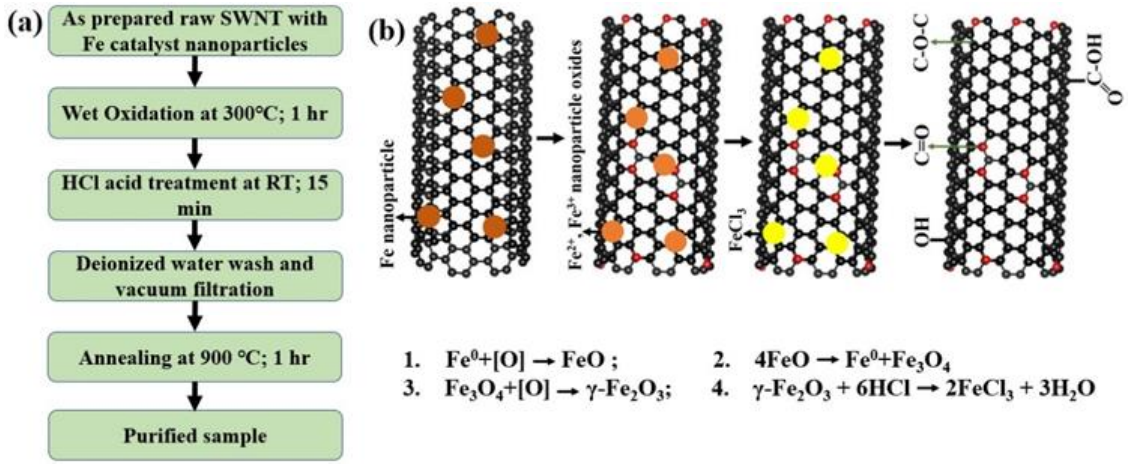

Figure 4.1: Schematic of the purification process. (a) Flow chart depicting the process step by step, and (b) pictorial presentation of the oxidative attachment of the functional groups on the side walls of the CNTs and the related chemical equations involved during the purification process.

Figure 4.1(a) shows the stepwise schematic of the purification process, while Figure 4.1(b) illustrates the chemical alterations that might take place on the tube surfaces as a result of oxidative acid reflux [136]. Following wet oxidation for one hour, FeNPs initially adhered to both the side walls and to the end of the CNTs, underwent transformation into iron oxides. Subsequently, when subjected to HCl acid treatment, these iron oxide impurities were converted into soluble ferric salts in the presence of H^+ and Cl^- ions. This process is depicted in Figure 4.1(b), and Figure 4.2. In Figure 4.2, we show the process of the cracking of carbon shells around the FeNPs.

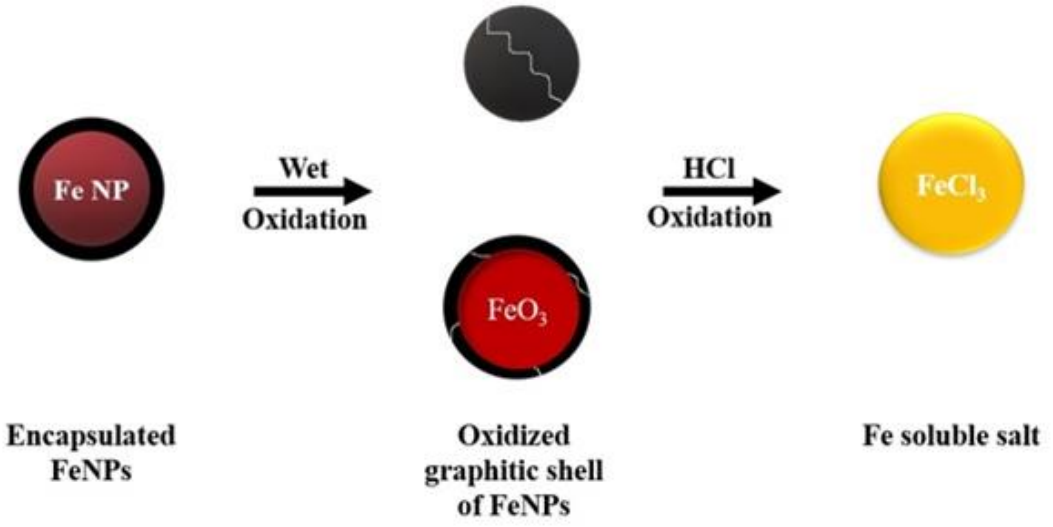

Figure 4.2: Schematic of cracking of carbon shell surrounding FeNPs by wet oxidation and removal of FeNPs and amorphous carbon transforming into a soluble ferric salt after HCl treatment.

Through several rinses with DI water, these salts can be effectively removed. The resulting purified product can be obtained by completion of neutralization and drying processes at room temperature (RT). The chemical reactions occurring during the purification process are given at the bottom of Figure 4.1(b).

Purification is followed by functionalization of the CNTs and is discussed below.

4.3. Functionalization

To carry out the functionalization process, we had taken concentrated H_2SO_4 and HNO_3 with a volume ratio of 3:1 and black powder of purified sample in a beaker. The mixture was stirred using a magnetic stirrer at a temperature of 70 ℃ for 8 hours and allowed to cool down to RT. The mixture was then neutralized by rinsing with DI water until neutral pH is obtained. The functionalized powder was obtained by sieving the solution using Whatman filter paper. The sieved powder was dried under vacuum at RT. A schematic of the functionalization process is shown in Figure 4.3.

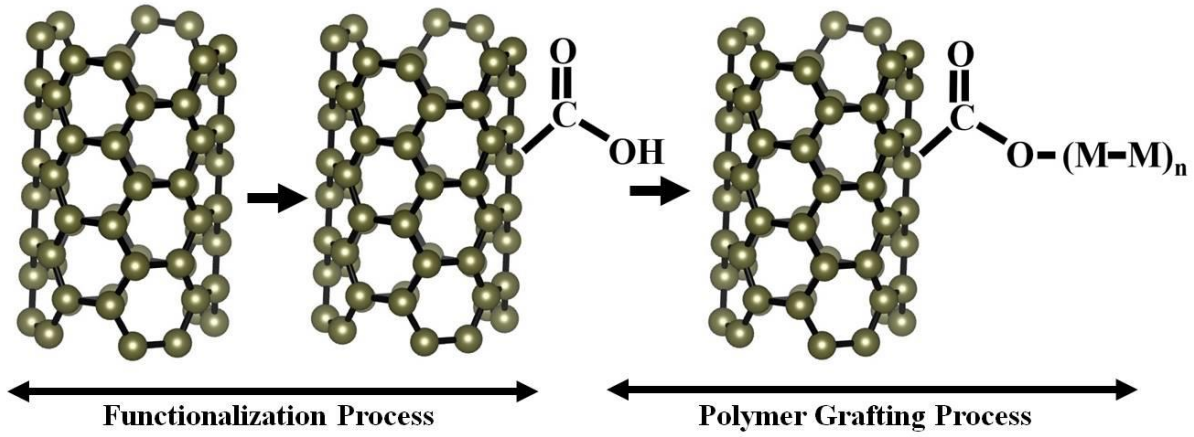

Figure 4.3: Schematic representation of the functionalization and polymer grafting processes. The attachment of carboxyl group $(-COOH)$ after the functionalization, is followed by polymer grafting process with hydrocarbon chains, $-(M-M)_n$.

4.4. Spray coating

The functionalized powder was mixed with a weighted amount of polyurethane binder and a solvent and ultrasonicated for 60 minutes using ultrasonic probe sonicator Q500 from Q-Sonica in order to obtain a well-dispersed agglomeration-free solution. The solution, thus obtained was spray-coated [Figure 4.4] on a cleaned aluminium (Al)

substrate using a hand airbrush Pilot AB16 in a glove box under a controlled nitrogen atmosphere.

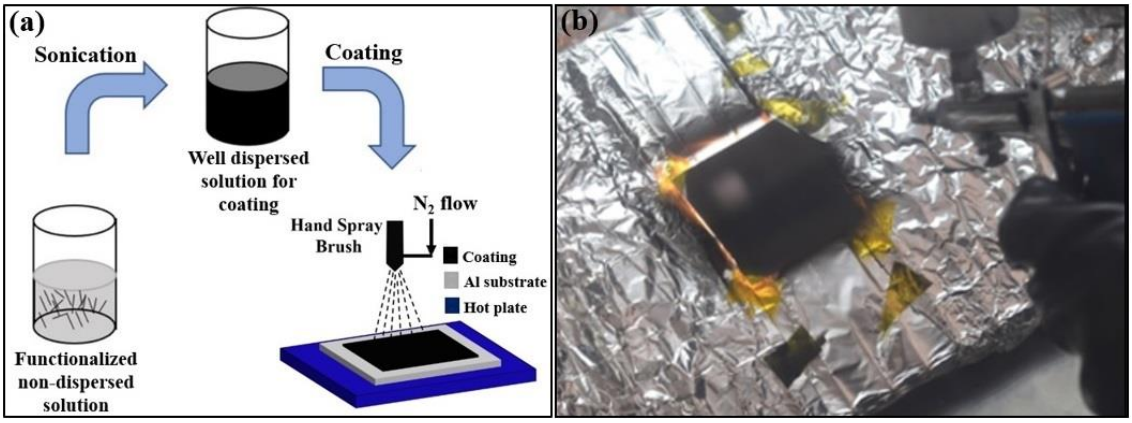

Figure 4.4: (a) Schematic representation of different stages of coating process and (b) image of in-situ hand spray coating process.

The Al substrate was preheated to a temperature of around 300℃ by a quartz radiant heater attached with a PID controller to maintain the temperature within a range of 300 ± 10℃ during the spray coating process. The temperature was monitored using a thermocouple. After the deposition of the film, samples were allowed to cool down to RT.

4.5. Characterizations

Different characterization techniques were used to understand the step-by-step structural and chemical modifications, as well as the spectral properties of the coated films. The purified and functionalized CNTs were first subjected to functional group analysis by FTIR spectroscopy. The infrared absorption spectra of the CNT pellets prepared using KBr powder were measured in the range of 4000-500 cm^{-1} using a PerkinElmer Spectrum GX spectrometer. For the XPS measurements, an AXIS Ultra DLD spectrometer was used to study chemical composition of the post-treated samples.

Measurements were carried out using monochromatic Al K_α (1486.3 eV) X-ray source operating at 117 W power. Survey spectra were acquired with a pass energy of 160 eV, whereas, for high-resolution $C1s$ and $O1s$ spectra, a pass energy of 20 eV with a step size of 0.1 eV was used. The $C1s$ peak corresponding to adventitious carbon on the surface was set at 284.6 eV to correct the charging effect and accordingly giving a shift to the obtained spectra. Data were analyzed using Shirley background correction and Gaussian / Lorentzian function with GL line shapes of varying FWHM for component peaks. Shirley background is the most common method of non-linear background subtraction, which considers the background at any point due to inelastically scattered electrons and is proportional to the integrated photoelectron intensity to higher kinetic energy [3]. The vibrational spectroscopy measurements of the purified, functionalized, and spray-coated samples were carried out by subjecting them to Raman spectroscopy analysis using a LabRam HR 800 instrument with 532 nm wavelength of Nd-YAG laser High Resolution TEM measurements were carried out by drop-casting the sample on Cu grids using an FEI-Titan Themis instrument operated at 300 kV. The morphology of the samples was investigated by field-emission SEM on a Zeiss SEM Ultra55. AFM measurements were carried out using a Bruker Dimension ICON AFM in tapping mode (amplitude modulation mode), which helped minimize the effect of friction and other lateral forces in the topography measurements. XRD measurements were carried out using a Smartlab X-ray diffractometer by Rigaku. The data was collected using monochromatic Cu K_α radiation (1.54 Å) at 40 kV and 30 mA. The spectral properties of the spray-coated samples were analyzed using a UV-VIS-NIR spectrometer, PerkinElmer Lambda 950 in the wavelength range of 400-2500 nm. The spray coated samples were subjected to SESTs using the environmental test facilities available at LEOS, Bengaluru. Figure 4.5 illustrates the work plan, indicating the characterizations conducted at each stage.

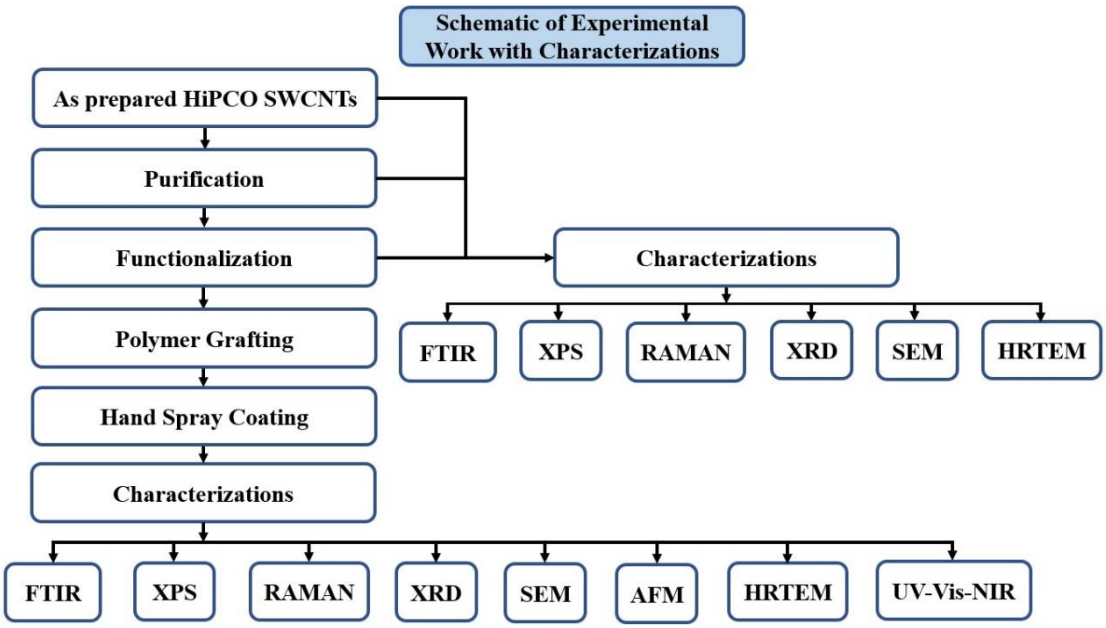

Figure 4.5: Flow chart of the work methodology followed in this study.

4.6. Conclusion

In this chapter, we have discussed the methodologies employed in the study, shedding light on the experimental techniques adapted and the details of the instruments used. Purification, functionalization, polymer grafting and hand spray coating contribute to the chemical and morphological evolution of the as-prepared SWCNTs to different low dimensional derivatives (discussed in upcoming chapters). We have elaborated here on the details of the characterizations that are used to develop a proper understanding of the results.

CHAPTER 5

Chemical, structural and vibrational spectroscopy study of carbon nanomaterials

In this chapter, we present our results on FTIR, XPS, XRD, and Raman spectroscopy revealing chemical and structural modifications to the as-prepared HiPCO SWCNTs during purification, functionalization and coating processes.

5.1. Introduction

We address here chemical attachment of different functional groups, modifications in the crystal structure and the changes in the vibrational spectroscopy due to purification and functionalization. Earlier reports show different methods proposing significant enhancement to the adsorption properties of SWCNTs by creating low-energy sorption sites capable of binding diverse functional groups [137]. These modifications have a profound impact, particularly the defects created on the CNT walls act as active nucleation sites for additional condensation of chemical vapors from various organic binders and solvents. The change, thus occurring in the surface chemistry, is instrumental in manipulating the properties and enhancing the adsorption characteristics of the CNTs, as well as other carbon nanomaterials. We investigate the chemical and physical modifications by performing FTIR, XPS, XRD and Raman spectroscopy measurements.

5.2. Results and discussion

5.2.1. FTIR

FTIR is a versatile non-destructive technique for the identification and characterization of the chemical structure of the sample. Normalized FTIR spectra of the purified and functionalized samples are shown in Figure 5.1. The chemical incorporation of various functional components is well evident in the FTIR investigations [Figure 5.1]. After the sulpho-nitric functionalization process, further attachment of oxygen (O), nitrogen (N), and sulphur (S) containing functional groups can be seen by significant increase in the intensity of the bands, as well as addition of new band features appearing in the functionalized spectrum.

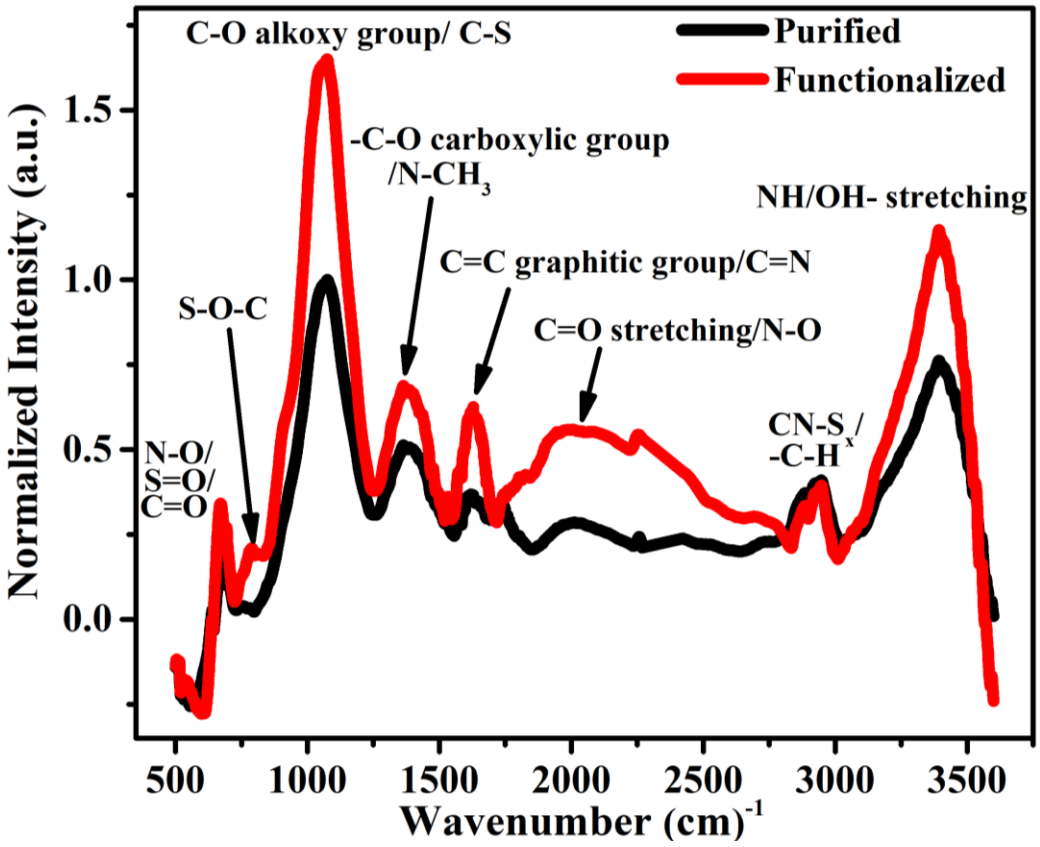

Figure 5.1: FTIR spectra of purified and functionalized samples. Both the spectra are normalized w.r.t. the maximum intensity of the purified sample data.

The absorption feature obtained at 3393 cm^{-1} [Figure 5.1] in the functionalized spectrum is assigned to the $-OH$ stretching mode of the $-COOH$ group [126,138]. Features at 2940 cm^{-1} and 2878 cm^{-1} correspond to the $-CH$ stretching vibrations attributed to methylene group of $-S(CH_2)_4SH$ [139,140], whereas, the peak centered at 2914 cm^{-1} is ascribed to residual $N-H$ components and $-OH$ bands corresponding to uncondensed amino groups and surface-adsorbed H_2O molecules [141]. The band around 2800-3000 cm^{-1} can be associated with the symmetric and asymmetric stretching vibrations of the $C-H$ bond which is an indication of the addition of oxygen containing functional groups during the systematic processes of purification and functionalization [20,28]. The broad absorption band between 2734-1734 cm^{-1} is related to aldehyde

(2750 cm^{-1}, $= C - H$ stretching mode); signature of nitrile (2250 cm^{-1}, $-C \equiv N$ band, which can be due to presence of small amount of nitrogen in the sample during treatment with HNO_3); weak presence of alkyne (2150 cm^{-1}, $-C \equiv C -$ band) and strong signature of $-C = O$ stretching (1734 cm^{-1}) [142]. Also, emergence of a shallow feature in between 1746-1870 cm^{-1} within the broad absorption band mentioned above is assigned to $-N = O$ bond stretching [143], as well as stretching of $-C = O$ within the anhydride group $[-(CO)_2O]$. The relatively strong peak feature centered at 1626 cm^{-1} can be associated with the stretching of $C = C$ graphitic group [144] and N atoms covalently attached to the C network $(C = N)$ [144]. The stretching and bending of $-C = O$ bonds in the carboxyl, epoxy $(-C - O - C-)$ and hydroxyl are mostly contributing to the broad absorption feature centered at around 1384 cm^{-1} [12,144,145]. The prominent band, peaking at 1375 cm^{-1} is attributed to the $-C - O -$ stretching or to the contribution of nitrate species [145] corresponding to the carboxylic group. A strong band emerging between 1250-1600 cm^{-1} is attributed to the substitution of an N atom in place of a C atom in a sp^2 hybridized C network [146]. The peak at 1364 cm^{-1} corresponds to $N - CH_3$ bond stretching [146], while the peak at 1075 cm^{-1} and the features visible at 789-825 cm^{-1} are assigned to $C - S$ bond stretching and $S - O - C$ bond stretching, respectively [147]. After functionalization, the peak at 1067 cm^{-1} which was previously associated with the $-C - O$ alkoxy group stretching [144,148], has become more intense due to the attachment of sulphate functionalities and its vibration [147]. The deformation of the hydroxy functional group $(-OH)$ presents as a peak feature at 1078 cm^{-1} [28]. The absorption band at 671 cm^{-1} is ascribed to the $-C = O$ group stretching [144,148] and presence of sulfate ions (internal vibration of the (SO_4^{2-}) adsorbed on the carbon surface [149]. Evidence of various bands present in the purified sample ensures integration of different functionalities during the chemical purification process [150]. After functionalization, intensity of many bands has enhanced along with emergence of new bands [Figure 5.1], indicating a successful functionalization process.

5.2.2. XPS

High resolution XPS measurements carried out on the samples are shown in Figure 5.2. Figure 5.2(a) and (b) correspond to $C1s$ and $O1s$ lines of the purified sample. Deconvoluted $C1s$ spectrum [Figure 5.2(a)] exhibits feature peaking at around 284.6, 285, 286, 287 and 289 eV which we assign to $C = C$ sp^2 [151], $C - C$ sp^3 [152], $C - O$ alkoxy groups [151], $C = O$ carbonyl [153] or epoxy $-C - O - C -$ [154] and $-O - C = O$ carboxyl groups [151,155] respectively.

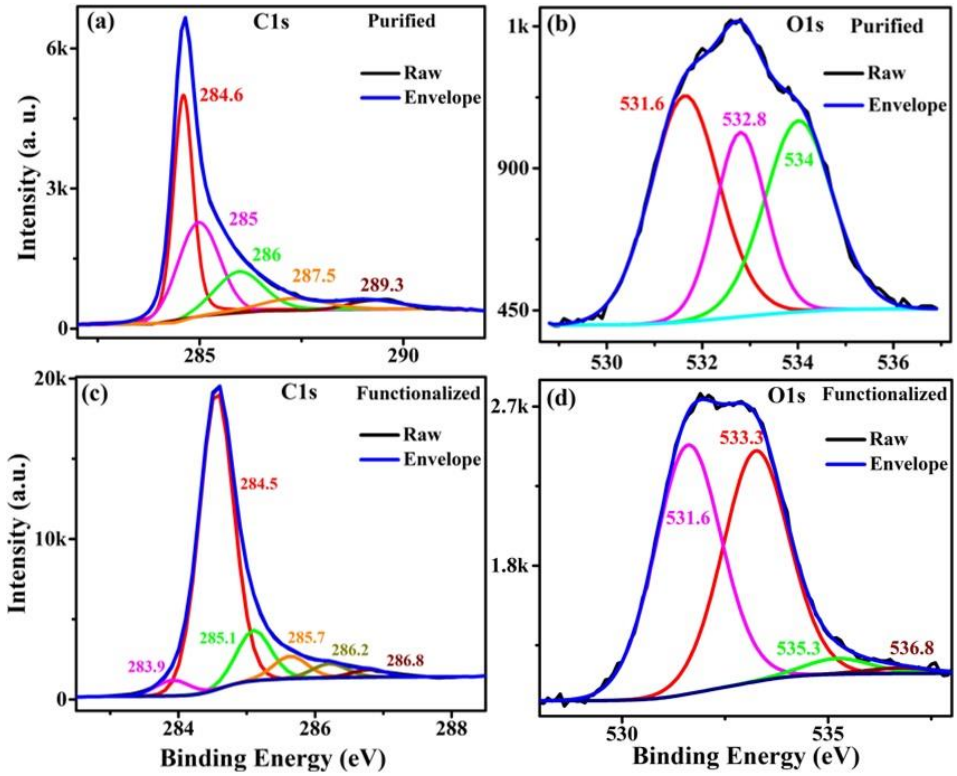

Figure 5.2: High resolution XPS spectra (a) $C1s$ and (b) $O1s$ for purified sample. (c) $C1s$, (d) $O1s$ for the functionalized sample.

The fitted $O1s$ spectrum [Figure 5.2(b)] displays contributions at 531.6, 532.8 and at 534 eV that are assigned to $-C = O$ functional group (531.6 eV) [151], ether type oxygen $-C - O -$ [156], or $-C - O - C -$ epoxy signature (532.8 eV) [157], and $-C - OH$

bonds [151], [158] or H_2O molecules (534 eV) that are trapped during the synthesis process [159].

The $C1s$ and $O1s$ core level spectra of functionalized sample are shown in [Figure 5.2(c, d)]. $C1s$ line exhibits 5 contributions at 283.9, 284.5, 285.1, 285.7, 286.2 and 286.8 eV [Figure 5.2(c)]. The peak at 283.9 eV is attributed to defective and oxidized graphite and MWCNTs [160], while the 284.5 eV peak is ascribed to graphitic $C = C$ sp^2 carbon [154]. The maximum observed at 285.1 eV could be due to $C - C$ sp^3 or $C - H$ [161,162] and the line at 285.7 eV could be due to $C - O$ and $C - OH$ functionalities or characteristic of the $C - N$ bond with sp^2 hybridization [163]. The contribution at 286.2 eV is typical of carbon making a single bond with oxygen representing alkoxy group or with nitrogen $[-C - (O, N)]$ [164]. The peak at 286.8 eV could be the characteristic of $C = N$ with sp^3 hybridization [164] or the $C = O$ carbonyl [155,165] or the epoxy $C - O - C -$ group [156].

The $O1s$ spectrum of functionalized sample reveals four peak features centering around 531.6, 533.3, 535.3, 536.8 eV after the deconvolution [Figure 5.2(d)]. The first peak at 531.6 eV is assigned to $-C = O$, group of carboxylic groups ($COOH$) denoted as $C - OH$ [166], or sulfonic group ($R - S(= O_2) - OH$) [167]. The peak at 535.3 eV could be the contribution coming from O in H_2O [168,169] and the feature at 536.8 eV is ascribed to the oxygen bonded to sulfur in sulfuric acids [170].

5.2.3. XRD

The XRD investigations carried out on the different CNT samples are shown in Figure 5.3 and 5.4. As-prepared sample [Figure 5.3] having measure contributions at 26.32° and 44.1° which correspond to the abundance of graphitic (002) character [140] and FeNPs impurities [140] respectively.

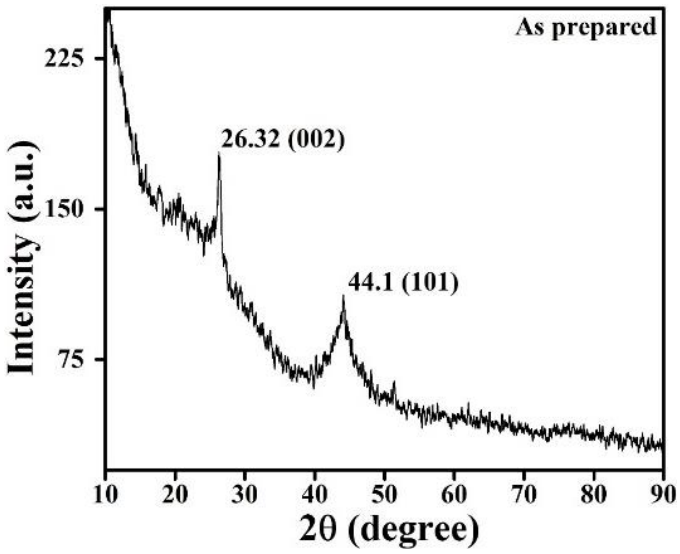

Figure 5.3: XRD spectrum of the as-prepared sample.

In Figure 5.3, the graphitic peak is notably prominent in the as-prepared sample as anticipated. The high background in the as-prepared data indicates a significant presence of amorphous carbon and metal impurities [171]. The characteristic (002) peak of the carbon-based materials is observed [Figure 5.4] at around 26º.

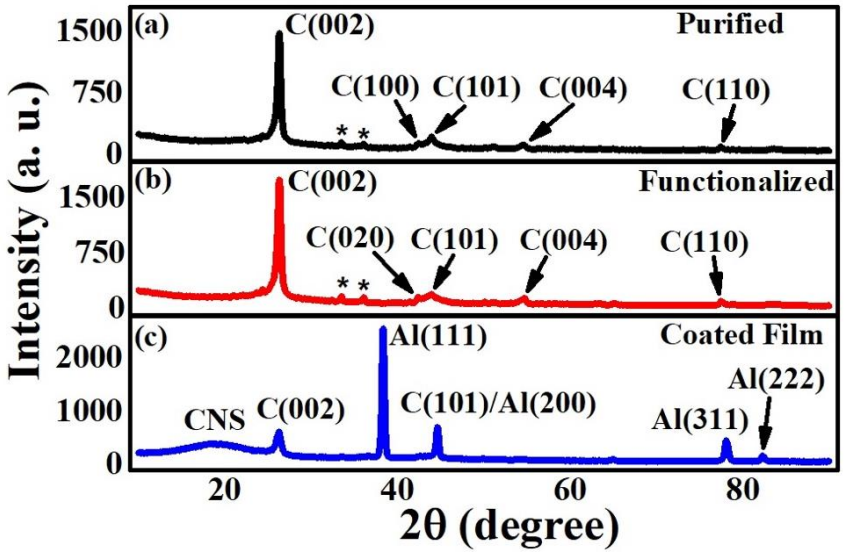

Figure 5.4: XRD data of (a) purified, (b) functionalized and (c) coated film.

The intensity and width of the (002) peak (JCPDS card no. 01-075-1621) are related to the number of layers, the orientation of the CNTs, and the content network distortion [140]. High intensity of the (002) peak and small value of the FWHM [Figure 5.4(a, b)] indicate good crystalline quality of the purified and functionalized samples.

Purified sample [Figure 5.4(a)] shows up small peaks at around 42º and 44º which correspond to the (100) and (101) graphitic planes respectively (JCPDS card no. 01-075-1621) [Figure 5.3 and 5.4(a)]. In addition, peak-like features observed at 33.5º and 36.2º (indicated in the images by stars) in the purified spectrum can be associated with the Fe catalyst impurities [172] attached to the CNTs [143], while the peaks at 54.6º and 77.5º correspond to the (004) and (110) planes of the graphitic layers (JCPDS card no. 01-075-1621). The XRD data obtained for the functionalized sample is shown in Figure 5.4(b). We could hardly find any difference in the peak positions of the graphitic planes between the purified and the functionalized samples; however, a slight variation in the intensity of the peaks is observed, which can be associated with further de-bundling and better dispersion of the CNTs. The XRD data of the coated film exhibit signatures of the graphitic components and the Al substrate. The graphitic planes of (002) and (101) at 26º and 44.6º respectively are observed with a lower intensity compared to that of the functionalized sample. Generally, the polymer grafting process of the coated film will lead to an apparent decrease in the intensity of the graphitic planes [173,174]. The peaks at 38.3º, 78.1º and 82.3º are assigned to the (111), (311) and (222) planes of the Al substrate respectively [175]. The broad onset peak at around 18º is attributed to the presence of the CNS and other structural components in the sample [175]. It has been reported that due to the residual solvent trapped between the graphitic layers of different structures, there may be an expansion in the interlayer spacing, giving rise to a distribution that contributes to a broad onset at around 15-18º [175].

5.2.4. Raman spectroscopy

Raman measurement, which is very sensitive to the chiral indices (*n*, *m*), is naturally considered to be an important spectroscopic tool to characterize CNTs.

Normalized Raman spectra of as-prepared, purified, functionalized and coated film are shown in Figure 5.5 and 5.6. Distinct signature of radial breathing modes (RBM) unique to the SWCNTs are observed in the as-prepared [Figure 5.5], purified and functionalized data [Figure 5.6].

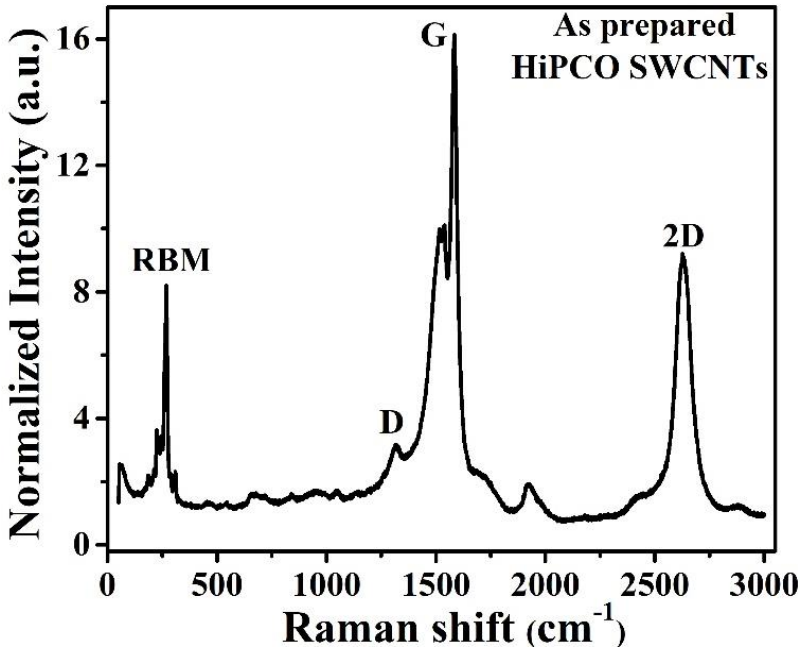

Figure 5.5: Raman spectrum of as-prepared HiPCO SWCNT sample representing prominent characteristics of RBM and G peaks along with low peak feature of D band. The spectrum is normalized w.r.t. the G peak of the purified sample.

Presence of characteristic G and $2D(G')$ bands of graphitic materials with high intensity are also visible in the spectra. RBMs are associated with the A_g symmetry of the carbon atoms that move in-phase in the radially outward direction, while G-band corresponds to an optical phonon mode, representing in-plane tangential vibrations of sp^2 bonded carbon in graphitic materials. These vibrations are schematically shown in Figure 5.7. The characteristic RBMs of SWCNTs usually occur in the range of 120-350 cm^{-1} for tubes with diameter ranging from 0.7-2 nm [176]. We observe manifestation of RBMs in the samples between 150 and 350 cm^{-1} [Figure 5.5, 5.6(a, b)].

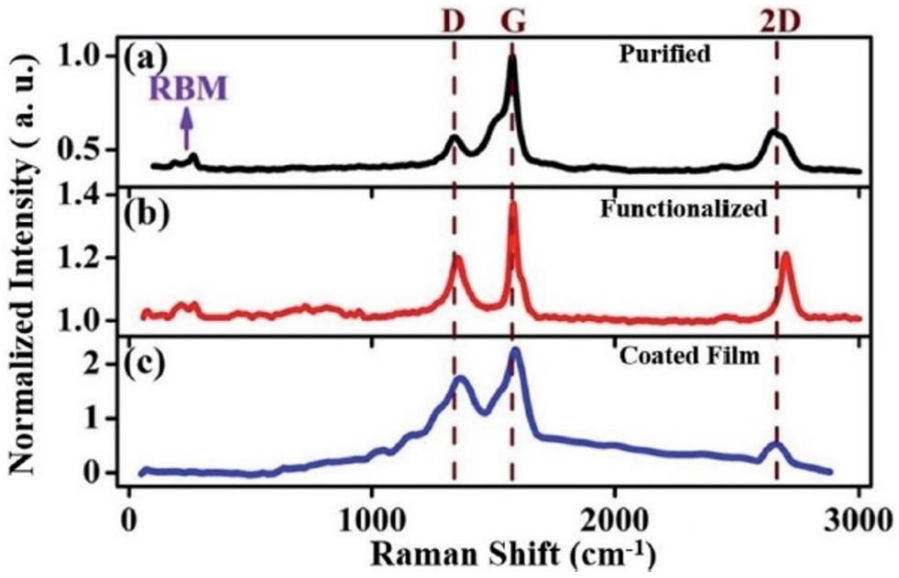

Figure 5.6: Raman spectra of (a) purified (b) functionalized and (c) coated film. The spectra are normalized with respect to the G peak of the purified data shown in (a).

Presence of well-defined RBMs, especially in the as-prepared and purified data indicate high purity of the SWCNTs with a very low concentration of defects. A feeble D band in the as-prepared and purified data further supports this evidence [Figure 5.5, 5.6(a)]. The $2D$ or G' band is a Raman-allowed signature by symmetry, and not a defect induced one [177].

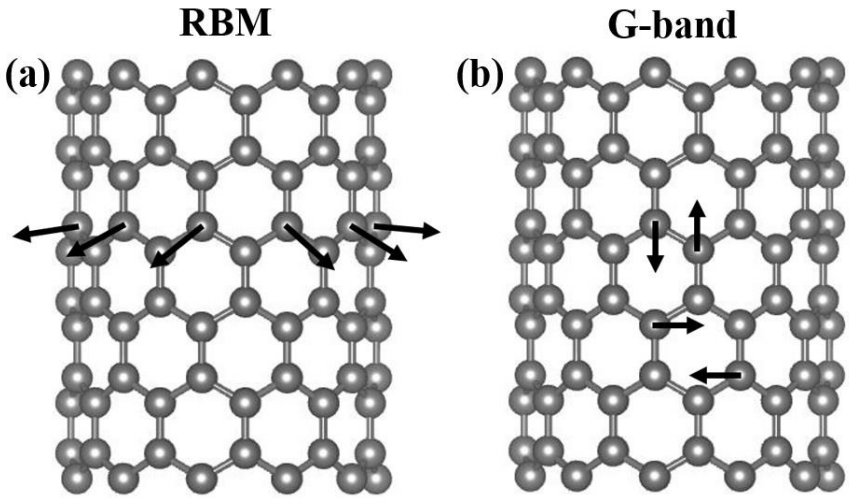

Figure 5.7: (a) RBM vibrations directed radially outwards and (b) in-plane vibrations of G-band in SWCNTs.

As we progress through purification, functionalization and coating processes, the intensity of the D band gradually increases. This is attributed to the inclusion of defects, dislocations, impurities, as well as transformation of sp^2 hybridization to sp^3 during the processing steps [154–157].

The D peak, which corresponds to the breathing modes of the A_{1g} symmetry around the K points of the Brillouin zone, is forbidden in an ideal graphitic structure and requires structural defects for a phonon of certain angular momentum to be activated. Consequently, the signature of the D band is a measure of non-crystalline disorder, lattice distortions and defects associated with the CNTs, whereas a higher intensity of the G band compared to D is a manifestation of superior graphitic crystallinity in the sample. Further confirmation of the formation of CNS and MWCNT can also be drawn from the D, G and $2D$ bands.

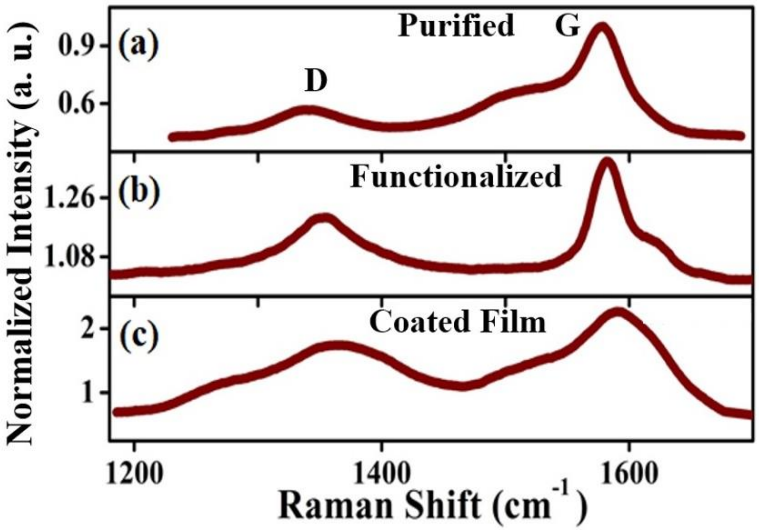

Figure 5.8: D and G mode vibrations in (a) purified, (b) functionalized and (c) coated samples. The intensity of the spectra was normalized with respect to the G peak of the purified data shown in (a).

The presence of CNS and gradual induction of defects on the sidewalls of the raw SWCNTs during the processing treatment [178,179] can be directly associate with the D peaks, which consequently exhibit an increase in intensity [Figure 5.8] and full width at half maximum (FWHM) (59.7, 65.84 and 149.29 cm^{-1}) [Figure 5.8] from the purified sample to the coated film. CNS with their long unfused edges contribute to enhancing the D peak intensity [180]. The clear up-shift in the D peak positions (1343.66, 1353.79 and 1363.52 cm^{-1}) indicate an increase in the diameter of the curved-sheets/ nanoscrolls/ nanotubes from the purified to the coated film. The intensity ratio of the G to D band (I_G/I_D) decreases after functionalization, which is attributed to the distortion in the graphitic structure, elongation of the $C-C$ bond due to the electron transfer, and increase in the sp^3 C hybridization in comparison to the sp^2 C [179,181–183]. The purified sample shows the lowest [Figure 5.10(a)] D band intensity (I_D) and highest I_G/I_D ratio, while the coated film has the most intense D feature [Figure 5.8(c)] with the smallest I_G/I_D value. The I_G/I_D ratio of the functionalized sample [Figure 5.8(b)] is in the middle. The position of the G band is also important, which is highly dependent on the elastic strain. Due to

the rolling and curling of the sheets, elastic strain develops in the system, which has an inverse relation to the diameter of curvature [180]. Consequently, a downward shift in the G peak position can occur with an increase in the diameter of the rolled sheets. A small down-shift and broadening of the G band is observed for the coated film compared to that of the functionalized sample, indicating the presence of a larger diameter of curvature and varying elastic strain, respectively, in the sample. Acid treatment of the graphitic sheets can affect the peak position and the peak width [180]. Furthermore, the broadening of the $2D$ band also signifies a greater number of layers stacked on the wall. The broadening of the $2D$ band is more for the coated sample compared to the functionalized sample. Further analyses are carried out on the D, G and $2D$ signatures by considering approximations and the results obtained are discussed below in detail.

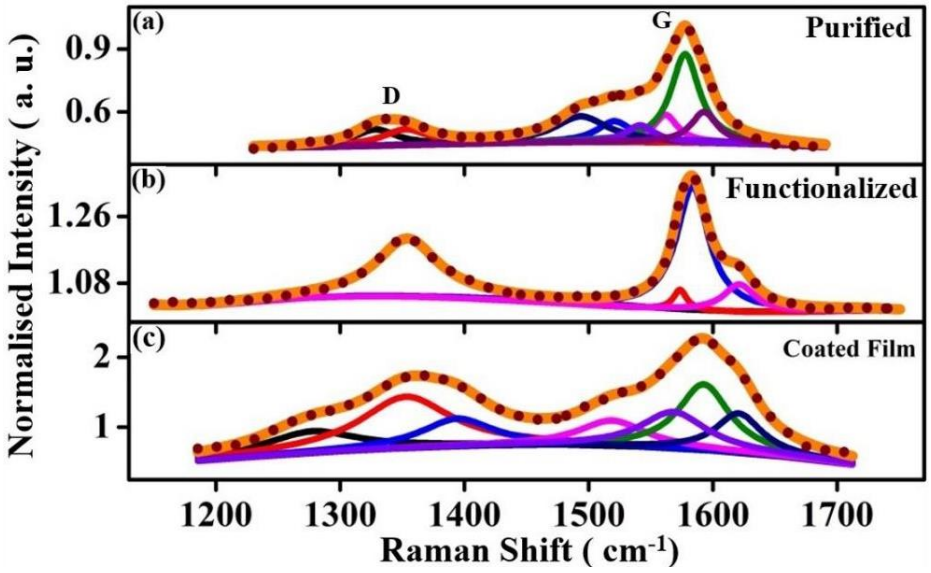

Figure 5.9: Peak fit of Raman D and G band of purified, functionalized and coated SWCNT film using Lorentz profiles. The intensity of the spectra is normalized w.r.t. the G peak of the purified data.

We have performed G band fitting by considering both the Lorentz profiles [Figure 5.9] which showed various defect components. Defect induced Raman D and G bands of purified, functionalized and coated film samples are shown in Figure 5.9. The bands are

approximated using Lorentz oscillators. Fitted D bands exhibit two (1328.45 and 1352.85 cm^{-1}), one (1354 cm^{-1}) and three (1277.35, 1352.83, 1394.55 cm^{-1}) components [Figure 5.9] respectively for the purified, functionalized, and coated film. G band which is the vibration of two unlike C atoms in the graphite unit cell is usually comprised of two peak features, a low-frequency G^- and a high-frequency G^+ arising from the confinement of phonon wave vector. While G^- corresponds to transverse optical (TO) phonon which is the vibration of C atoms along the nanotube circumferential direction, G^+ is associated with a longitudinal optical (LO) phonon signifying vibration along the nanotube axis [184]. The line shape of the G band is very significant where a narrow symmetric profile observed for each G mode corresponds to chiral semiconducting tubes and a broad softened G^- associated with a narrow G^+ is accounted for chiral metallic tubes. We find the signature of asymmetric G bands [Figure 5.9] which exhibit multiple contributions after fitting. Group theory anticipates six Raman active modes with two each of A (A_g^1), E1 [(E_g^1) and (E_g^2)] within A the tangential G band of SWCNTs [185].

In our data, six Lorentz oscillators peaking at 1493.81, 1520.79, 1541.96, 1561.88, 1577.67 and 1592.91 cm^{-1} respectively provide the best fit of the G feature for the purified sample [Figure 5.9]. Deconvoluted G spectrum of functionalized sample exhibits three Lorentz components at 1573.55, 1583.68, 1621.23 cm^{-1}, while the coated film shows the Lorentz profiles peaking at 1518.96, 1568.29, 1592.68, 1620.84 cm^{-1}. These Lorentz approximations yield COD values, 0.9961, 0.9969, and 0.9977 for the purified, functionalized and coated samples respectively which show the precision of our fit.

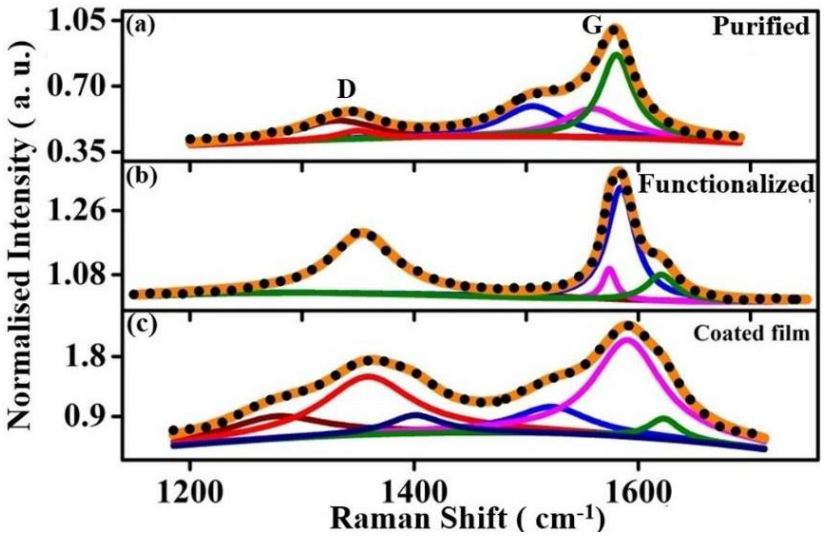

Figure 5.10: Peak fit of Raman D and G band of purified, functionalized and coated film using a combination of Lorentz and BWF line shapes. The intensity of the spectra is normalized w.r.t. the G peak of the purified data.

Our attempt to approximate G bands by considering the combination of Breit Wigner Fano (BWF) [Figure 5.10] and Lorentz line shapes have yielded a very low coupling strength parameter (phonon interaction with the continuum of states), $1/q \approx 0$ (< 0.007 for the coated film, while for purified and functionalized cases, $1/q$ is of the order of 10^{-6} and 10^{-7} respectively) which interpret that our investigations on the G band features do not reveal any signature of metallic CNTs in the samples, which may be an indication that the metallic tubes are not in resonance with the 2.33 eV laser excitation energy used for the Raman measurements herein.

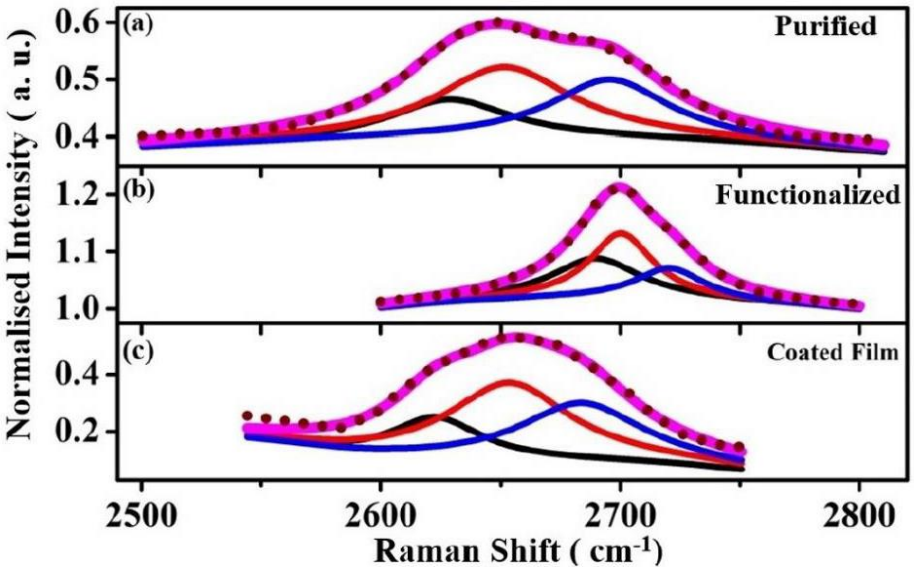

Figure 5.11: Lorentz approximated Raman $2D$ band of purified, functionalized and coated film. The intensity of the spectra is normalized w.r.t. the G peak of the purified data.

Figure 5.11 shows the $2D$ or G' bands clearly exhibit the presence of single-layer graphene-like structures in the nanotube ensembles (with the highest intensity), together with various double electron-phonon resonant processes. The emergence of $2D$ or G' band in the respective Raman spectra. $2D$, an overtone of D, is due to second-order processes of self-annihilating pair of phonons near the K-point of the zone boundary. This does not require the presence of any defect state to be activated. Each $2D$ band was well approximated by considering three Lorentz contours. The most intense $2D$ center peak is situated at 2651.3, 2700.3 and 2653.56 cm^{-1} for the purified, functionalized and coated film respectively [Figure 5.11]. These center peaks could be associated with single-layer graphene in sample 3. The low (2628.7, 2689.7, 2623 cm^{-1}) and the high (2695.76, 2720.55, 2683.9 cm^{-1}) frequency peak components on both sides of the main center peak could be assigned to double electron-phonon resonance activities in the samples giving rise to different resonant conditions for resonances with different VHS [139].

We have also analyzed the low-frequency range of the Raman spectra of functionalized and coated samples that reveal many peak onsets (up to 1000 cm^{-1}). It was reported that curved graphene sheets can show Raman signatures in the range of 200-1000 cm^{-1} [180,186,187]. For the functionalized sample, the low frequency range of 50-1000 cm^{-1} is analyzed. RBM-like features are observed at 214 and 270 cm^{-1} together with several onsets related to the CNS and MWCNT components [Figure 5.12 (a)].

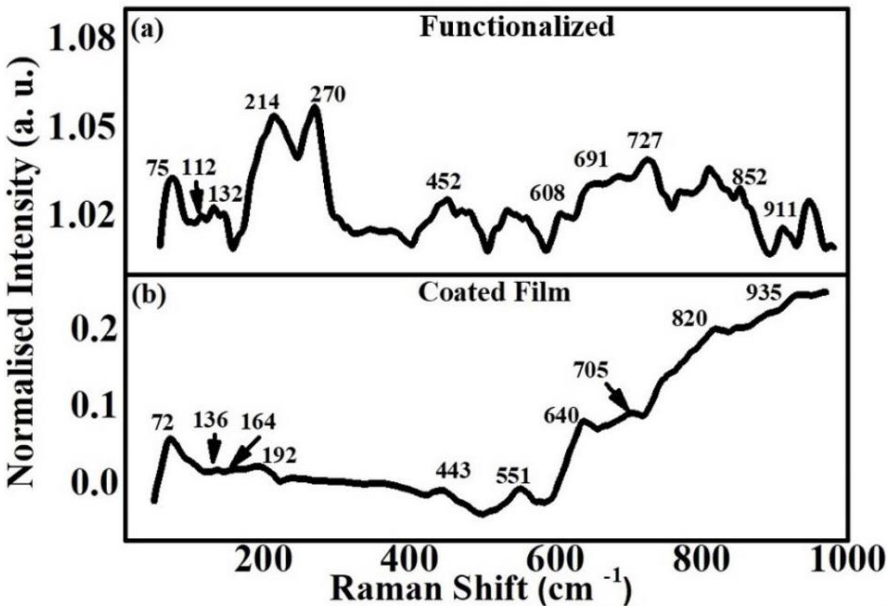

Figure 5.12: Low-frequency Raman spectra from (a) functionalized and (b) coated samples. The intensity of both spectra was normalized with respect to the G peak of the purified data.

The features located around 727, and 852 cm^{-1} can be associated with the curvature happening in the graphene sheets during the functionalization process [186], whereas the peaks appearing at around 452, 608, 691, and 911 cm^{-1} correspond to CNS [180] [Figure 5.12(a)]. The transverse optic and transverse acoustic phonon branches, which are usually inactive in the crystalline planar graphite, can become active due to the relaxation of the Raman selection rules owing to the curvature of the scrolls [180]. The Raman modes related to single and multiwall CNTs are also observed in the range 50-220 cm^{-1} [187,188]. For the MWCNTs, the origin of the low-frequency bands is due to the

breathing vibrations corresponding to individual walls, a phenomenon similar to that of the RBMs in SWCNTs. However, the vibration in MWCNTs is quite complex due to interaction among the individual concentric walls. We identify the characteristic onsets corresponding to MWCNTs at around 75, 112, and 132 cm^{-1}. The feature at 214 cm^{-1} could be associated either with the RBMs of the SWCNTs or to the MWCNTs in the functionalized sample [188]. The coated sample also exhibits almost a similar trend with the low frequency peaks appearing at 72, 136, 164 and 192 cm^{-1} signifying MWCNT components in the film [188], while the onsets at 443, 640, 705, and 935 cm^{-1} correspond to CNS [188]. We also observe several additional weak low frequency Raman onsets, which can be attributed to the curving of the graphitic sheets [180] [Figure 5.12(b)]. A diameter-dependent shift in the high-energy phonons can happen to the curved graphene layers and it is even possible to observe additional phonon modes corresponding to the extra symmetries induced in the curved structures [189].

5.3. Conclusion

In this chapter, we have conducted essential characterizations, including FTIR, XPS, XRD, and Raman, to gain insights into the chemical environment and vibrational modes of the as-prepared, purified, functionalized, and coated samples. The comparative study offers valuable distinctions in the chemical compositions, as well as disclosing emergence of various low-dimensional structural derivatives during the treatments.

CHAPTER 6

Emergence of structural derivatives of carbon from SWCNTs

In this chapter, we discuss emergence of various low dimensional structural derivatives of carbon from SWCNT bundles during oxidative purification, covalent functionalization and coating processes. The primary focus is to analyze and understand the TEM investigations that display diverse nano-structural components from the as-prepared SWCNTs. The most fascinating among all the structures observed is the signature of CNS and the beautiful manifestation of folding of GS into CNS. These results will be presented here.

6.1. Introduction

The novelty of the carbon nanomaterials lies in their structure dependent properties and the ability to tuning them during post-synthesis processes. Although CNTs have been extensively studied, many of the physico-chemical properties of the low dimensional carbon structures, as well as the stability of the SWCNTs and their bundles is still a matter of enormous research interest. Production of SWCNTs by synthetic methods give aggregates which are held together by vdWs forces of approximately 500 eV per micrometer of tube-tube [87] contact. These as-prepared bundles have a mixture of SWCNTs with different diameters and chiralities exhibiting widely varying properties [88]. Implementation of HiPCO SWCNTs into devices is often hindered due to presence of amorphous carbon contaminants and metal catalyst particles that need post-synthesis purification for further use. Exfoliation of the bundles and individual separation of the tubes by covalent functionalization or with surfactants in water are necessary before subjecting them to any applications. Therefore, a comprehensive understanding of the morphological and chemical modifications of the as-prepared CNTs after performing purification and functionalization is required.

In this chapter, structural evolution of as-prepared SWCNTs will be addressed. Disintegration of SWCNTs into other structural forms like MWCNTs, GS, junctions etc. are already reported. Here, we will highlight existing experimental and theoretical investigations to develop our understanding of the observed results behind exfoliation and unzipping of SWCNT networks and their structural alterations. Formation process of CNS from the SWCNTs is the main focus of this chapter by providing direct illustration of the TEM investigations.

6.2. Disintegration of SWCNTs

6.2.1. GS and MWCNTs

There are abundance of studies documenting the unzipping process of as-prepared SWCNTs due to post-synthesis treatments. Chemical and oxidative unzipping

[122,190,191], atomic H-induced cutting and unraveling [192], longitudinal unzipping of the CNTs using mixture of H_2SO_4 and $KMnO_4$ or KNO_3 [122], plasma etching [193], metal catalyst assisted cutting [194,195], lithium insertion and exfoliation [196,197] mechanical sonication in organic solvents [198], inter- or intra- tube intercalation of ions via tuning vdWs interactions [117,199–201] pressure induced radial collapse of the CNTs to GNRs [202] are the effective approaches reported to assist exfoliation of the CNT bundles. During oxidative acid purification or covalent functionalization, hydrogen ions in the acidic solution plays a crucial role in disintegrating the $C-C$ bonds and initiating the formation of different structural forms of carbon from SWCNTs [100,190]. Heat treatment of the SWCNTs [85,86] to manipulate their structures by minimizing strain energy is also a promising technique. During heat treatment, same chiral angle SWCNTs exhibit a gradual increase in diameter due to self-reconstruction [203] or diameter doubling [107]. It has been shown that almost 60% of the SWCNTs coalesce during annealing and form tubes of diameter twice or thrice of the original SWCNTs [107]. Tight binding and Monte Carlo calculations show coalescence of the SWCNTs under electron beam irradiation at high temperature in an electron microscope [203]. Emergence of MWCNTs is also reported [204] due to merging of SWCNTs around the central SWCNT or amalgamation of the bundle as a result of heat treatment [205]. Theoretical first-principles calculations demonstrate that oxidative longitudinal unzipping of SWCNTs takes place in the middle and at the ends for the armchair and zigzag tube configurations respectively via overcoming a diameter and chirality dependent energy barrier [206]. At the initial stage of $C-C$ bond tearing, the value of the energy barrier decreases with increasing tube diameter; however, the subsequent tearing of the $C-C$ bonds that are parallel to the ones broken initially is barrierless [206]. The unzipping process of SWCNTs is also examined using molecular dynamics (MD) simulations and tight-binding approach in the presence of atomic H [207]. The calculations reveal self-zipping of the partially unzipped SWCNTs which occurs at about $600K$ is hindered when dangling bonds of unzipped C atoms are saturated with H atoms [207].

CNTs in the presence of oxidizing agents unzip and form GS [208]. In this process, the mechanism of unzipping is based on the oxidation of alkenes by concentrated acid treatment [122]. Lopez et al. [205] proposed a thermally driven transition of SW to MW tubes by creating vacancies and defects at an elevated temperature. Structural amendment of SW to MW CNTs was explicitly demonstrated experimentally by annealing SWCNT bundles. These results were further substantiated by performing MD simulations [205]. The vacancies or defects created on the SWCNTs were cited to be primarily responsible for promoting the coalescence of two SWCNTs via inter-tube polymerization. This plays a prominent role in the transformation of SW to MW tubes. Acid purification and a slight increase in temperature can drastically alter the SWCNT structure [190]. The vacancies and defects during annealing acquire high mobility throughout the tubes and the migration of defects continues until they are trapped in the inter-tube regions by saturation of the dangling bonds at the vacancy sites, which initiates polymerization in the neighboring tubes due to interactions among the trapped defects [205]. The coalescence of two tubes occurs via further pulling apart of the intra- and inter- tube bonds followed by patching and tearing of all the SWCNTs in the bundle, giving rise to MWCNTs [205]. Functionalization will further enhance the tearing process of the CNTs due to the use of a mixture of concentrated H_2SO_4 and HNO_3 acids and subsequent magnetic stirring, which will produce more defects and increase the temperature of the samples [209], [210]. This will result in the formation of GS and MWCNTs. HNO_3 can also intercalate in the SWCNT bundles and dismantle the tube walls to give rise to graphitic sheets, which can eventually change to form various multi-shell phases [211].

6.2.2. CNS

CNS with their recent scientific visibility and research interest have become an important topic of investigation. These jelly roll-like structures owing to their unique scroll topology, unfused ends and open extremities can exhibit far superior properties compared to other carbon 1D counterparts of SW or MW CNTs. With tunable core sizes, CNS can be the perfect candidates for applications related to tunable water and ion channels,

molecular sensors, flexible gene and drug delivery systems [212]. Varying interlayer spacing of CNS can host different intercalated species that can have potential applications starting from hydrogen and energy storage in supercapacitors and batteries [213,214], [215]. Optical properties of these 1D carbon materials [216,217] reveal promising features to be used as black absorber coatings [28]. To date, a variety of routes have been employed to fabricate CNS from graphene sheets such as mechanical methods and chemical synthesis. The molecular dynamics simulations performed by Braga et al. showed that CNS can have a lower energy than graphene layers [218]. The production of high yield CNS was first reported more than a decade ago by intercalating graphite with potassium followed by exfoliation in a highly exothermal reaction environment. Exfoliated graphene layers were then deformed by sonication to give rise to CNS [219,220]. Since then, many other methods have been proposed for the bulk production of CNS, e.g., microwave irradiation [24,221] using CNTs [24], inducing solution-based scrolling of graphene sheets on a silicon dioxide (SiO_2) substrate [220], and solvent-assisted self-assembly of graphene oxide (GO) layers [222]. The formation of CNS is an energy aided process due to the structural transition of the graphene layer, where a large overlap between two edges of freestanding graphene occurs, leading to the relative sliding of the overlapped region after a critical overlapped area is attained. The self-sustained scrolling process continues as the vdWs interactions between the layers provide structural stability to form CNS [218]. Also, the low bending rigidity of graphene, which is determined by the bending-induced changes in the interactions between electron orbitals [223], plays an important role in the structural modification of graphene nanoribbons and the eventual formation of CNS. For monolayer graphene, the out-of-plane deformation associated with stretching and compression of covalent $C-C$ bonds is responsible for the bending rigidity [224,225], while for multilayer graphene, this depends on the number of layers and the interlayer shear interaction [226]. The bending stiffness typically follows a thickness-dependent square power relation for the self-folding mechanism of few-layer graphene (2-6 layers) with an interlayer shear modulus value in the range of 0.36-0.49 GPa [226]. The atomistic simulations performed by

Nikiforov et al. [227] showed that large diameter SWCNTs very closely represent the behavior of graphene under pure bending in the low-curvature linear elastic regime. The simulations revealed curvature-induced torsional misalignment of the *p* hybrid orbitals as the key source of bending stiffness with a value of 1.49 eV [228]. Although theoretical studies provide a wide range of values of bending rigidity for single-layer graphene [228], [229], the experimental value is cited to be 1.2 eV for a graphene sheet [230]. Fabrication of CNS out of GS via mechanical and chemical routes were reported earlier. Production of CNS with high yield was first reported by intercalating graphite with potassium in a highly exothermal reaction and deforming the exfoliated graphene layers by sonication [24,222]. Since then, various methods have been proposed for bulk production of CNS [222–225]. According to MD simulation results, CNS have a lower energy than the graphene layers [221]. The scrolling mechanism of CNS is a self-sustaining process determined mainly by the low bending rigidity [226–235] of graphene and the vdWs interactions between the layers that provide structural stability [221]. In our TEM studies, we find direct manifestation of tearing of the SWCNT bundles, evidence of GS in the treated sample and winding of GS into CNS. This was achieved by subjecting the as-prepared SWCNTs to the oxidative acid purification and covalent functionalization process. Investigation of the TEM results, impact of chemical processing on the initial tubes and their structural changes will be discussed in this chapter.

6.3. Electron microscopy investigation results

Comprehensive information about sequential structural disintegration of the as-prepared SWCNT bundles was revealed by TEM studies. We see direct evidence of low dimensional structural forms in the sample after purification, functionalization and polymer grafting process. An artificial color code is given to the images using ImageJ / Gwyddion softwares during analysis of the TEM data for better visualization.

6.3.1. As-prepared

TEM investigations carried out on the as-prepared sample reveal sparse bundle network of SWCNTs [Figure 6.1]. Large area scans of the sample prior to purification exhibit a cloth like network of SWCNT aggregates [Figure 6.1(a)] with traces of carbonaceous [marked by arrows in Figure 6.1(a)] and metal catalyst particles [Figure 6.1].

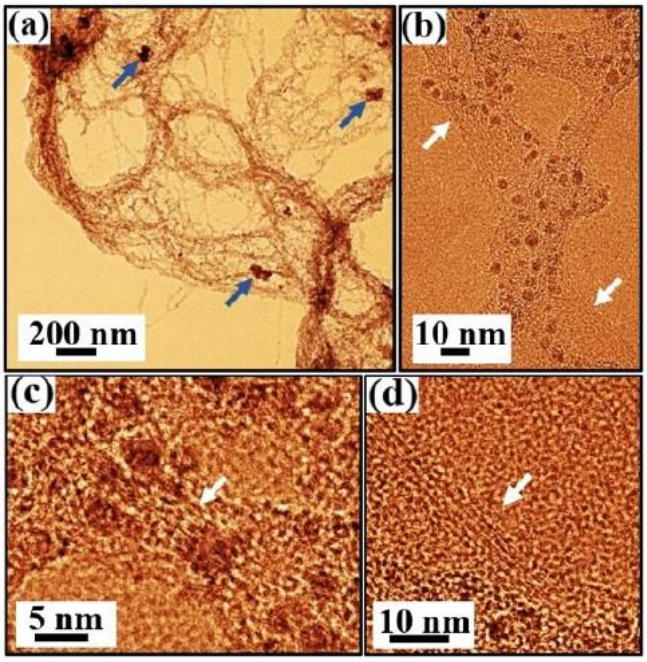

Figure 6.1: TEM micrographs obtained from the as-prepared SWCNT sample. (a) Shows the large area image with bundled networks of SWCNTs. Amorphous carbonaceous particles are marked in (a) using arrows. (b) (c) and (d) show clear evidence of SWCNTs (marked with white arrows) within the bundled network. Presence of metal nanoparticles are observed as dark spots in (b-d).

The metal impurities appear as dark spots in the micrographs [Figure 6.1(b-d)]. The SWCNT bundles are shown by white arrows in Figure 6.1(b-d). We do not find any evidence of GS, MWCNTs, CNS or other structures in the TEM studies of the pristine sample.

6.3.2. Purified

TEM investigations of the purified sample are shown in Figure 6.2, 6.3 and 6.4. Purified data reveals SWCNT networks with a substantial decrease in the catalyst and carbonaceous contaminants [Figure 6.2]. However, small traces of contaminant particles are still visible as dark spots shown by black arrows in Figure 6.2(a). Within the network, the different SWCNT bundles exhibit different diameter periodicities ranging from 0.7-1.1 nm [Figure 6.2(a, b)].

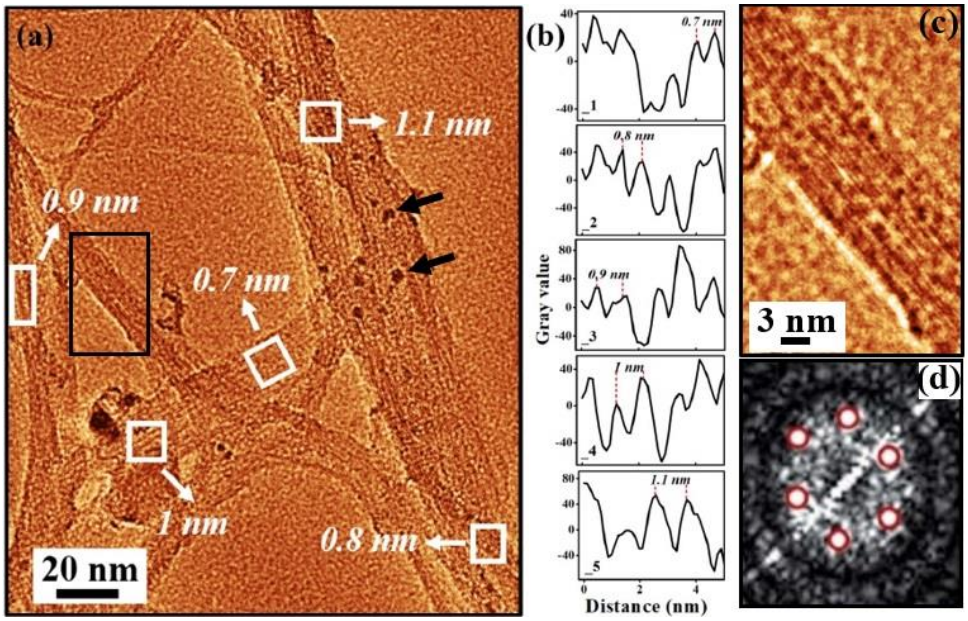

Figure 6.2: (a) TEM image showing SWCNT strands of varying diameters in purified sample. The regions of different diameter periodicities are marked using white rectangles on the image. (b) Shows the line profiles taken across each such rectangular region. Diameter periodicity of the SWCNT bundles within the rectangles is marked in the profiles. (c) Evidence of SWCNTs in the bundles and (d) FFT of the SWCNT bundle shows the hexagonal symmetry of the sp^2 hybridized carbon atoms.

The line profile taken across a bundle is averaged w.r.t. the number of nanotubes (represented by peaks in the profiles) to obtain an average diameter. Figure 6.2(c) is obtained from Figure 6.2(a) [area marked by black rectangle]. It clearly displays a SWCNT array that has a diameter periodicity of 0.9 nm [Figure 6.2(c)]. The FFT obtained from this array [Figure 6.2(d)] shows the hexagonal symmetry of the sp^2 hybridized

carbon atoms. Structural heterogeneity in the purified sample is also evident with signature of MWCNTs, GS and CNS [Figure 6.3, 6.5]. Evidence of MWCNTs in the SWCNT network is marked in Figure 6.3 by rectangles. Figure 6.3(b) depicts one of such MWCNT networks taken from the rectangular area of Figure 6.3(a). The MWCNTs typically exhibit diameters in the range of 10-30 nm [marked in Figure 6.3(c)]. The high-resolution TEM micrograph [Figure 6.3(d)] obtained from such a MWCNT clearly exhibits graphitic (002) layer stacking with a spacing of 0.34±0.02 nm.

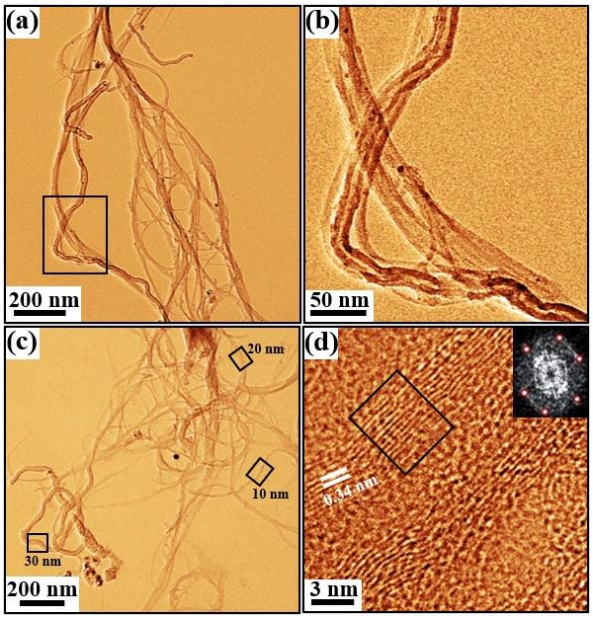

Figure 6.3: TEM investigations of the purified sample. (a) Large-scale image showing sparse bundle network of SW and MW CNTs with rare presence of impurity particles. (b) MWCNTs from the marked area in (a). (c) Presence of MWCNTs with varying diameters (marked within black squares). (d) High-resolution TEM image of an MWCNT with graphitic (002) plane stacking. The (002) layer spacing of ~0.34 nm is marked in (d). Inset of (d) is the FFT from the selected area [marked as a rectangle in the image].

The FFT taken from the marked area in Figure 6.3(d) is shown as an inset. It again reveals the hexagonal symmetry of the graphitic layers within the MWCNT structure. Catalyst particle induced tearing of the SWCNT bundles in the TEM micrographs are also noticed [Figure 6.4(a, b)]. Curling of SWCNTs and forming ring like structures are seen in Figure

6.4(c) and (d) [marked by arrows]. Manifestation of ring like structural configurations by branch of tubes exfoliated from the SWCNT bundles are seen in Figure 6.4(c, d).

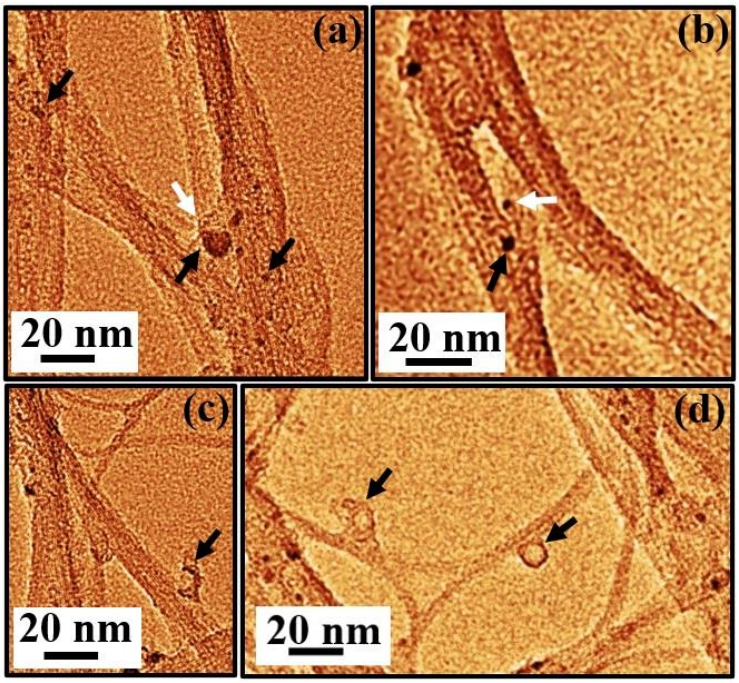

Figure 6.4: TEM investigations of the purified sample. Gross reduction in catalytic metal nanoparticles after a systematic purification process is observed. (a) and (b) Catalytic tearing induced by metal nanoparticles in the SWCNT bundles shown by white arrows; (c) curling of SWCNTs; and (d) evidence of ring formation.

This is an indication of O_2 driven exfoliation of SWCNTs leading to formation of ring structures [236–238]. Chen et al. [238] discussed the possibilities of deformation and coiling of carbon nanorings (CNRs) from SWCNTs due to vdWs interaction. According to Chen et al., least energy and maximum occupancy of the CNRs are achieved for spiral configuration during insertion or wrapping processes [238]. This kind of self-assembly of CNRs and SWCNTs [Figure 6.4(c) and (d)] can have high potential applications in carbon based nanodevices [238]. TEM investigations of purified data further reveal evidence of GS and formation of CNS in the sample [Figure 6.5(a, b)]. Illustration of curling and folding of GS into CNS can be observed in Figure 6.5(a-c).

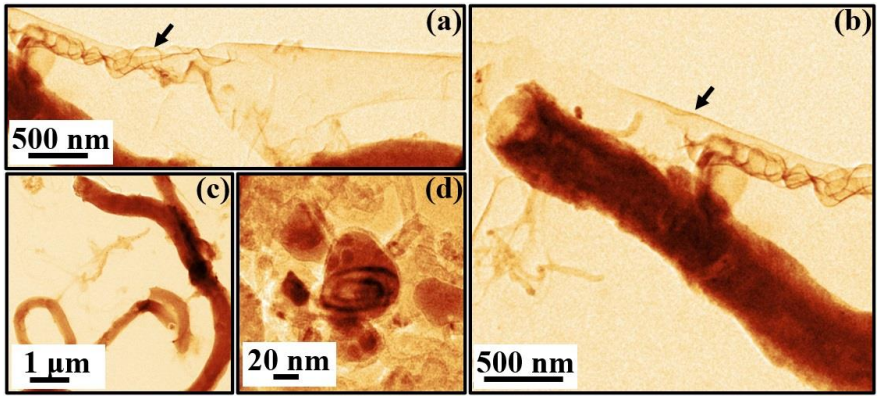

Figure 6.5: (a)-(c) TEM micrographs depicting formation of CNS from GS. (d) Cross-sectional view of CNS revealing rolling of GS inside.

Figure 6.5(d) shows the cross-sectional view of a CNS where rolling of GS to CNS is well evident. CNS are morphologically similar to MWCNTs; however, the distinction remains in their open extremities, varied layer spacing, and sides, where the edges of the scrolled sheets are not fused. These 1D structures usually exhibit large diameters, typically around 100-500 nm with open ends as observed in Figure 6.5(c-d). Signature of longitudinal tearing of CNS along the axis, induced by either catalyst particles [Figure 6.6(a, b)] or due to stress and strain [Figure 6.6(c)] are also observed in the TEM studies.

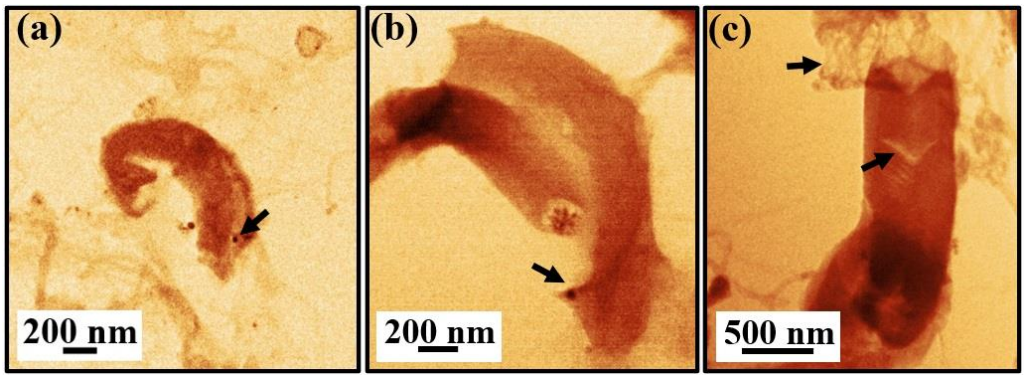

Figure 6.6: (a and b) Catalyst metal nanoparticle induced axial tearing of CNS. (c) Stress and strain induced tearing of CNS.

The tearing of CNS will generate GS in the system. Indication of merging of SWCNT bundles via diameter enlargement is captured in Figure 6.7. Figure 6.7(a) shows many entangled SWCNT bundles with signature of infused catalyst nanoparticles at their ends. Zoomed images of the end points of such entangled SWCNTs are shown in Figure 6.7(b, c). The ends are mostly capped with catalyst particles that are surrounded by shell like structures [Figure 6.7(b, c)]. However, uncapped hollow ends are also evident [Figure 6.7(a, b)], without any trace of catalyst particles. The end of the tube bundles is having circular [Figure 6.7(a, b)] or faceted peripheries [Figure 6.7(b)].

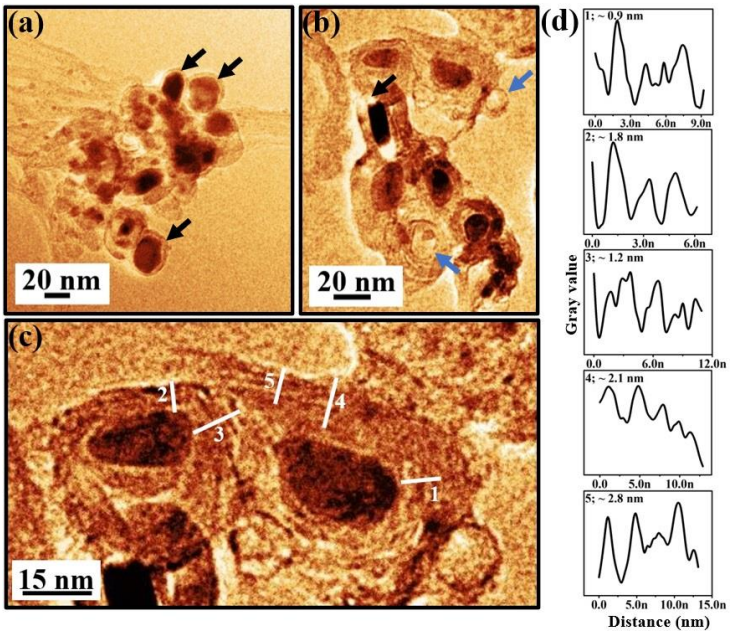

Figure 6.7: (a)-(c) TEM images of merging of SWCNT bundles. (d) Periodicities of the merged SWCNTs.

The shells are formed by many concentric graphitic layers exhibiting distinct fringes [Figure 6.7(b, c)] with periodicities in the range between 0.9-2.8 nm [Figure 6.7(d)]. The inner diameter of the shells is around 15-20 nm, whereas the outer diameter lies in the range between 25-30 nm with typical width of the shells around 10-15 nm. Signature of radial merging of the outer fringes of the nearby shell-like structures is evident in Figure 6.7(b, c). Such merging process signals direct amalgamation process occurring via

tearing and subsequent coalescence of the SWCNTs in the bundles causing an increase in the inner diameter observed as 15-20 nm which is, otherwise, reported to be 0.7-1.3 nm [88] for individual tubes in the purified sample.

6.3.3. Functionalized

TEM micrographs of the functionalized sample again disclose a multi-component material with evidence of various low dimensional carbon features [Figure 6.8, 6.9]. The network of entangled and branched bundles of SWCNTs [Figure 6.8(a)] is still evident, however, further structural alterations and emergence of heterogeneous components are seen due to sulfo-nitric treatment using strong H_2SO_4 and HNO_3.

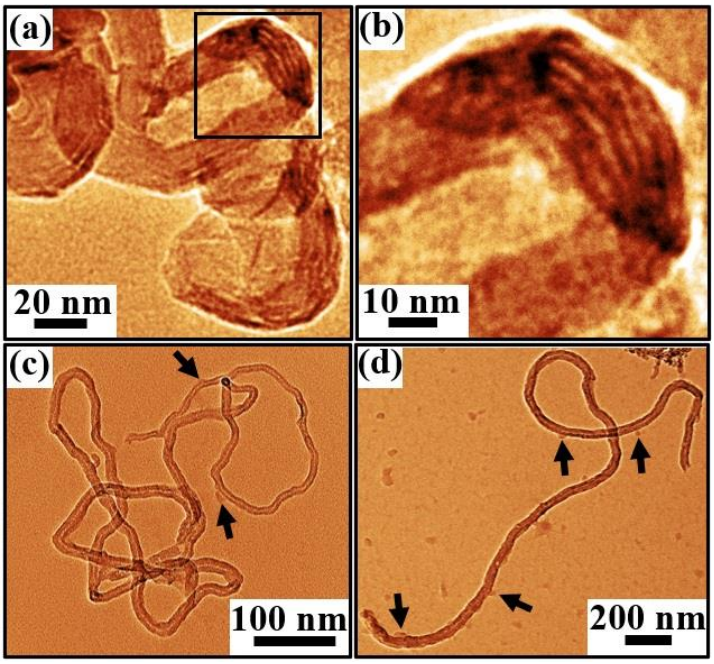

Figure 6.8: The presence of SWCNT bundles (a, b) and MWCNTs (c, d) in the functionalized data. Twisted SWCNT bundles can be seen in (a). SWCNTs with enlarged diameter (b). Attachment of functional groups is visible as protrusions on the walls of the nanotubes [marked by arrows, (c), (d)].

Figure 6.8(a, b) show the SWCNT network, while Figure 6.8(c, d) exhibit the MWCNTs in the functionalized data. Signature of significant amount of functional groups attached

to the side walls are evident in the TEM micrographs [Figure 6.8(c, d); marked by arrows]. Twisted SWCNT bundles with enlarged diameter are seen in Figure 6.8(c, d). This is attributed to the incorporation and intercalation of functional groups into the CNTs. Functionalized sample exhibits SWCNTs with diameter in the range between 1-3 nm, while for the MWCNTs it is around 30-80 nm. Figure 6.9 reveals multicomponent low dimensional structural forms in the functionalized data.

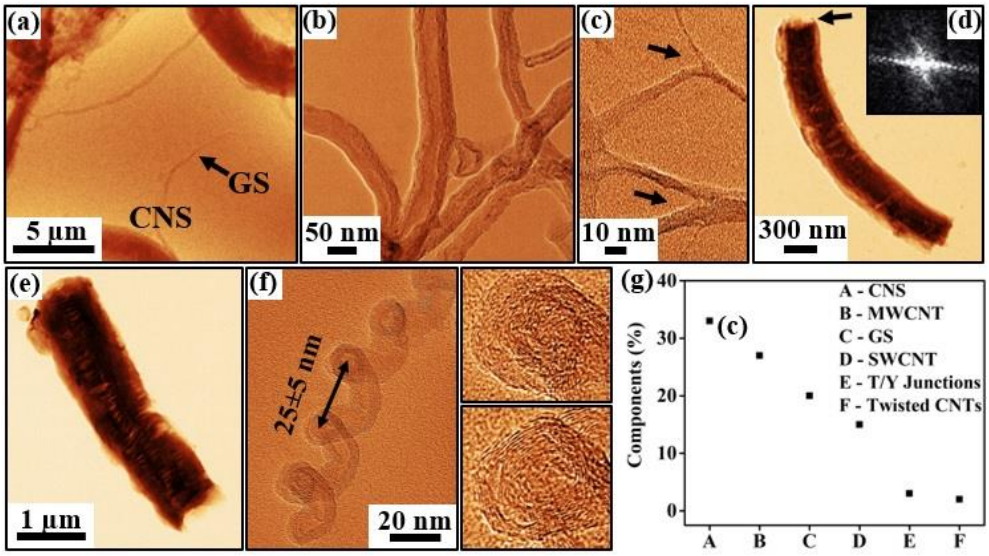

Figure 6.9: TEM micrographs of the functionalized sample. (a) Evidence of GS and CNS. (b) MWCNTs with amorphous side walls. (c) Longitudinal exfoliation of SWCNT bundles and formation of `Y' like junctions. (d, e) Nanoscrolls which are short after conducting the functionalization process and with open-ends [marked with arrow]. Inset in (d) is the FFT of the CNS revealing amorphous crystallinity. (f) Twisted MWCNT with a periodicity 25±5 nm. Right panel of (f) shows 'CNO' like nodes of the twisted structures with a graphitic (002) layer spacing. (g) Statistical weightage of different structural components presents in the sample.

CNS and GS are seen in Figure 6.9(a). Figure 6.9(b) shows MWCNTs with amorphous graphitic walls. Signature of `Y' like junctions in the sample is also evident [Figure 6.9(c)]. Figure. 6.9(d, e) show CNS in the sample which are short compared to the purified data due to concentrated acid treatment. FFT [inset, Figure 6.9(d)] acquired from the CNS shown in Figure 6.9(d) reveals amorphous nature. We also notice signature of spiral like twisted CNTs [Figure 6.9(e)] after the sulfo-nitric process. It is documented

that the HNO_3 treatment of SWCNTs usually generate multi-shell phases of carbon like MWCNTs, carbon nano onions (CNOs) etc. [239]. Twisted structures of collapsed SWCNTs or MWCNTs try to minimize their free energy in the deformed state or accord a local minimum with a large barrier to sustain the collapsed state [225,240]. Coils of MWCNTs, suspended or supported on the surfaces, are due to the competition between interlayer attractive force and curvature elasticity, while atomic lattice registry dependent intertube interactions between SWCNTs of different helicity generate the twisted SWCNT ropes [225,241–245]. The periodicity of the twisted nodes seen in our case is around 25 ± 5 nm [Figure 6.9(f)]. These structural forms induced by curvature elasticity after the functionalization process can be very useful to achieve large scale deformation of nanoscale specimens and for biopolymer applications. These twisted structures can be used as actuators, lithium ion batteries etc. [246,247]. Right panel of [Figure 6.9(f)] shows the resolved fringes within the nodes of collapsed MWCNTs. High resolution TEM micrographs of these nodes look "CNO like" structures with graphitic (002) layer stacking (spacing between the layers: 0.34 ± 0.02 nm) [248].

CNOs are member of fullerene family comprised of quasi spherical or polyhedral shaped graphitic layers with a hollow core [248]. Structural simplicity, as well as, chemical reactivity of CNO like structures are very useful for applications in heterogeneous catalysis [249], electro-optical devices [250], energy storage etc. [251]. The cylindrical or spherical morphology of these particles at the nanometer scale can demonstrate interesting tribological properties mostly due to their shape and chemical inertness without dangling bonds. As a result, CNO like structures are used as additives and can lead to a strong reduction of both friction and wear even at low temperature. These particles are also considered promising candidates as solid lubricants for incorporation in fuels by NASA for aerospace applications [242] owing to their lubricating property. Onion like structures along the tube can also be induced due to presence of a minuscule quantity of $-CH_x$ functional groups on the side walls of the CNTs.

The step wise acid treatment carried out in this study using concentrated HCl and a mixture of strong H_2S0_4 and HNO_3 are supplemented by damage to the nanotube

framework by creating intrinsic defects and holes that are functionalized with oxygenated functional groups like carboxylic, hydroxyl, ketone, alcohol, ester, sulfate, nitrate etc. Overall, this atomic alteration and chemical modification tend to open up the tubes which eventually give rise to distinct structures. It is known that sulfate with a moderate solvated size and polarizability also helps in exfoliation [199].

Statistically, the percentage of structural diversity in the sample was calculated by considering around 150 TEM micrographs. We find that the main components in the functionalized sample are CNS, MWCNTS, GS, and SWCNTs contributing more than 95%. Other structural forms like junctions, CNT coils etc. are less than 5% in the sample. This is shown in Figure 6.9(g).

6.3.4. Coated Film

The TEM investigations of the coated sample are shown in Figure 6.10. We observe SWCNT arrays [Figure 6.10(a)]. Presence of MWCNTs with the walls made of many graphitic layers spaced approximately 0.34 ± 0.02 nm apart is shown in Figure 6.10(b, c). Figure 6.10(d) clearly exhibit the polymer grafted CNTs with a polymer thickness of 5-20 nm.

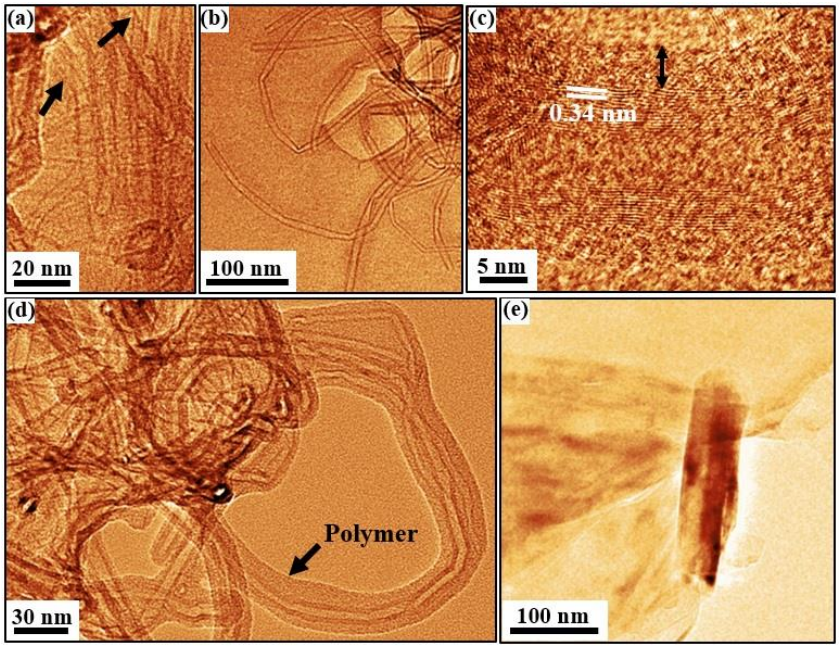

Figure 6.10: TEM investigations on the coated film. (a) SWCNTs (marked with arrows). (b) Graphitic plane stacking in the MWCNTs present in the sample. (c) Large-area image showing the entwined MWCNT structures. (d) Formation of CNS from the carbon sheets.

Coated sample also manifests scrolling of carbon sheets and formation of CNS [Figure 6.10(e)].

6.4. Discussion

A pictorial depiction of the sequential merging process of SWCNT bundles is shown in Figure 6.11. Figure 6.11(a) displays the cross-sectional view of a SWCNT bundle with 19 individual SWCNTs which start disintegrating slowly during the purification process following various intermediate steps [Figure 6.11(b-e)] to form concentric SWCNTs [Figure 6.11(f)] with enlarged diameter.

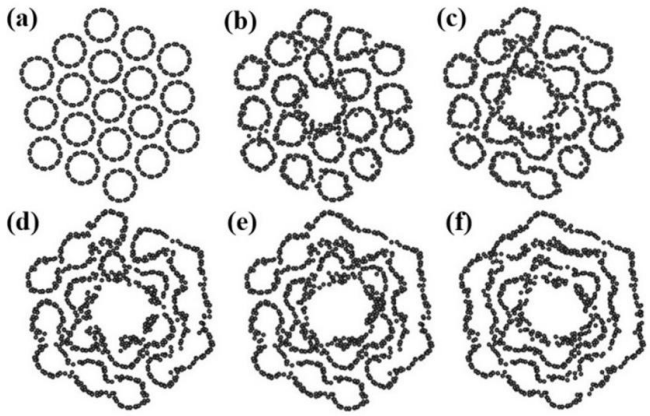

Figure 6.11: Pictorial cross-sectional depiction of merging process of the SWCNT bundles during purification process.

It has been reported that the presence of defects in the tubes mainly vacancies, act as a dominating force to drive the coalescence process [252] of the CNTs. Vacancies can be created by various routes like high temperature annealing of the CNTs above 1600℃ [253], irradiation by electron beam [254], chemical treatment [107] and so on. A two-step purification process involving HCl treatment followed by air-oxidation at 500℃ for 30 min was reported to convert the SWCNTs to double wall nanotubes (DWCNTs) with high yield (95%) [204]. The entangled CNTs in the acidic medium aggregate themselves during annealing owing to vdWs interactions that result in enhancing the diameter [190]. According to K. H. An et al. the HCl treated SWCNT samples showed a diameter distribution in the range 10-25 nm matching well with the observed distribution of inner diameter of 15-20 nm of the merged tubes in our case as indicated above. Here, the samples were wet oxidized at 300℃ followed by HCl washing and were then annealed at 900℃ for one hour. As a result, coalescence of the tubes is very likely and their unzipping will produce GNR and GS [115, 120, 121, 188–194, 195–198, 200, 254] which will eventually initiate the scrolling. Binding of oxygen atoms to the surface and formation of two-legged epoxy bridges across the carbon atoms is also likely which in due course would line up to lower their energy and exerts a collective tension to tear the $C-C$ bonds [236,255]. Ultimate structural relaxation would occur via forming GNR and GS which

eventually scroll up to give CNS. In the similar way, the mechanism of tearing of SWCNTs via attachment of oxygen containing functionalities at the defective sites leading to final transformation into CNS is demonstrated in Figure 6.12(a-e).

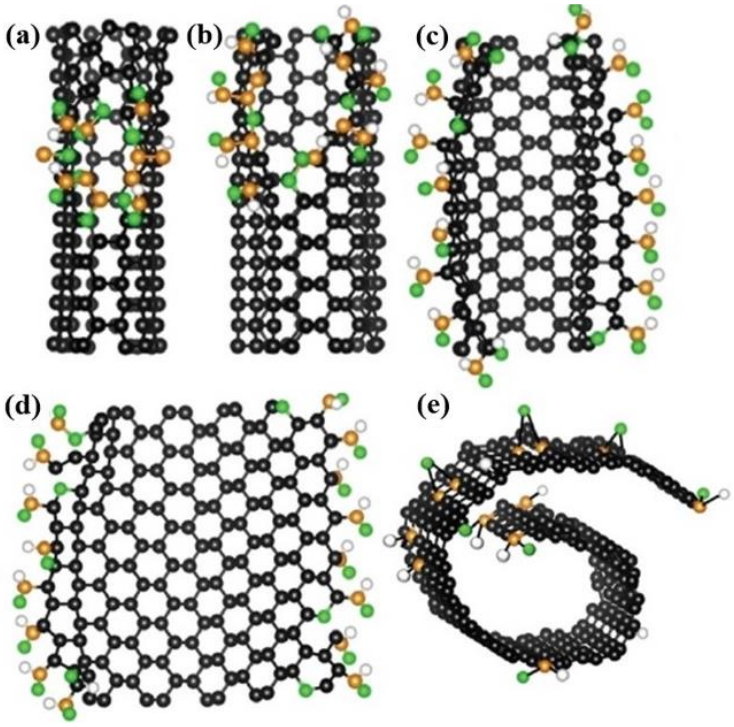

Figure 6.12: Stepwise axial unzipping of CNTs leading to formation of opened GS and rolled CNS structures.

In Figure 6.12(a-e), the defect and chemical group induced axial unzipping process of SWCNTs into GS and further rolling of GS to CNS are shown schematically. Scrolling and unscrolling processes of the GS are largely dependent on the chemical properties of the surface [35,256,257]. Interaction of graphene with itself or nearby GS or with other materials during folding is a complex event with surface forces being the governing parameters. For the graphene layers with the vdWs interaction being the main surface force of attraction, adhesion energies of ca. $0.45\ Jm^{-2}$ and $0.31\ Jm^{-2}$ have been reported for single and 2-5 layers respectively that lies within the limit of solid-liquid interaction. This value of high adhesion energy is mostly responsible for GS to give various other

surface morphologies [258]. Formation of CNS is governed by the elastic energy due to bending of GS and decrease of free energy in the overlapped regions of the layer originated by vdWs interaction [219]. During folding, the overlapped areas of a graphene layer interact and adhere and the deformation of the lattice occurs at the bend site giving rise to lattice strain [35]. The low bending rigidity of graphene that is governed by the bending-induced changes in the interactions between electron orbitals [28,259] plays a vital role in structural modifications of graphene sheets and formation of CNS. Also, the lattice strain generated at the bend site works itself as a restoring force to get the layer back to planar configuration [35]. With the attractive forces in the overlapped areas being greater than the restoring force at the bend site, the GS continues to bend and the vdWs force provide the stability of the scrolled configuration. Critical dependence of rolling on the surface energy could be modified by introducing foreign atoms and molecules on the surface. However, the presence of surfactants or functional groups in a liquid medium which get attached to the graphene surface would render surface charge making the folding mechanism more complex [252]. A possibility to overcome the issue of surface charge is to adjust the pH of the solution. The number of functional groups attached would vary depending on the techniques used and their random distribution on the defect sites of the lattice resulting different layer–layer and layer–solvent interactions. At low pH, the folding or scrolling takes place due to functionalized areas of the graphene layer interacting with the other areas of the same or different sheets in the medium, whereas, at a pH above neutral, the negative charges on the oxygen containing functional groups on the surface repel each other that causes deformation of the sheet to a curved surface from its planar configuration [254]. In a medium with very high pH, there will be a large number of oxygen groups attached to the surface that will have many center points to start the radial curvature process resulting in multiple bends and folds in the system giving rise to a nonuniform folded morphology. Additional architectural change can also occur due to surface tension effects during drying up of the solvent [254]. Research on covalent, non-covalent functionalization of graphene and chemical modifications of the graphene surface for various applications have received huge research interest in the last

several years. Formation of strong covalent bonds that occurs between the functional groups and the CNTs during covalent functionalization makes it superior to the noncovalent functionalization process. Scrolling can be induced by reliable functionalization of graphene or graphene oxide (GO) sheets with various oxygen containing functional groups like carboxyl, hydroxyl, carbonyl, epoxide etc. that provide active sites to trap, stabilize and nucleate metal ions [260]. This technique seems to be very promising to prepare CNS. Zu et al., have shown that partially hydrogenated graphene on one side of the sheet can form stable CNS at RT [261]. Chemical modification of GO and its covalent functionalization at the basal plane and edges is reported to be effective in making the sheets scroll to form CNS [69,262,263]. Graphene scrolls prepared by liquid nitrogen quenching, adding sodium citrate in GO aqueous suspension demonstrated high electrochemical properties which are dependent on the amount of added sodium citrate and the individual scroll morphology. Sodium citrate with abundant functional groups and short carbon chains modifies the surface properties of the GS to make scrolls of controllable geometry and size that emerge as supercapacitors [264]. In this study, the presence of alkoxy ($C-O$), carboxylic ($-C-O$), hydroxyl ($-OH$), carbonyl ($C=O$) and epoxy ($-C-O-C-$) functional groups that are clearly evident in the XPS and FTIR studies (discussed in the previous chapter) of the samples will modify the surface properties of the GS that emerged during the chemical oxidation process of the CNTs. It has been reported that functional groups can be used as surfactants to assist the synthesis of graphene scroll composites via changing the surface properties of the GS [264,265]. We attribute the formation of CNS from the SWCNTs as oxidative functional group induced folding and scrolling of the GS.

6.5. Conclusion

Research on CNS is presently an emerging field where attention is mainly focussed on their synthesis, fabrication and looking for new properties for industrial applications. In this chapter, we have discussed the TEM results of disintegration of as-prepared HiPCO SWCNTs to other low dimensional structural derivatives of carbon such as MWCNTs,

GS, CNS, twisted CNTs etc. after performing purification and functionalization process. Manifestation of CNS from the SWCNT networks via a simple oxidative route is addressed in detail for the first time. The purified sample exhibits evidence of GS and direct illustration of curling and folding of GS into CNS. Signature of radial merging, catalyst particle induced axial tearing of the SWCNTs, chemical cutting as well as stress, strain induced tearing of CNS and their unraveling to GS are also clearly observed in the TEM investigations. The GS, thus, formed may again contribute to forming the CNS due to presence of the functional groups in the treated sample. Strong acid treatment during covalent functionalization process further helps in exfoliating, unzipping and cutting down the structures, and also give new structures like twisted CNTs and CNOs in the sample. These results are addressed here. Such fabrication of CNS from SWCNTs is hitherto unreported.

CHAPTER 7

Morphology study of CNT based black absorber thin films

This chapter conducts a thorough examination of coated samples utilizing SEM and TEM characterization tools. It specifically emphasizes the notable absorption features observed in thin film coatings derived from black absorber CNTs. The study employs UV-Vis-NIR characterizations, and the verification of absorption features is conducted after subjecting the coatings to space simulation tests. The results highlight the extended duration and stability of these coatings under extreme space conditions.

7.1. Introduction

The morphology study of CNT-based black coatings using SEM and AFM provides valuable insights into the structural characteristics and surface topography of the coatings. SEM offers a high-resolution, three-dimensional view of the coating's surface, allowing for the observation of CNT distribution, orientation, and overall morphology. AFM, on the other hand, provides nanoscale surface profiling, offering detailed information about surface roughness and CNT arrangement. By employing these advanced microscopy techniques, we can comprehensively analyze the nanostructure of CNT-based black coatings. This combined approach aids in understanding the coating's surface features, which is essential for optimizing its performance in terms of adhesion, durability, and functionality. On the other hand, to investigate the high absorption features of black absorber CNT coatings using UV-Vis-NIR spectroscopy is a crucial aspect of understanding their optical properties. UV-Vis-NIR spectroscopy enables the comprehensive examination of the coatings' absorption capabilities across a wide range of wavelengths. This study provides valuable insights into the efficiency of CNT coatings in absorbing light, especially in the UV, Vis, and NIR regions. Such knowledge is essential for optimizing these coatings for stray light control applications, where tailored absorption features can significantly enhance performance.

7.2. Microstructure and elemental analysis

SEM and AFM studies are used for microstructural analysis of the samples. SEM micrographs obtained are shown in Figures 7.1. Figure 7.1 (a-c), (d-f), and (g-i) show the morphology of the purified, functionalized, and spray-coated samples respectively.

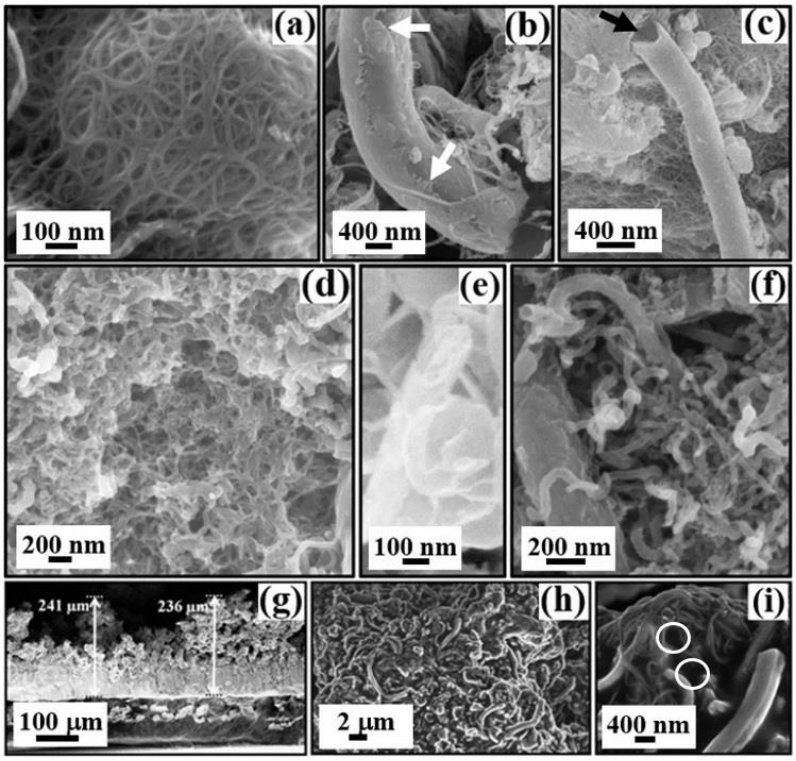

Figure 7.1: SEM micrographs of purified (a-c), functionalized (d-f) and coated (g-i) samples. The unfused edges and open ends of the CNS are marked by arrows in (b) and (c) respectively. A cross-sectional view of the coated film on the Al substrate is shown in (g) with the thickness marked. The cavities formed on the coated film are shown by circles in (i).

Direct evidence of nesting of the CNTs with agglomeration [Figure 7.1(a)], the signature of CNS with unfused [Figure 7.1(b)] and open [Figure 7.1(c)] ends (marked by arrows) can be seen in the purified sample. Nesting and agglomeration are due to σ and π bonds of the carbon atoms with σ bonds forming the strong hexagonal carbon network within the rolled graphene sheets, whereas, π bonds, perpendicular to the surface of the tubes, try to connect the CNTs by weak vdWs interactions [1,21,266–268]. SEM investigations after functionalization [Figure 7.1(d-f)] display evenly dispersed CNTs [Figure 7.1(d)], a direct manifestation of curling and folding of the carbon sheets to form CNS [Figure 7.1(e)] and coexistence of CNTs and CNS [Figure 7.1(f)]. An overall uniform distribution of CNTs after functionalization [Figure 7.1(d)] is attributed to the attachment of

carboxylic functional groups on the surface [181,182], which improves the dispersion and adhesion properties of the tubes [269].

SEM micrographs obtained from the coated films are shown in Figure 7.1(g-i). Cross-sectional view [Figure 7.1(g)] reveals the thickness of the film which is approximately 200-250 μm. SEM images also disclose the presence of interlinked forests [Figure 7.1(h, i)] with cavities or pores [Figure 7.1(i)] on the surface (marked by circles).

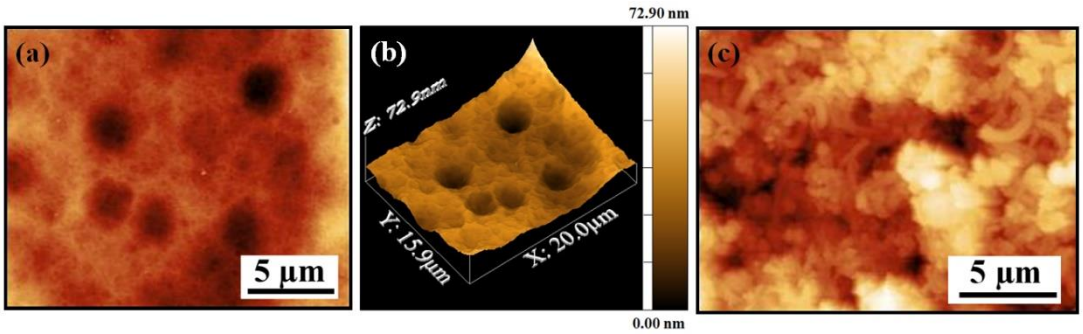

Figure 7.2: AFM micrographs of the coated film surface. (a, c) show the surface morphology with microcavities/holes. (b) 3D projection of surface (a).

AFM investigations on the coated films [Figure 7.2(a, b, c)] further support the evidence of interlinked CNT forests. We can also see microcavities [270,271], or holes [Figure 7.2(a, b)] on the surface. Since optical properties of the blackest coatings will hugely depend on the surface morphology and related light trapping abilities, the presence of these pores or holes will play an important role to trap light via multipole reflections [272] inside the cavities.

7.3. Spectral reflectance measurement

Hemispherical reflectance measurements have been carried out on the spray-coated samples using an integrating sphere attached to the spectrometer. Total reflectance of the coated film before and after subjecting to SEST is presented in Figure 7.3.(a). Our coated film shows broadband reflectance in the range 400-2500 nm [Figure 7.3.(a)]. For the

spectral band 500-1500 nm, almost a uniform variation of reflectance is observed with a minimum value of 2.3%.

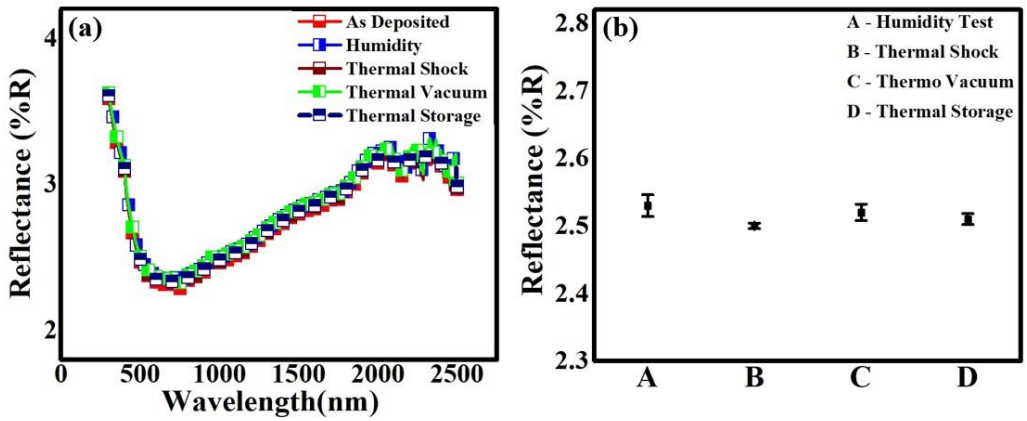

Figure 7.3: (a) Optical reflectance studies on the as-prepared coated film as well as after subjecting to various SEST. (b) The standard deviation of the mean reflectance values after performing SEST w.r.t. the as-prepared film.

Figure 7.3.(a) also shows reflectance spectra acquired after performing SEST namely humidity, thermal shock, thermal vacuum, thermal storage. As can be seen in Figure 7.3.(a), the reflectance spectrum obtained after each SEST exhibits identical behavior as that of the coated film which clearly demonstrates the stability of the film. In Figure 7.3.(b), we have plotted the standard deviation of the mean reflectance values obtained from the film after performing each SEST w.r.t. the value before the SEST (spectral range 500-1500 nm). It is clearly evident [Figure 7.3.(b)] that the variation of the mean reflectance values is very small and within the error limit. Percentage deviation is within 0.4-1.6 with the thermal shock test giving the lowest variation and the humidity test showing the highest.

Several earlier reports on broadband absorption observed in vertically aligned CNT forest were attributed to the formation of compound materials made up of individual nanotubes comprised of different chirality, bandgap, number of layers, etc. [267,270,271]. Here, trapping of light and multiple reflections happening within the cavities as well as in the nanotubes and nanoscrolls would contribute significantly to the observed low reflectance.

Post-growth processing of the CNT bundles and site densification [273–275] are necessary in order to achieve the desired property of the CNT-based films. Purification of the as-prepared SWCNTs by chemical oxidation is important to remove the catalyst and carbonaceous contaminants from the bundle network. This would also modify the CNT structures including cutting and opening them up. The functionalization process is carried out to enhance the solvation properties of the purified CNTs [269] which are usually in the form of bundles and ropes because of interfacial interaction, intrinsic vdWs force, and high aspect ratio [21]. Chemical functionalization involves covalent attachment of chemical groups through reactions onto the π- conjugated skeleton of the CNTs by forming a covalent linkage between the functional entities and the carbon skeleton of the tubes [178,269]. While direct covalent sidewall functionalization with carboxylic groups is associated with a change in hybridization from sp^2 to sp^3 [179,181,182], indirect covalent functionalization is due to the chemical transformation of the carboxylic groups at the open ends and holes in the sidewalls of the CNT surfaces. In the covalent functionalization process, the CNT structures are further destroyed, resulting in significant changes in their physical properties [21,178,266,268,276]. In addition to the parameters like diameter, length, orientation of the tubes; densification also plays a major role in altering the physical properties of the film. Stray light control application requires a successful fabrication of a stable film that could be achieved using a highly volatile solvent like acetone associated with a polymer binder. This makes the CNTs come in close contact due to the capillary coalescence effect and create a random porous network of dense CNT forests [275]. We have grown solvent-binder wetted layer-by-layer stacking of random forests of CNT-CNS composite film by a simple spray coating technique where evaporation of localized solvent will make CNTs and CNS come close to each other due to capillary forces, giving rise to porous mesh-like network [275]. Capillary-induced densification can lead to large size pores depending on the choice of solvents [275]. Evidence of macro-pores of diameter up to few microns observed on our film surface [Figure 7.1(i) and 7.2] could be related to the volatility of the solvent, capillary forces, and the transport of the colloidal particles [275,277]. These macro-pores

will play a vital role in the observed low reflectance value by efficiently trapping the incident light. It has been shown that refractive index, n, remains almost constant for a densified film compared to the pristine sample [274] and densification can reduce the film thickness by approximately 50% to obtain alike transmittance [274]. However, all these were discussed for wavelengths till 600 nm, much below our experimental range to draw any comparison. Ab initio and tight-binding calculations show that CNS, CNTs, and monolayer amorphous carbon sheets display similar absorption trends w.r.t. energy with a variation only in the intensity values [278]. In the UV-Vis spectral range, CNS exhibit a higher absorbance owing to their large curvature compared to CNTs and amorphous carbon sheets. In the spectral range approximately between 300 nm (~4.13 eV) to 800 nm (~1.55 eV), the absorbance of CNS is almost twice that of CNTs and amorphous carbon layers, while, reflectivity remains mostly constant [278]. The calculated reflectivity and refractive index curves also reveal an identical spectral nature for CNS, CNTs and the carbon sheets in the UV-Vis-IR range with a major part of the incident light getting absorbed between 1240 nm (1 eV) - 310 nm (4 eV) [278]. The spectral behavior of our reflectance data appears to be in good agreement with the theoretically predicted results[278]. This illustrates the possibility of these easily synthesized curved graphene composites, obtained via microstructural changes during the processing, as potential candidates for stray light control and optoelectronics applications [278].

7.4. Implementations of black absorber thin film coatings

CNT based coatings are a new trend in material science world. Achieving robust adhesion in CNT based black coatings poses significant challenges. The unique properties of CNTs, such as their high aspect ratio and low density, can make it challenging to ensure uniform and durable adhesion to various substrates. Properly bonding the CNTs within the coating matrix is crucial for maintaining the integrity and effectiveness of the black coating. Factors like surface preparation, coating application techniques, and the compatibility of CNTs with the substrate material play pivotal roles in addressing these

adhesion challenges. Developing innovative solutions to enhance adhesion will not only improve the durability of CNT-based black coatings but also expand their applicability in diverse industrial and technological contexts. Here, we are highlighting the challenges encountered during the preparation of the black absorber coatings. These challenges are listed below.

a) Uniformity of the coating
b) Long term stability of coating solution
c) Adhesion of the coating
d) Specular absorption property of the film
e) Uniform temperature gradient
f) Solvent-binder chemistry
g) Extent of functionalization or attachment of oxidized entities
h) Maintaining proper ratio among CNT composition, solvent and binder with particular frequency of ultrasonication process
i) Controlling frequency of ultrasonication without disturbing integrity of CNTs.

We have successfully overcome these issues by optimizing the parameters via performing repeated experiments until the goal is achieved which was a cumbersome process.

7.5. Adhesion test

Adhesion is an important physical property that is an indicator of proper bonding between the coated film and the substrate. For a coated film to fulfill its function, it should adhere to the substrate properly. We have studied the stability of the films by using the ‘scotch tape method’ which is a commonly used technique to assess the adhesion of the CNT coatings with the substrate surface. Figure 7.4 shows the sequence of the snapshots carried out on the coated film samples in our case. As can be seen [Figure 7.4], the film was gently pressed by using a normal scotch tape on the surface. In our case, the film is well adhered to the substrate, the peeled-off tape would not exhibit any signature of the

film coming out with the tape. Rather, only the impression of the loosely bound particles which are present on the film surface will be evident on the tape after removing it off.

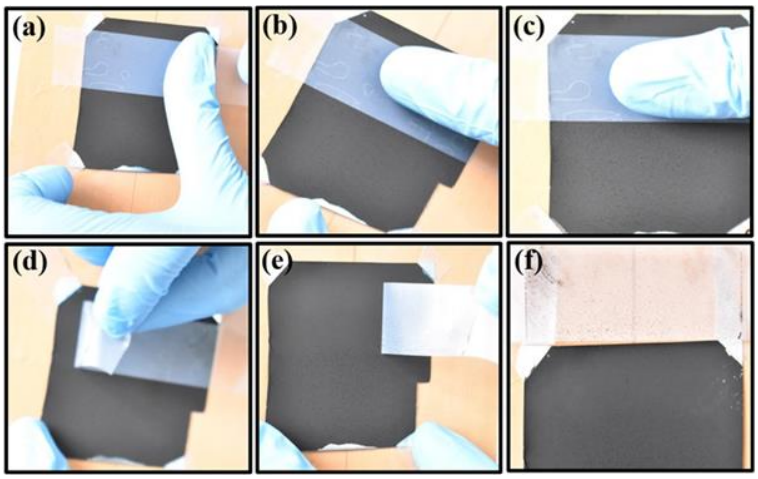

Figure 7.4: Sequential depiction of adhesion test performed on the coated film by using a scotch tape.

This can be clearly seen in Figure 7.4 where the signature of a very small amount of surface particles is only visible on the tape after performing the experiment. The visual analysis [Figure 7.4] confirms the high stability and viability of the CNT, CNS blended film coatings in terms of adhesion with the Al substrate. Well-dispersed CNTs in an Al matrix can pin dislocations driven by the capillary action during solvent evaporation and can form strong chemical bonds with substrate [279] exhibiting good film stability. A significant contribution would also come from the polyurethane binder due to its physico-chemical bonds, high elongation, and tensile strength. The success in the adhesion test allows us to proceed further with the SEST.

7.6. SESTs study

We have carried out elementary SEST on these coatings to check their sustainability for space-related applications. Any device which needs to be used in spacecraft has to survive in the space environment which is entirely different compared to ground conditions on

earth. CNT coatings have shown great promise in this field to be used for stray light control [270,280], bolometric measurements [270,272], and blackbody sources [270], etc. to name a few. In that series of experiments, the primary tests include survival of these coatings throughout the launch environments like vibration, humidity, shock, temperature extremes, etc. In the humidity test, moisture is allowed to ingress into the surface which may lead to oxidation, and hence there is a large probability that the properties of the coating will degrade. However, our sample subjected to the humidity test exhibits good stability without any trace of decay in its optical absorptance property. The samples exposed to thermal shock, thermal storage, and thermo-vacuum cycling tests also indicate that the stress and strain due to temperature variations are not affecting the film demonstrating the stability of these coatings under different environmental conditions.

Tests	**Tests Conditions**	**Average Reflectance (500 - 1500 nm) (%)**	**Deviation in reflectance w.r.t. (*) (%)**
As-prepared sample (*)	-----	2.49	-----
Humidity	95% relative humidity, 50ºC	2.53	1.6
Thermal Shock	-30ºC to +70ºC, 500 cycles	2.50	0.4
Thermal Storage	-50ºC to +80ºC, 10 cycles, 2hrs dwell time	2.52	0.8
Thermal Vacuum Cycling	-50ºC to +80ºC, 2 hrs dwell time, $1x10^{-5}$mbar, 5 cycles	2.51	1.2

Table 7.1: SEST and the spectral properties of the spray-coated sample. Average reflectance values after performing SEST remain within the error limit w.r.t. the as-prepared coated film (*).

From Table 7.1, one can see that the average reflectance (%) has not changed after performing SEST. The samples do not exhibit any difference either visually [Figure 7.4] or in spectral reflectance measurements [Figure 7.3. and Table 7.1] before and after subjecting to the SEST. Details of the SEST are given in Table 7.1.

7.7. Prototype application of vanes coated with the carbon composite thin films

These CNT-polymer based composite films are highly useful in different areas. Frequent applications of CNT-based thin film coatings are found wherever stray light needs to be controlled, such as coatings for thermal detectors and baffles, various optical components, sensors, space telescopes, and components in spacecraft.

Figure 7.5: Final assembly of coated vanes for the actual prototype of spacecraft for stray light control application.

As the spray coating method is very flexible so it is highly useful and easy to access to coat sharp edge objects. The final prototype of the unit is shown in Figure 7.5.

7.8. Conclusion

In this chapter, we explored morphological transformations in the purified, functionalized, and coated samples through SEM and AFM analyses. The absorption

characteristics of the coated samples were confirmed through UV-Vis-NIR spectroscopy. These films were subjected to the SESTs including humidity, thermal storage, thermal vacuum cycling and thermal shock. Across the spectral band of 500-1500 nm, a nearly consistent variation in reflectance is evident, reaching a minimum value of 2.3%. Adhesion test of the coatings was the crucial step coupled with visual inspections, and was performed successfully before deploying the films to control stray light in space units.

CHAPTER 8

Conclusion and future perspective

8.1. Conclusion

Research on blackest coatings using carbon materials continues to be an evolving field of study. The optical properties of carbon based coatings need to be tuned according to the requirement and application. The task of making adequate coatings for specific applications by tailoring the growth process, surface preparation, and modification is still under progress. As a result, thin films of carbon materials have received enormous attention for developing high absorber coatings for stray light control applications in thermal detectors and baffles, various optical components, sensors, space telescopes, spacecraft components etc. Herein, we report a facile, cost-effective method of fabricating stable coatings comprised of CNTs, CNS, GS and other low dimensional structural derivatives of carbon on flexible Al substrate via a simple spray coating technique for stray light control applications in the space domain. We discuss in this work the action of oxidizing acid purification and covalent functionalization on the as-prepared SWCNT bundles and their structural decomposition due to chemical modification via attachment of various functional groups. Spectroscopy, microscopy and microstructural studies demonstrate emergence of MWCNTs, GS, CNS and other low dimensional structural components of carbon as a result of processing-induced modifications to the as-prepared SWCNTs.

CNS, an emerging 1D helical form of carbon with its unique structure and superior properties has received enormous attention recently where main focus is on their synthesis, fabrication and looking for new properties for industrial implementation. Although a plethora of investigations carried out on MWCNTs demonstrate their highly promising optical absorption properties, studies on CNS are still in its beginning. It is predicted that CNS could be a better candidate than CNTs in this regard [273]. We demonstrate here beautiful manifestation of CNS from the SWCNT networks via a simple oxidative route of purification for the first time. The purified sample not only exhibits a high degree of reduction in the contaminant metal particles and amorphous carbon, it also shows evidence of MWCNTs, GS and CNS. Reflux action involving wet oxidation, HCl wash and annealing at 900°C was crucial to develop a solution based

oxidative route for successful merging, exfoliation and unzipping of SWCNTs to MWCNTs and GS and subsequent formation of CNS via curling and folding of GS. Signature of radial merging, catalyst particle induced axial tearing of the SWCNT bundles, chemical cutting, as well as stress and strain induced tearing of CNS and their unraveling to GS are also clearly observed. The GS, thus, formed would again contribute in forming CNS due to presence of the functional groups in the treated sample. We present our stepwise systematic investigations and analysis towards the microstructural and chemical changes occurring to the as-prepared SWCNTs. Covalent functionalization further induces significant number of functional groups to the structures revealing a general trend of increase in the diameter of the tubes and signature of short and distorted CNTs and CNS compared to the purified data. An intriguing understanding is developed via performing functional group analysis, Raman spectroscopy studies, XRD investigations, morphology and microstructure analyses by TEM and SEM.

Thin films of these heterogeneous carbon derivatives amalgamated in polyurethane matrix on Al substrate are further studied by spectral reflectance measurements, microstructural analysis, and SESTs. These coated films demonstrate promising results by exhibiting a low reflectance of the order of 2-3% in the Vis-NIR spectral bands, especially in the range 500-1500 nm where light reflectance is 2.3-2.8%. Microstructural investigations including SEM and AFM confirm the presence of microcavities and pores on the surface of the films. These cavities and pores would significantly contribute to the observed low reflectance value of these compound films by trapping incident light via multiple reflections. Fundamental SEST performed on the coated films show good stability and endurance to harsh space conditions with their reflectance values unaltered, demonstrating the durability of these films as potential candidates to be used in extreme space environmental conditions. This study describes the preparation, characterization, and testing of blended heterogeneous low dimensional derivatives of carbon coatings for low-light scattering applications. We develop a process for successful fabrication of stable composite film coatings comprised of random network of functionalized carbon nanomaterials and polymer conjugate without going into non-trivial process of separating

the structural components. This work is now directly implemented to make coatings on vanes/baffles in space components.

8.2. Future perspective

The future applications of these thin films derived from CNTs exhibit significant potential across diverse realms of nanoscience and technology. The CNT-based black absorber thin films can be strategically utilized in solar systems to enhance energy absorption in areas such as thermal management, where these films can efficiently absorb and dissipate heat. Additionally, their potential application extends to corrosion protective paints for large wind blades in wind mills, UV based sensors and photo detectors in space exploration, where they can serve as coatings on satellite surfaces, enhancing thermal control and mitigating the impact of intense solar radiation. The unique properties of CNT-based black absorber thin films position them as innovative solutions for addressing challenges in renewable energy, thermal regulation, and space technology.

References

[1] S. Iijima, Helical microtubules of graphitic carbon, Nature. 354 (1991) 56–58. https://doi.org/10.1038/354056a0.

[2] B.R.C. De Menezes, K.F. Rodrigues, B.C.D.S. Fonseca, R.G. Ribas, T.L.D.A. Montanheiro, G.P. Thim, Recent advances in the use of carbon nanotubes as smart biomaterials, Journal of Materials Chemistry B. 7 (2019) 1343–1360. https://doi.org/10.1039/c8tb02419g.

[3] X. Wang, A. Dong, Y. Hu, J. Qian, S. Huang, A review of recent work on using metal-organic frameworks to grow carbon nanotubes, Chemical Communications. 56 (2020) 10809–10823. https://doi.org/10.1039/d0cc04015k.

[4] X. Zhao, H. Chen, F. Kong, Y. Zhang, S. Wang, S. Liu, L.A. Lucia, P. Fatehi, H. Pang, Fabrication, characteristics and applications of carbon materials with different morphologies and porous structures produced from wood liquefaction: A review, Chemical Engineering Journal. 364 (2019) 226–243. https://doi.org/10.1016/j.cej.2019.01.159.

[5] Л.В.М. Радушкевич, Л. В, О Структуре Углерода, Образующегося При Термическом Разложении Окиси Углерода На Железном Контакте, Журнал Физической Химии (in Russian). 26 (1952) 88–95.

[6] R. Bacon, Growth, structure, and properties of graphite whiskers, Journal of Applied Physics. 31 (1960) 283–290. https://doi.org/10.1063/1.1735559.

[7] A. Oberlin, M. Endo, T. Koyama, Filamentous growth of carbon through benzene decomposition, Journal of Crystal Growth. 32 (1976) 335–349. https://doi.org/10.1016/0022-0248(76)90115-9.

[8] K. Square, P.E.J. Van Balen, Carbon fibrils, method for producing same and compositions containing same, Composites. 19 (1988) 255. https://doi.org/10.1016/0010-4361(88)90324-2.

[9] S. Iijima, T. Ichihashi, Single-shell carbon nanotubes of 1-nm diameter, Nature. 363 (1993) 603–605. https://doi.org/10.1038/363603a0.

[10] C.H. Kiang, M.S. Devries, G. Gorman, R. Savoy, D.S. Bethune, C.H. Klang, M.S. de-Vries, J. Vazquez, R. Beyers, Cobalt-catalysed growth of carbon nanotubes with single-atomic-layer walls, Nature. 363 (1993) 605–607. http://doi.org/10.1038/363605a0

[11] Sumio Iijima and Toshinari Ichihashi, 1-Nm Diameter, Nature. (1993) 603–605.

[12] E. T., A. A., H. H., T. T., Purification of nanotubes, Nature. 367 (1994) 519–520.

[13] N.G. Chopra, L.X. Benedict, V.H. Crespi, M.L. Cohen, S.G. Louie, A. Zettl, Fully collapsed carbon nanotubes, Nature. 377 (1995) 135–138. https://doi.org/10.1038/377135a0.

[14] J.Q. Xi, M.F. Schubert, J.K. Kim, E.F. Schubert, M. Chen, S.Y. Lin, W. Liu, J.A. Smart, Optical thin-film materials with low refractive index for broadband elimination of Fresnel reflection, Nature Photonics. 1 (2007) 176–179. https://doi.org/10.1038/nphoton.2007.26.

[15] M. Meyyappan, SCIENCE AND APPLICATIONS EDITED BY, n.d.

[16] D.A.M.A. John Edward Proctor, and A. Vijayaraghavan, An Introduction to Graphene and Carbon Nanotubes, ISBN: 1498751792.

[17] S. Kumar, R. Rani, N. Dilbaghi, K. Tankeshwar, K.H. Kim, Carbon nanotubes: A novel material for multifaceted applications in human healthcare, Chemical Society Reviews. 46 (2017) 158–196. https://doi.org/10.1039/c6cs00517a.

[18] S.K. Soni, B. Thomas, V.R. Kar, A Comprehensive Review on CNTs and CNT-Reinforced Composites: Syntheses, Characteristics and Applications, Materials Today Communications. 25 (2020) 101546. https://doi.org/10.1016/j.mtcomm.2020.101546.

[19] Z. Yin, C. Cui, H. Chen, Duoni, X. Yu, W. Qian, The Application of Carbon Nanotube/Graphene-Based Nanomaterials in Wastewater Treatment, Small. 16 (2020) 1–16. https://doi.org/10.1002/smll.201902301.

[20] D. Tasis, N. Tagmatarchis, A. Bianco, M. Prato, Chemistry of carbon nanotubes, Chemical Reviews. 106 (2006) 1105–1136. https://doi.org/10.1021/cr050569o.
[21] B. Bhushan, ed., Springer Handbook of Nanotechnology, Springer Berlin Heidelberg, Berlin, Heidelberg, Heidelberg, 2007. https://doi.org/10.1007/978-3-540-29857-1.
[22] C. Hong An Wong, M. Pumera, Unscrolling of multi-walled carbon nanotubes: Towards micrometre-scale graphene oxide sheets, Physical Chemistry Chemical Physics. 15 (2013) 7755–7759. https://doi.org/10.1039/c3cp51026c.
[23] O. V. Kharissova, B.I. Kharisov, Variations of interlayer spacing in carbon nanotubes, RSC Advances. 4 (2014) 30807–30815. https://doi.org/10.1039/c4ra04201h.
[24] D. Xia, J. Xie, H. Chen, C. Lv, F. Besenbacher, Q. Xue, M. Dong, Fabrication of carbon nanoscrolls from monolayer graphene, Small. 6 (2010) 2010–2019. https://doi.org/10.1002/smll.201000646.
[25] M.M. Zaeri, S. Ziaei-Rad, Elastic properties of carbon nanoscrolls, RSC Advances. 4 (2014) 22995–23001. https://doi.org/10.1039/c4ra01931h.
[26] V.P. Reddy, General Aspects of Organofluorine Compounds, in: Organofluorine Compounds in Biology and Medicine, Elsevier, 2015: pp. 1–27. https://doi.org/10.1016/B978-0-444-53748-5.00001-0.
[27] S. Saini, S. Reshmi, G.M. Gouda, K. Bhattacharjee, Emergence of carbon nanoscrolls from single walled carbon nanotubes: an oxidative route, Physical Chemistry Chemical Physics. 23 (2021) 27437–27448. https://doi.org/10.1039/d1cp03945h.
[28] S. Saini, S. Reshmi, G.M. Gouda, A. Kumar S., S. K. V., K. Bhattacharjee, Low reflectance of carbon nanotube and nanoscroll-based thin film coatings: a case study, Nanoscale Advances. 3 (2021) 3184–3198. https://doi.org/10.1039/d0na01058h.
[29] V. Meunier, M.B. Nardelli, J. Bernholc, T. Zacharia, J.C. Charlier, Intrinsic electron transport properties of carbon nanotube Y-junctions, Applied Physics Letters. 81 (2002) 5234–5236. https://doi.org/10.1063/1.1533842.
[30] S.Y. Kim, I.H. Lee, S. Jun, Y. Lee, S. Im, Coalescence and T-junction formation of carbon nanotubes: Action-derived molecular dynamics simulations, Physical Review B - Condensed Matter and Materials Physics. 74 (2006) 1–8. https://doi.org/10.1103/PhysRevB.74.195409.
[31] R. Sen, B.C. Satishkumar, A. Govindaraj, K.R. Harikumar, M.K. Renganathan, C.N.R. Rao, Nitrogen-containing carbon nanotubes, Journal of Materials Chemistry. 7 (1997) 2335–2337. https://doi.org/10.1039/a705891h.
[32] A.K. Haghi, G.E. Zaikov, Carbon nanotubes and related structures, Handbook of Research on Functional Materials: Principles, Capabilities and Limitations. 58 (2016) 147–254. https://doi.org/10.1201/b16444-5.
[33] C.S. Haines, N. Li, G.M. Spinks, A.E. Aliev, J. Di, R.H. Baughman, New twist on artificial muscles, Proceedings of the National Academy of Sciences. 113 (2016) 11709–11716. https://doi.org/10.1073/pnas.1605273113.
[34] D.C. Elias, R.R. Nair, T.M.G. Mohiuddin, S. V. Morozov, P. Blake, M.P. Halsall, A.C. Ferrari, D.W. Boukhvalov, M.I. Katsnelson, A.K. Geim, K.S. Novoselov, Control of Graphene's Properties by Reversible Hydrogenation: Evidence for Graphane, Science. 323 (2009) 610–613. https://doi.org/10.1126/science.1167130.
[35] R.L.D. Whitby, Chemical control of graphene architecture: Tailoring shape and properties, ACS Nano. 8 (2014) 9733–9754. https://doi.org/10.1021/nn504544h.
[36] R. Dubey, D. Dutta, A. Sarkar, P. Chattopadhyay, Functionalized carbon nanotubes: synthesis, properties and applications in water purification, drug delivery, and material and biomedical sciences, Nanoscale Advances. 3 (2021) 5722–5744. https://doi.org/10.1039/d1na00293g.
[37] A. Benko, J. Duch, M. Gajewska, M. Marzec, A. Bernasik, M. Nocuń, W. Piskorz, A. Kotarba, Covalently bonded surface functional groups on carbon nanotubes: From molecular modeling to

practical applications, Nanoscale. 13 (2021) 10152–10166. https://doi.org/10.1039/d0nr09057c.
[38] M.S. Strano, C.A. Dyke, M.L. Usrey, P.W. Barone, M.J. Allen, H. Shan, C. Kittrell, R.H. Hauge, J.M. Tour, R.E. Smalley, Electronic structure control of single-waited carbon nanotube functionalization, Science. 301 (2003) 1519–1522. https://doi.org/10.1126/science.1087691.
[39] C. Wang, X. Ma, S. Ye, L. Cheng, K. Yang, L. Guo, C. Li, Y. Li, Z. Liu, Protamine functionalized single-walled carbon nanotubes for stem cell labeling and in vivo Raman/magnetic resonance/photoacoustic triple-modal imaging, Advanced Functional Materials. 22 (2012) 2363–2375. https://doi.org/10.1002/adfm.201200133.
[40] X. Li, B. Wu, Y. Li, M.M. Alam, P. Chen, R. Xia, C. Te Lin, J. Qian, Construction of Oriented Interconnected BNNS Skeleton by Self-Growing CNTs Leading High Thermal Conductivity, Advanced Materials Interfaces. 8 (2021) 1–9. https://doi.org/10.1002/admi.202001910.
[41] S.Y. Brichka, M.I. Terets, O.I. Svistova, S.L. Revo, Mechanical properties of carbon nanotubes, Scientific Herald of Uzhhorod University.Series Physics. 16 (2004) 104–108. https://doi.org/10.24144/2415-8038.2004.16.104-108.
[42] N. Khandoker, S.C. Hawkins, R. Ibrahim, C.P. Huynh, F. Deng, Tensile Strength of Spinnable Multiwall Carbon Nanotubes, Procedia Engineering. 10 (2011) 2572–2578. https://doi.org/10.1016/j.proeng.2011.04.424.
[43] R. Sharma, P. Benjwal, K.K. Kar, Carbon Nanotubes: Synthesis, Properties and Applications, 2015. https://doi.org/10.1002/9781119179108.ch4.
[44] B. Pradhan, S.K. Batabyal, A.J. Pal, Functionalized carbon nanotubes in donor/acceptor-type photovoltaic devices, Applied Physics Letters. 88 (2006) 2–5. https://doi.org/10.1063/1.2179372.
[45] D.A. Walters, L.M. Ericson, M.J. Casavant, J. Liu, D.T. Colbert, K.A. Smith, R.E. Smalley, Elastic strain of freely suspended single-wall carbon nanotube ropes, Applied Physics Letters. 74 (1999) 3803–3805. https://doi.org/10.1063/1.124185.
[46] F. Li, H.M. Cheng, S. Bai, G. Su, M.S. Dresselhaus, Tensile strength of single-walled carbon nanotubes directly measured from their macroscopic ropes, Applied Physics Letters. 77 (2000) 3161–3163. https://doi.org/10.1063/1.1324984.
[47] T.H. Nam, K. Goto, Y. Yamaguchi, E.V.A. Premalal, Y. Shimamura, Y. Inoue, K. Naito, S. Ogihara, Effects of CNT diameter on mechanical properties of aligned CNT sheets and composites, Composites Part A: Applied Science and Manufacturing. 76 (2015) 289–298. https://doi.org/10.1016/j.compositesa.2015.06.009.
[48] E.W. Wong, P.E. Sheehan, C.M. Lieber, Nanobeam mechanics: Elasticity, strength, and toughness of nanorods and nanotubes, Science. 277 (1997) 1971–1975. https://doi.org/10.1126/science.277.5334.1971.
[49] S. Iijima, C. Brabec, A. Maiti, J. Bernholc, Structural flexibility of carbon nanotubes, Journal of Chemical Physics. 104 (1996) 2089–2092. https://doi.org/10.1063/1.470966.
[50] M. Estili, A. Kawasaki, Y. Sakka, Highly concentrated 3D macrostructure of individual carbon nanotubes in a ceramic environment, Advanced Materials. 24 (2012) 4322–4326. https://doi.org/10.1002/adma.201201134.
[51] C. Nanotube, I. Suspended, Fast Electromechanical Switches Based on Carbon Nanotubes, (2008) 1–5.
[52] B. Earp, D. Dunn, J. Phillips, R. Agrawal, T. Ansell, P. Aceves, I. De Rosa, W. Xin, C. Luhrs, Enhancement of electrical conductivity of carbon nanotube sheets through copper addition using reduction expansion synthesis, Materials Research Bulletin. 131 (2020) 110969. https://doi.org/10.1016/j.materresbull.2020.110969.
[53] P.J.F. Harris, Carbon nanotube composites, International Materials Reviews. 49 (2004) 31–43. https://doi.org/10.1179/095066004225010505.
[54] A. Lekawa-Raus, J. Patmore, L. Kurzepa, J. Bulmer, K. Koziol, Electrical properties of carbon

nanotube based fibers and their future use in electrical wiring, Advanced Functional Materials. 24 (2014) 3661–3682. https://doi.org/10.1002/adfm.201303716.
[55] Q. Li, Y. Li, X. Zhang, S.B. Chikkannanavar, Y. Zhao, A.M. Dangelewicz, L. Zheng, S.K. Doorn, Q. Jia, D.E. Peterson, P.N. Arendt, Y. Zhu, Structure-dependent electrical properties of carbon nanotube fibers, Advanced Materials. 19 (2007) 3358–3363. https://doi.org/10.1002/adma.200602966.
[56] D. Janas, K.Z. Milowska, P.D. Bristowe, K.K.K. Koziol, Improving the electrical properties of carbon nanotubes with interhalogen compounds, Nanoscale. 9 (2017) 3212–3221. https://doi.org/10.1039/c7nr00224f.
[57] M. Nihei, A. Kawabata, D. Kondo, M. Horibe, S. Sato, Y. Awano, Electrical properties of carbon nanotube bundles for future via interconnects, Japanese Journal of Applied Physics, Part 1: Regular Papers and Short Notes and Review Papers. 44 (2005) 1626–1628. https://doi.org/10.1143/JJAP.44.1626.
[58] L. Qian, Y. Xie, S. Zhang, J. Zhang, Band Engineering of Carbon Nanotubes for Device Applications, Matter. 3 (2020) 664–695. https://doi.org/10.1016/j.matt.2020.06.014.
[59] H. Kataura, Y. Kumazawa, Y. Maniwa, I. Umezu, S. Suzuki, Y. Ohtsuka, Y. Achiba, Optical properties of single-wall carbon nanotubes, Synthetic Metals. 103 (1999) 2555–2558. https://doi.org/10.1016/S0379-6779(98)00278-1.
[60] R. Saito, A. Grüneis, G.G. Samsonidze, G. Dresselhaus, M.S. Dresselhaus, A. Jorio, L.G. Cançado, M.A. Pimenta, A.G.S. Filho, Optical absorption of graphite and single-wall carbon nanotubes, Applied Physics A: Materials Science and Processing. 78 (2004) 1099–1105. https://doi.org/10.1007/s00339-003-2459-z.
[61] D.K. Singh, P.K. Iyer, P.K. Giri, Optical Signature of Structural Defects in Single Walled and Multiwalled Carbon Nanotubes, Journal of Nanoscience and Nanotechnology. 9 (2009) 5396–5401. https://doi.org/10.1166/jnn.2009.1139.
[62] S. Van Bezouw, D.H. Arias, R. Ihly, S. Cambré, A.J. Ferguson, J. Campo, J.C. Johnson, J. Defillet, W. Wenseleers, J.L. Blackburn, Diameter-Dependent Optical Absorption and Excitation Energy Transfer from Encapsulated Dye Molecules toward Single-Walled Carbon Nanotubes, ACS Nano. 12 (2018) 6881–6894. https://doi.org/10.1021/acsnano.8b02213.
[63] M.F. Lin, K.W.K. Shung, Plasmons and optical properties of carbon nanotubes, Physical Review B. 50 (1994) 17744–17747. https://doi.org/10.1103/PhysRevB.50.17744.
[64] Y. Jin, T. Zhang, J. Zhao, Y. Zhao, C. Liu, J. Song, X. Hao, J. Wang, K. Jiang, S. Fan, Q. Li, Spray coating of a perfect absorber based on carbon nanotube multiscale composites, Carbon. 178 (2021) 616–624. https://doi.org/10.1016/j.carbon.2021.03.019.
[65] E. Theocharous, C.J. Chunnilall, R. Mole, D. Gibbs, N. Fox, N. Shang, G. Howlett, B. Jensen, R. Taylor, J.R. Reveles, O.B. Harris, N. Ahmed, The partial space qualification of a vertically aligned carbon nanotube coating on aluminium substrates for EO applications, Optics Express. 22 (2014) 7290. https://doi.org/10.1364/OE.22.007290.
[66] A.P. Leggiero, K.J. Trettner, H.L. Ursino, D.J. McIntyre, M. Schauer, E. Zeira, C.D. Cress, B.J. Landi, High Conductivity Copper-Carbon Nanotube Hybrids via Site-Specific Chemical Vapor Deposition, ACS Applied Nano Materials. 2 (2019) 118–126. https://doi.org/10.1021/acsanm.8b01740.
[67] R.M. Tromer, L.C. Felix, L.A. Ribeiro, D.S. Galvao, Optoelectronic properties of amorphous carbon-based nanotube and nanoscroll, Physica E: Low-Dimensional Systems and Nanostructures. 130 (2021) 114683. https://doi.org/10.1016/j.physe.2021.114683.
[68] A.N. Andriotis, M. Menon, D. Srivastava, L. Chernozatonskii, Rectification Properties of Carbon Nanotube "Y-Junctions," Physical Review Letters. 87 (2001) 66802-1-66802–4. https://doi.org/10.1103/PhysRevLett.87.066802.

[69] C. Hontoria-Lucas, A.J. López-Peinado, J. de D. López-González, M.L. Rojas-Cervantes, R.M. Martín-Aranda, Study of oxygen-containing groups in a series of graphite oxides: Physical and chemical characterization, Carbon. 33 (1995) 1585–1592. https://doi.org/10.1016/0008-6223(95)00120-3.
[70] C. Journet, W.K. Maser, P. Bernier, A. Loiseau, letters to nature Large-scale production of single-walled carbon nanotubes by the electric-arc technique, 388 (1997) 20–22.
[71] Z. Shi, Y. Lian, F. Hui, X. Zhou, Z. Gu, Y. Zhang, S. Iijima, H. Li, K. To, S. Zhang, Large scale synthesis of single-wall carbon nanotubes by arc-discharge method ☪, 61 (2000) 1031–1036.
[72] A. Thess, R. Lee, P. Nikolaev, H. Dai, P. Petit, J. Robert, C. Xu, Y.H. Lee, S.G. Kim, A.G. Rinzler, D.T. Colbert, G.E. Scuseria, D. Tománek, J.E. Fischer, R.E. Smalley, Crystalline Ropes of Metallic Carbon Nanotubes, Science. 273 (1996) 483–487. https://doi.org/10.1126/science.273.5274.483.
[73] T. Guo, P. Nikolaev, A. Thess, D.T. Colbert, R.E. Smalley, Catalytic growth of single-walled manotubes by laser vaporization, Chemical Physics Letters. 243 (1995) 49–54. https://doi.org/10.1016/0009-2614(95)00825-O.
[74] T.S. Chemistry, Y.S. Kim, C.J. Bennett, A. Bergantini, R. Frigge, R.I. Kaiser, Synthesis of Carbon Nanotubes (CNT) by Chemical Vapor Deposition (CVD) using a biogas- based carbon precursor : A review Synthesis of Carbon Nanotubes (CNT) by Chemical Vapor Deposition (CVD) using a biogas-based carbon precursor : A review, IOP Publication. 959 (2020). https://doi.org/10.1088/1757-899X/959/1/012019.
[75] A. Yahyazadeh, B. Khoshandam, Results in Physics Carbon nanotube synthesis via the catalytic chemical vapor deposition of methane in the presence of iron , molybdenum , and iron – molybdenum alloy thin layer catalysts, Results in Physics. 7 (2017) 3826–3837. https://doi.org/10.1016/j.rinp.2017.10.001.
[76] P. Nikolaev, Gas-Phase Production of Single-Walled Carbon Nanotubes from Carbon Monoxide: A Review of the HiPco Process, Journal of Nanoscience and Nanotechnology. 4 (2004) 307–316. https://doi.org/10.1166/jnn.2004.066.
[77] M.J. Bronikowski, P.A. Willis, D.T. Colbert, K.A. Smith, R.E. Smalley, Gas-phase production of carbon single-walled nanotubes from carbon monoxide via the HiPco process: A parametric study, Journal of Vacuum Science & Technology A: Vacuum, Surfaces, and Films. 19 (2001) 1800–1805. https://doi.org/10.1116/1.1380721.
[78] P. Nikolaev, M.J. Bronikowski, R.K. Bradley, F. Rohmund, D.T. Colbert, K.A. Smith, R.E. Smalley, Gas-phase catalytic growth of single-walled carbon nanotubes from carbon monoxide, Chemical Physics Letters. 313 (1999) 91–97. https://doi.org/10.1016/S0009-2614(99)01029-5.
[79] C. Yang, K. Kaneko, M. Yudasaka, S. Iijima, Effect of Purification on Pore Structure of HiPco Single-Walled Carbon Nanotube Aggregates, Nano Letters. 2 (2002) 385–388. https://doi.org/10.1021/nl015652f.
[80] M.A. Godwin, A.B. Allannavar, S. Joshi, G. Reddy, S.S. Abhishek, R.K. Bradley, An Efficient Method to Completely Remove Catalyst Particles from HiPCO Single Walled Carbon Nanotubes, Journal of Nano Research. 53 (2018) 64–75. https://doi.org/10.4028/www.scientific.net/JNanoR.53.64.
[81] P.X. Hou, C. Liu, H.M. Cheng, Purification of carbon nanotubes, Carbon. 46 (2008) 2003–2025. https://doi.org/10.1016/j.carbon.2008.09.009.
[82] C.M. Yang, K. Kaneko, M. Yudasaka, S. Iijima, Surface chemistry and pore structure of purified HiPco single-walled carbon nanotube aggregates, Physica B: Condensed Matter. 323 (2002) 140–142. https://doi.org/10.1016/S0921-4526(02)00880-3.
[83] E. Vázquez, V. Georgakilas, M. Prato, Microwave-assisted purification of HIPCO carbon nanotubes, Chem. Commun. (2002) 2308–2309. https://doi.org/10.1039/B207436B.

[84] K.S. Ibrahim, Carbon nanotubes-properties and applications: a review, Carbon Letters. 14 (2013) 131–144. https://doi.org/10.5714/CL.2013.14.3.131.
[85] J.. Kirk, Chemistry and physics of carbon. Vol.19, Endeavour. 9 (1985) 152. https://doi.org/10.1016/0160-9327(85)90130-9.
[86] Pierre Delhaes, Graphite and precusors, ISBN: 90-6599-228-7, ISSN: 1560-8557.
[87] M.J. O'Connell, S.H. Bachilo, C.B. Huffman, V.C. Moore, M.S. Strano, E.H. Haroz, K.L. Rialon, P.J. Boul, W.H. Noon, C. Kittrell, J. Ma, R.H. Hauge, R.B. Weisman, R.E. Smalley, Band gap fluorescence from individual single-walled carbon nanotubes, Science. 297 (2002) 593–596. https://doi.org/10.1126/science.1072631.
[88] B. White, S. Banerjee, S. O'Brien, N.J. Turro, I.P. Herman, Zeta-potential measurements of surfactant-wrapped individual single-walled carbon nanotubes, Journal of Physical Chemistry C. 111 (2007) 13684–13690. https://doi.org/10.1021/jp070853e.
[89] P. Chungchamroenkit, S. Chavadej, U. Yanatatsaneejit, B. Kitiyanan, Residue catalyst support removal and purification of carbon nanotubes by NaOH leaching and froth flotation, Separation and Purification Technology. 60 (2008) 206–214. https://doi.org/10.1016/j.seppur.2007.08.009.
[90] A. Rinaldi, B. Frank, D.S. Su, S.B.A. Hamid, R. Schlögl, Facile Removal of Amorphous Carbon from Carbon Nanotubes by Sonication, Chemistry of Materials. 23 (2011) 926–928. https://doi.org/10.1021/cm103069z.
[91] H. Ribeiro, M.C. Schnitzler, W.M. da Silva, A.P. Santos, Purification of carbon nanotubes produced by the electric arc-discharge method, Surfaces and Interfaces. 26 (2021) 101389. https://doi.org/10.1016/j.surfin.2021.101389.
[92] S. Fogden, R. Verdejo, B. Cottam, M. Shaffer, Purification of single walled carbon nanotubes: The problem with oxidation debris, Chemical Physics Letters. 460 (2008) 162–167. https://doi.org/10.1016/j.cplett.2008.05.069.
[93] H. Yoon, R. Thompson, B. Hwang, Dispersibility study of carbon nanotubes using multiple light scattering: A mini-review, Colloid and Interface Science Communications. 52 (2023) 100686. https://doi.org/10.1016/j.colcom.2022.100686.
[94] M.N. Norizan, M.H. Moklis, S.Z. Ngah Demon, N.A. Halim, A. Samsuri, I.S. Mohamad, V.F. Knight, N. Abdullah, Carbon nanotubes: Functionalisation and their application in chemical sensors, RSC Advances. 10 (2020) 43704–43732. https://doi.org/10.1039/d0ra09438b.
[95] T. Sun, T. Zeng, C. Xia, S. Li, H. Wu, Purification and separation of single-walled carbon nanotubes (SWCNTs), Journal of Nanoscience and Nanotechnology. 12 (2012) 2955–2963. https://doi.org/10.1166/jnn.2012.5741.
[96] Y. Wang, H. Shan, R.H. Hauge, M. Pasquali, R.E. Smalley, A highly selective, one-pot purification method for single-walled carbon nanotubes, Journal of Physical Chemistry B. 111 (2007) 1249–1252. https://doi.org/10.1021/jp068229.
[97] S. Gajewski, H.-E. Maneck, U. Knoll, D. Neubert, I. Dörfel, R. Mach, B. Strauß, J.F. Friedrich, Purification of single walled carbon nanotubes by thermal gas phase oxidation, Diamond and Related Materials. 12 (2003) 816–820. https://doi.org/10.1016/S0925-9635(02)00362-X.
[98] Y. Liu, L. Gao, J. Sun, S. Zheng, L. Jiang, Y. Wang, H. Kajiura, Y. Li, K. Noda, A multi-step strategy for cutting and purification of single-walled carbon nanotubes, Carbon. 45 (2007) 1972–1978. https://doi.org/10.1016/j.carbon.2007.06.009.
[99] J.L. Zimmerman, R.K. Bradley, C.B. Huffman, R.H. Hauge, J.L. Margrave, Gas-Phase Purification of Single-Wall Carbon Nanotubes, 34 (2000) 1361–1366.
[100] J.-M. Moon, K.H. An, Y.H. Lee, Y.S. Park, D.J. Bae, G.-S. Park, High-Yield Purification Process of Singlewalled Carbon Nanotubes, The Journal of Physical Chemistry B. 105 (2001) 5677–5681. https://doi.org/10.1021/jp0102365.
[101] X.Y. Zhu, S.M. Lee, Y.H. Lee, T. Frauenheim, Adsorption and Desorption of an O_2 Molecule on

Carbon Nanotubes, Physical Review Letters. 1 (2000) 2757–2760. https://10.1103/PhysRevLett.85.2757
[102] M. Monthioux, B.W. Smith, B. Burteaux, A. Claye, J.E. Fischer, D.E. Luzzi, Sensitivity of single-wall carbon nanotubes to chemical processing: An electron microscopy investigation, Carbon. 39 (2001) 1251–1272. https://doi.org/10.1016/S0008-6223(00)00249-9.
[103] Z. Jia, Z. Wang, J. Liang, B. Wei, D. Wu, Production of short multi-walled carbon nanotubes, Carbon. 37 (1999) 903–906. https://doi.org/10.1016/S0008-6223(98)00229-2.
[104] Y. Mackeyev, S. Bachilo, K.B. Hartman, L.J. Wilson, The purification of HiPco SWCNTs with liquid bromine at room temperature, Carbon. 45 (2007) 1013–1017. https://doi.org/10.1016/j.carbon.2006.12.026.
[105] H. Hu, B. Zhao, M.E. Itkis, R.C. Haddon, Nitric Acid Purification of Single-Walled Carbon Nanotubes, Journal of Physical Chemistry B. 107 (2003) 13838–13842. https://doi.org/10.1021/jp035719i.
[106] M.T. Martínez, M.A. Callejas, A.M. Benito, W.K. Maser, M. Cochet, J.M. Andrés, J. Schreiber, O. Chauvet, J.L.G. Fierro, Microwave single walled carbon nanotubes purification, Chemical Communications. 9 (2002) 1000–1001. https://doi.org/10.1039/b201593e.
[107] P. Nikolaev, A. Thess, A.G. Rinzler, D.T. Colbert, R.E. Smalley, Diameter doubling of single-wall nanotubes, Chemical Physics Letters. 266 (1997) 422–426. https://doi.org/10.1016/S0009-2614(97)00053-5.
[108] A.G.S. Filho, A. Jorio, G.G. Samsonidze, G. Dresselhaus, R. Saito, M.S. Dresselhaus, Raman spectroscopy for probing chemically/physically induced phenomena in carbon nanotubes, Nanotechnology. 14 (2003) 1130–1139. https://doi.org/10.1088/0957-4484/14/10/311.
[109] J. Zhu, J.D. Kim, H. Peng, J.L. Margrave, V.N. Khabashesku, E. V. Barrera, Improving the dispersion and integration of single-walled carbon nanotubes in epoxy composites through functionalization, Nano Letters. 3 (2003) 1107–1113. https://doi.org/10.1021/nl0342489.
[110] Y.P. Sun, K.F. Fu, Y. Lin, W.J. Huang, Functionalized carbon nanotubes: Properties and applications, Acc. Chem. Res. 35 (2002) 1096–1104. https://doi.org/10.1021/er010160v.
[111] Z. Liu, S. Tabakman, K. Welsher, H. Dai, Carbon nanotubes in biology and medicine: In vitro and in vivo detection, imaging and drug delivery, Nano Research. 2 (2009) 85–120. https://doi.org/10.1007/s12274-009-9009-8.
[112] B. Arora, P. Attri, Carbon nanotubes (CNTs): A potential nanomaterial for water purification, Journal of Composites Science. 4 (2020) 1–20. https://doi.org/10.3390/jcs4030135.
[113] Z. Syrgiannis, M. Melchionna, M. Prato, Encyclopedia of Polymeric Nanomaterials, Springer Berlin Heidelberg, Berlin, Heidelberg, 2020. https://doi.org/10.1007/978-3-642-36199-9.
[114] W.A. Saidi, Functionalization of single-wall zigzag carbon nanotubes by carboxyl groups: Clustering effect, Journal of Physical Chemistry C. 117 (2013) 9864–9871. https://doi.org/10.1021/jp400903b.
[115] Z. Liu, K. Chen, C. Davis, S. Sherlock, Q. Cao, X. Chen, H. Dai, Drug delivery with carbon nanotubes for in vivo cancer treatment, Cancer Research. 68 (2008) 6652–6660. https://doi.org/10.1158/0008-5472.CAN-08-1468.
[116] M.S. Dresselhaus, G. Dresselhaus, Intercalation compounds of graphite, Advances in Physics. 51 (2002) 1–186. https://doi.org/10.1080/00018730110113644.
[117] Y.S. Li, J.L. Liao, S.Y. Wang, W.H. Chiang, Intercalation-assisted longitudinal unzipping of carbon nanotubes for green and scalable synthesis of graphene nanoribbons, Scientific Reports. 6 (2016) 1–12. https://doi.org/10.1038/srep22755.
[118] X. Devaux, B. Vigolo, E. McRae, F. Valsaque, N. Allali, V. Mamane, Y. Fort, A. V. Soldatov, M. Dossot, S.Y. Tsareva, Covalent Functionalization of HiPco Single-Walled Carbon Nanotubes: Differences in the Oxidizing Action of H 2 SO 4 and HNO 3 during a Soft Oxidation Process,

ChemPhysChem. 16 (2015) 2692–2701. https://doi.org/10.1002/cphc.201500248.
[119] V.T. Le, C.L. Ngo, Q.T. Le, T.T. Ngo, Surface modification and functionalization of carbon nanotube with some organic compounds, (n.d.) 4–9. https://doi.org/10.1088/2043-6262/4/3/035017.
[120] W. Zhou, S. Sasaki, A. Kawasaki, Effective control of nanodefects in multiwalled carbon nanotubes by acid treatment, Carbon. 78 (2014) 121–129. https://doi.org/10.1016/j.carbon.2014.06.055.
[121] F. Banoo, R. Stewart, Permanganate oxidation of aromatic alcohols in acid solution, Canadian Journal of Chemistry. 47 (1969) 3199–3205. https://doi.org/10.1139/v69-526.
[122] D. V. Kosynkin, A.L. Higginbotham, A. Sinitskii, J.R. Lomeda, A. Dimiev, B.K. Price, J.M. Tour, Longitudinal unzipping of carbon nanotubes to form graphene nanoribbons, Nature. 458 (2009) 872–876. https://doi.org/10.1038/nature07872.
[123] D.B. Shinde, M. Majumder, V.K. Pillai, Counter-ion Dependent, Longitudinal Unzipping of Multi-Walled Carbon Nanotubes to Highly Conductive and Transparent Graphene Nanoribbons, Scientific Reports. 4 (2015) 4363. https://doi.org/10.1038/srep04363.
[124] V. Ţucureanu, A. Matei, A.M. Avram, FTIR Spectroscopy for Carbon Family Study, Critical Reviews in Analytical Chemistry. 46 (2016) 502–520. https://doi.org/10.1080/10408347.2016.1157013.
[125] S. Hussain, P. Jha, A. Chouksey, R. Raman, S.S. Islam, T. Islam, P.. Choudhary, Spectroscopic Investigation of Modified Single Wall Carbon Nanotube (SWCNT), Journal of Modern Physics. 02 (2011) 538–543. https://doi.org/10.4236/jmp.2011.26063.
[126] A. Misra, P.K. Tyagi, M.K. Singh, D.S. Misra, FTIR studies of nitrogen doped carbon nanotubes, Diamond and Related Materials. 15 (2006) 385–388. https://doi.org/10.1016/j.diamond.2005.08.013.
[127] B. Lesiak, L. Kövér, J. Tóth, J. Zemek, P. Jiricek, A. Kromka, N. Rangam, C sp 2 /sp 3 hybridisations in carbon nanomaterials – XPS and (X)AES study, Applied Surface Science. 452 (2018) 223–231. https://doi.org/10.1016/j.apsusc.2018.04.269.
[128] J.R. Pels, F. Kapteijn, J.A. Moulijn, Q. Zhu, K.M. Thomas, Evolution of nitrogen functionalities in carbonaceous materials during pyrolysis, Carbon. 33 (1995) 1641–1653. https://doi.org/10.1016/0008-6223(95)00154-6.
[129] M.A. Atieh, O.Y. Bakather, B. Al-Tawbini, A.A. Bukhari, F.A. Abuilaiwi, M.B. Fettouhi, Characterization of carbon nanotubes by Raman spectroscopy, Bioinorganic Chemistry and Applications. 2010 (2010) 1–9. https://doi.org/10.1155/2010/603978.
[130] D. Zhou, S. Seraphin, Complex branching phenomena in the growth of carbon nanotubes, Chemical Physics Letters. 238 (1995) 286–289. https://doi.org/10.1016/0009-2614(95)00406-T.
[131] X. Devaux, B. Vigolo, E. McRae, F. Valsaque, N. Allali, V. Mamane, Y. Fort, A. V. Soldatov, M. Dossot, S.Y. Tsareva, Covalent Functionalization of HiPco Single-Walled Carbon Nanotubes: Differences in the Oxidizing Action of H2SO4 and HNO3 during a Soft Oxidation Process, ChemPhysChem. 16 (2015) 2692–2701. https://doi.org/10.1002/cphc.201500248.
[132] C.C. Ciobotaru, C.M. Damian, H. Iovu, Single-wall carbon nanotubes purification and oxidation, UPB Scientific Bulletin, Series B: Chemistry and Materials Science. 75 (2013) 55–66.
[133] O.A. Gurova, V.E. Arhipov, V.O. Koroteev, T.Y. Guselnikova, I.P. Asanov, O. V. Sedelnikova, A. V. Okotrub, Purification of Single-Walled Carbon Nanotubes Using Acid Treatment and Magnetic Separation, Physica Status Solidi (B). 256 (2019) 1800742. https://doi.org/10.1002/pssb.201800742.
[134] A. Suri, K.S. Coleman, The superiority of air oxidation over liquid-phase oxidative treatment in the purification of carbon nanotubes, Carbon. 49 (2011) 3031–3038. https://doi.org/10.1016/j.carbon.2011.03.023.
[135] V.S. Gangoli, M.A. Godwin, G. Reddy, R.K. Bradley, A.R. Barron, The State of HiPco Single-Walled Carbon Nanotubes in 2019, C — Journal of Carbon Research. 5 (2019) 65.

https://doi.org/10.3390/c5040065.
[136] S. Poulin, R. França, L. Moreau-Bélanger, E. Sacher, Confirmation of X-ray photoelectron spectroscopy peak attributions of nanoparticulate iron oxides, using symmetric peak component line shapes, Journal of Physical Chemistry C. 114 (2010) 10711–10718. https://doi.org/10.1021/jp100964x.
[137] M.T. Martínez, M.A. Callejas, A.M. Benito, M. Cochet, T. Seeger, A. Ansón, J. Schreiber, C. Gordon, C. Marhic, O. Chauvet, J.L.G. Fierro, W.K. Maser, Sensitivity of single wall carbon nanotubes to oxidative processing: Structural modification, intercalation and functionalisation, Carbon. 41 (2003) 2247–2256. https://doi.org/10.1016/S0008-6223(03)00250-1.
[138] G.Q. Yu, S.H. Lee, J.J. Lee, Effects of thermal annealing on amorphous carbon nitride films by r.f. PECVD, Diamond and Related Materials. (2002). https://doi.org/10.1016/S0925-9635(02)00111-5.
[139] Y. Stubrov, A. Nikolenko, V. Gubanov, V. Strelchuk, Manifestation of Structure of Electron Bands in Double-Resonant Raman Spectra of Single-Walled Carbon Nanotubes, Nanoscale Research Letters. 11 (2016) 2. https://doi.org/10.1186/s11671-015-1213-8.
[140] R. Siddheswaran, D. Manikandan, R.E. Avila, C.E. Jeyanthi, R.V. Mangalaraja, Formation of carbon nanotube forest over spin-coated Fe2O 3 reduced thin-film by chemical vapor deposition, Fullerenes Nanotubes and Carbon Nanostructures. 23 (2015) 392–398. https://doi.org/10.1080/1536383X.2013.866945.
[141] J.E. Ellis, A. Star, Carbon Nanotube Based Gas Sensors toward Breath Analysis, ChemPlusChem. 81 (2016) 1248–1265. https://doi.org/10.1002/cplu.201600478.
[142] K. Hata, Water-Assisted Highly Efficient Synthesis of Impurity-Free Single-Walled Carbon Nanotubes, Science. 306 (2004) 1362–1364. https://doi.org/10.1126/science.1104962.
[143] A. Martinez-Hernandez, C. Velasco-Santos, V. Castano, Carbon Nanotubes Composites: Processing, Grafting and Mechanical and Thermal Properties, Current Nanoscience. 6 (2010) 12–39. https://doi.org/10.2174/157341310790226270.
[144] B.D. Wood, J.S. Dyer, V.A. Thurgood, N.A. Tomlin, J.H. Lehman, T.C. Shen, Optical reflection and absorption of carbon nanotube forest films on substrates, Journal of Applied Physics. 118 (2015). https://doi.org/10.1063/1.4923390.
[145] R. Kavian, A. Vicenzo, M. Bestetti, Growth of carbon nanotubes on aluminium foil for supercapacitors electrodes, Journal of Materials Science. 46 (2011) 1487–1493. https://doi.org/10.1007/s10853-010-4950-1.
[146] J.J. Butler, G.T. Georgiev, J.L. Tveekrem, M. Quijada, S. Getty, J.G. Hagopian, Initial studies of the bidirectional reflectance distribution function of carbon nanotube structures for stray light control applications, in: X. Xiong, C. Kim, H. Shimoda (Eds.), Earth Observing Missions and Sensors: Development, Implementation, and Characterization, 2010: p. 78620D. https://doi.org/10.1117/12.869569.
[147] F. Wang, The Optical Resonances in Carbon Nanotubes Arise from Excitons, Science. 308 (2005) 838–841. https://doi.org/10.1126/science.1110265.
[148] N.A. Tomlin, A.E. Curtin, M. White, J.H. Lehman, Decrease in reflectance of vertically-aligned carbon nanotubes after oxygen plasma treatment, Carbon. 74 (2014) 329–332. https://doi.org/10.1016/j.carbon.2014.03.040.
[149] A. Venkataraman, E.V. Amadi, Y. Chen, C. Papadopoulos, Carbon Nanotube Assembly and Integration for Applications, Nanoscale Research Letters. 14 (2019) 220. https://doi.org/10.1186/s11671-019-3046-3.
[150] H. Kuzmany, A. Kukovecz, F. Simon, M. Holzweber, C. Kramberger, T. Pichler, Functionalization of carbon nanotubes, 141 (2004) 113–122. https://doi.org/10.1016/j.synthmet.2003.08.018.
[151] Y. Xing, L. Li, C.C. Chusuei, R. V. Hull, Sonochemical oxidation of multiwalled carbon nanotubes, Langmuir. 21 (2005) 4185–4190. https://doi.org/10.1021/la047268e.

[152] W. Francisco, F.V. Ferreira, E.V. Ferreira, L. de S. Cividanes, A. dos R. Coutinho, G.P. Thim, Functionalization of multi-walled carbon nanotube and mechanical property of epoxy-based nanocomposite, Journal of Aerospace Technology and Management. 7 (2015) 289–293. https://doi.org/10.5028/jatm.v7i3.485.
[153] K.C. Chang, W.F. Ji, M.C. Lai, Y.R. Hsiao, C.H. Hsu, T.L. Chuang, Y. Wei, J.M. Yeh, W.R. Liu, Synergistic effects of hydrophobicity and gas barrier properties on the anticorrosion property of PMMA nanocomposite coatings embedded with graphene nanosheets, Polymer Chemistry. 5 (2014) 1049–1056. https://doi.org/10.1039/c3py01178j.
[154] R. Maiti, A. Midya, C. Narayana, S.K. Ray, Tunable optical properties of graphene oxide by tailoring the oxygen functionalities using infrared irradiation, Nanotechnology. 25 (2014) 495704. https://doi.org/10.1088/0957-4484/25/49/495704.
[155] W. Sun, Z. Liu, C. Jiang, Y. Xue, W. Chu, X. Zhao, Experimental and theoretical investigation on the interaction between palladium nanoparticles and functionalized carbon nanotubes for Heck synthesis, Catalysis Today. 212 (2013) 206–214. https://doi.org/10.1016/j.cattod.2012.09.024.
[156] Z. Yang, H. Peng, W. Wang, T. Liu, Crystallization behavior of poly(ε-caprolactone)/layered double hydroxide nanocomposites, Journal of Applied Polymer Science. 116 (2010) 2658–2667. https://doi.org/10.1002/app.
[157] G. Zhou, D.W. Wang, L.C. Yin, N. Li, F. Li, H.M. Cheng, Oxygen bridges between nio nanosheets and graphene for improvement of lithium storage, ACS Nano. 6 (2012) 3214–3223. https://doi.org/10.1021/nn300098m.
[158] E. Desimoni, G.I. Casella, A. Morone, A.M. Salvi, XPS determination of oxygen-containing functional groups on carbon-fibre surfaces and the cleaning of these surfaces, Surface and Interface Analysis. 15 (1990) 627–634. https://doi.org/10.1002/sia.740151011.
[159] Y.J. Xu, R. Arrigo, X. Liu, D.S. Su, Characterization and use of functionalized carbon nanotubes for the adsorption of heavy metal anions, Xinxing Tan Cailiao/New Carbon Materials. 26 (2011) 57–62. https://doi.org/10.1016/S1872-5805(11)60066-8.
[160] J. Lomon, P. Chaiyabin, T. Saisopa, K. Seawsakul, N. Saowiang, K. Promsakha, P. Poolcharuansin, N. Pasaja, A. Chingsungnoen, R. Supruangnet, N. Chanlek, H. Nakajima, P. Songsiriritthigul, XPS and XAS preliminary studies of diamond-like carbon films prepared by HiPIMS technique, Journal of Physics: Conference Series. 1144 (2018). https://doi.org/10.1088/1742-6596/1144/1/012048.
[161] J. V. Rojas, M. Toro-Gonzalez, M.C. Molina-Higgins, C.E. Castano, Facile radiolytic synthesis of ruthenium nanoparticles on graphene oxide and carbon nanotubes, Materials Science and Engineering B: Solid-State Materials for Advanced Technology. 205 (2016) 28–35. https://doi.org/10.1016/j.mseb.2015.12.005.
[162] H. Maachou, M.J. Genet, D. Aliouche, C.C. Dupont-Gillain, P.G. Rouxhet, XPS analysis of chitosan-hydroxyapatite biomaterials: From elements to compounds, Surface and Interface Analysis. 45 (2013) 1088–1097. https://doi.org/10.1002/sia.5229.
[163] G. Beshkov, D.B. Dimitrov, S. Georgiev, D. Juan-Cheng, P. Petrov, N. Velchev, V. Krastev, XPS spectra of thin CNx films prepared by chemical vapor deposition, Diamond and Related Materials. 8 (1999) 591–594. https://doi.org/10.1016/s0925-9635(98)00269-6.
[164] S. Li, X. Song, X. Kuai, W. Zhu, K. Tian, X. Li, M. Chen, S. Chou, J. Zhao, L. Gao, A nanoarchitectured Na6Fe5(SO4)8/CNTs cathode for building a low-cost 3.6 v sodium-ion full battery with superior sodium storage, Journal of Materials Chemistry A. 7 (2019) 14656–14669. https://doi.org/10.1039/c9ta03089a.
[165] V. Duc Chinh, G. Speranza, C. Migliaresi, N. Van Chuc, V. Minh Tan, N.T. Phuong, Synthesis of Gold Nanoparticles Decorated with Multiwalled Carbon Nanotubes (Au-MWCNTs) via Cysteaminium Chloride Functionalization, Scientific Reports. 9 (2019) 1–9. https://doi.org/10.1038/s41598-019-42055-7.

[166] K. Artyushkova, P. Atanassov, X-Ray Photoelectron Spectroscopy for Characterization of Bionanocomposite Functional Materials for Energy-Harvesting Technologies, ChemPhysChem. 14 (2013) 2071–2080. https://doi.org/10.1002/cphc.201300037.
[167] A. Gharbi, T. Legigan, V. Humblot, S. Papot, J.M. Berjeaud, Surface functionalization by covalent immobilization of an innovative carvacrol derivative to avoid fungal biofilm formation, AMB Express. 5 (2015) 1–12. https://doi.org/10.1186/s13568-014-0091-2.
[168] R.F. Araújo, M.F. Proença, C.J. Silva, M.C. Paiva, S. Villar-Rodil, J.M.D. Tascón, The solvent effect on the sidewall functionalization of multi-walled carbon nanotubes with maleic anhydride, Carbon. 78 (2014) 401–414. https://doi.org/10.1016/j.carbon.2014.07.019.
[169] L.Z. Qin, Y.Z. Lin, Y.C. Dou, Y.J. Yang, K. Li, T. Li, F.T. Liu, Toward enhanced photocatalytic activity of graphite carbon nitride through rational design of noble metal-free dual cocatalysts, Nanoscale. 12 (2020) 13829–13837. https://doi.org/10.1039/c9nr10044j.
[170] Y.J. Tang, Y. Wang, X.L. Wang, S.L. Li, W. Huang, L.Z. Dong, C.H. Liu, Y.F. Li, Y.Q. Lan, Molybdenum Disulfide/Nitrogen-Doped Reduced Graphene Oxide Nanocomposite with Enlarged Interlayer Spacing for Electrocatalytic Hydrogen Evolution, Advanced Energy Materials. 6 (2016) 1–7. https://doi.org/10.1002/aenm.201600116.
[171] R.M. Allaf, I. V. Rivero, S.S. Spearman, L.J. Hope-Weeks, On the preparation of as-produced and purified single-walled carbon nanotube samples for standardized X-ray diffraction characterization, Materials Characterization. 62 (2011) 857–864. https://doi.org/10.1016/j.matchar.2011.06.005.
[172] S. Shukla, A. Jadaun, V. Arora, R.K. Sinha, N. Biyani, V.K. Jain, In vitro toxicity assessment of chitosan oligosaccharide coated iron oxide nanoparticles, Toxicology Reports. 2 (2015) 27–39. https://doi.org/10.1016/j.toxrep.2014.11.002.
[173] P. Liu, Modifications of carbon nanotubes with polymers, European Polymer Journal. 41 (2005) 2693–2703. https://doi.org/10.1016/j.eurpolymj.2005.05.017.
[174] P.N.H. Nakashima, The Crystallography of Aluminum and Its Alloys, in: Encyclopedia of Aluminum and Its Alloys, CRC Press, Boca Raton, 2019. https://doi.org/10.1201/9781351045636-140000245.
[175] B. Zheng, Z. Xu, C. Gao, Mass production of graphene nanoscrolls and their application in high rate performance supercapacitors, Nanoscale. 8 (2016) 1413–1420. https://doi.org/10.1039/C5NR07067H.
[176] Q.M. Li, M.X. Shi, Intermittent transformation between radial breathing and flexural vibration modes in a single-walled carbon nanotube, Proceedings of the Royal Society A: Mathematical, Physical and Engineering Sciences. 464 (2008) 1941–1953. https://doi.org/10.1098/rspa.2007.0253.
[177] M.B. Moraes, L. Cividanes, G. Thim, Synthesis of Graphene Oxide and Functionalized CNT Nanocomposites Based on Epoxy Resin, Journal of Aerospace Technology and Management. 10 (2018). https://doi.org/10.5028/jatm.v10.944.
[178] M. BURGHARD, Electronic and vibrational properties of chemically modified single-wall carbon nanotubes, Surface Science Reports. 58 (2005) 1–109. https://doi.org/10.1016/j.surfrep.2005.07.001.
[179] H.M. Park, K.H. Kim, S.H. Lee, D.H. Park, Y.K. Hong, J. Joo, Electrochemical polymerization of polypyrrole (PPy) and poly(3-hexylthiophene) (P3HT) using functionalized single-wall carbon nanotubes, Colloids and Surfaces A: Physicochemical and Engineering Aspects. 313–314 (2008) 72–76. https://doi.org/10.1016/j.colsurfa.2007.04.077.
[180] D. Roy, E. Angeles-Tactay, R.J.C. Brown, S.J. Spencer, T. Fry, T.A. Dunton, T. Young, M.J.T. Milton, Synthesis and Raman spectroscopic characterisation of carbon nanoscrolls, Chemical Physics Letters. 465 (2008) 254–257. https://doi.org/10.1016/j.cplett.2008.09.044.
[181] J.L. Bahr, J. Yang, D. V. Kosynkin, M.J. Bronikowski, R.E. Smalley, J.M. Tour, Functionalization of Carbon Nanotubes by Electrochemical Reduction of Aryl Diazonium Salts: A Bucky Paper

Electrode, Journal of the American Chemical Society. 123 (2001) 6536–6542. https://doi.org/10.1021/ja010462s.
[182] C.A. Mitchell, J.L. Bahr, S. Arepalli, J.M. Tour, R. Krishnamoorti, Dispersion of functionalized carbon nanotubes in polystyrene, Macromolecules. 35 (2002) 8825–8830. https://doi.org/10.1021/ma020890y.
[183] V.A. da Silva, M.C. Rezende, Effect of the Morphology and Structure on the Microwave Absorbing Properties of Multiwalled Carbon Nanotube Filled Epoxy Resin Nanocomposites, Materials Research. 21 (2018). https://doi.org/10.1590/1980-5373-mr-2017-0977.
[184] M.S. Dresselhaus, G. Dresselhaus, R. Saito, A. Jorio, Raman spectroscopy of carbon nanotubes, Physics Reports. 409 (2005) 47–99. https://doi.org/10.1016/j.physrep.2004.10.006.
[185] S.D.M. Brown, A. Jorio, P. Corio, M.S. Dresselhaus, G. Dresselhaus, R. Saito, K. Kneipp, Origin of the Breit-Wigner-Fano lineshape of the tangential G -band feature of metallic carbon nanotubes, Physical Review B. 63 (2001) 155414. https://doi.org/10.1103/PhysRevB.63.155414.
[186] D. Roy, M. Chhowalla, H. Wang, N. Sano, I. Alexandrou, T.W. Clyne, G.A.J. Amaratunga, Characterisation of carbon nano-onions using Raman spectroscopy, Chemical Physics Letters. 373 (2003) 52–56. https://doi.org/10.1016/S0009-2614(03)00523-2.
[187] D. Roy, M. Chhowalla, N. Hellgren, T.W. Clyne, G.A.J. Amaratunga, Probing carbon nanoparticles in CNx thin films using Raman spectroscopy, Physical Review B - Condensed Matter and Materials Physics. 70 (2004) 1–6. https://doi.org/10.1103/PhysRevB.70.035406.
[188] J.M. Benoit, J.P. Buisson, O. Chauvet, C. Godon, S. Lefrant, Low-frequency Raman studies of multiwalled carbon nanotubes: Experiments and theory, Physical Review B - Condensed Matter and Materials Physics. 66 (2002) 1–4. https://doi.org/10.1103/PhysRevB.66.073417.
[189] M.S. Dresselhaus, G. Dresselhaus, M. Hofmann, The big picture of Raman scattering in carbon nanotubes, Vibrational Spectroscopy. 45 (2007) 71–81. https://doi.org/10.1016/j.vibspec.2007.07.004.
[190] K.H. An, K.K. Jeon, J.M. Moon, S.J. Eum, C.W. Yang, G.S. Park, C.Y. Park, Y.H. Lee, Transformation of singlewalled carbon nanotubes to multiwalled carbon nanotubes and onion-like structures by nitric acid treatment, Synthetic Metals. 140 (2004) 1–8. https://doi.org/10.1016/S0379-6779(02)01254-7.
[191] S. Mondal, S. Ghosh, C.R. Raj, Unzipping of Single-Walled Carbon Nanotube for the Development of Electrocatalytically Active Hybrid Catalyst of Graphitic Carbon and Pd Nanoparticles, ACS Omega. 3 (2018) 622–630. https://doi.org/10.1021/acsomega.7b01913.
[192] X. Fan, Z. Peng, Y. Yang, H. Zhou, X. Guo, Atomic H-induced cutting and unzipping of single-walled carbon nanotube carpets with a teepee structure and their enhanced supercapacitor performance, Journal of Materials Chemistry A. 3 (2015) 10077–10084. https://doi.org/10.1039/c5ta01426c.
[193] L. Jiao, L. Zhang, X. Wang, G. Diankov, H. Dai, Narrow graphene nanoribbons from carbon nanotubes, Nature. 458 (2009) 877–880. https://doi.org/10.1038/nature07919.
[194] A.L. Elias, A.R. Botello-Méndez, D. Meneses-Rodríguez, V.J. González, D. Ramírez-González, L. Ci, E. Muñoz-Sandoval, P.M. Ajayan, H. Terrones, M. Terrones, Longitudinal cutting of pure and doped carbon nanotubes to form graphitic nanoribbons using metal clusters as nanoscalpels, Nano Letters. 10 (2010) 366–372. https://doi.org/10.1021/nl901631z.
[195] U.K. Parashar, S. Bhandari, R.K. Srivastava, D. Jariwala, A. Srivastava, Single step synthesis of graphene nanoribbons by catalyst particle size dependent cutting of multiwalled carbon nanotubes, Nanoscale. 3 (2011) 3876–3882. https://doi.org/10.1039/c1nr10483g.
[196] A.G. Cano-Márquez, F.J. Rodríguez-Macías, J. Campos-Delgado, C.G. Espinosa-González, F. Tristán-López, D. Ramírez-González, D.A. Cullen, D.J. Smith, M. Terrones, Y.I. Vega-Cantú, Ex-MWNTs: Graphene sheets and ribbons produced by lithium intercalation and exfoliation of carbon

nanotubes, Nano Letters. 9 (2009) 1527–1533. https://doi.org/10.1021/nl803585s.
[197] L. Xie, H. Wang, C. Jin, X. Wang, L. Jiao, K. Suenaga, H. Dai, Graphene nanoribbons from unzipped carbon nanotubes: Atomic structures, Raman spectroscopy, and electrical properties, Journal of the American Chemical Society. 133 (2011) 10394–10397. https://doi.org/10.1021/ja203860a.
[198] L. Jiao, X. Wang, G. Diankov, H. Wang, H. Dai, Facile synthesis of high-quality graphene nanoribbons, Nature Nanotechnology. 5 (2010) 321–325. https://doi.org/10.1038/nnano.2010.54.
[199] C. Bower, A. Kleinhammes, Y. Wu, O. Zhou, Intercalation and partial exfoliation of single-walled carbon nanotubes by nitric acid, Chemical Physics Letters. 288 (1998) 481–486. https://doi.org/10.1016/S0009-2614(98)00278-4.
[200] R.S. Lee, H.J. Kim, J.E. Fischer, A. Thess, R.E. Smalley, Conductivity enhancement in single-walled carbon nanotube bundles doped with K and Br, Nature. 388 (1997) 255–257. https://doi.org/10.1038/40822.
[201] D.B. Shinde, M. Majumder, V.K. Pillai, Counter-ion Dependent, Longitudinal Unzipping of Multi-Walled Carbon Nanotubes to Highly Conductive and Transparent Graphene Nanoribbons, Scientific Reports. 4 (2015) 4363. https://doi.org/10.1038/srep04363.
[202] S.D. Silva-Santos, R.S. Alencar, A.L. Aguiar, Y.A. Kim, H. Muramatsu, M. Endo, N.P. Blanchard, A. San-Miguel, A.G. Souza Filho, From high pressure radial collapse to graphene ribbon formation in triple-wall carbon nanotubes, Carbon. 141 (2019) 568–579. https://doi.org/10.1016/j.carbon.2018.09.076.
[203] M. Terrones, H. Terrones, F. Banhart, J.C. Charlier, P.M. Ajayan, Coalescence of single-walled carbon nanotubes, Science. 288 (2000) 1226–1229. https://doi.org/10.1126/science.288.5469.1226.
[204] Y.A. Kim, H. Muramatsu, T. Hayashi, M. Endo, M. Terrones, M.S. Dresselhaus, Thermal stability and structural changes of double-walled carbon nanotubes by heat treatment, Chemical Physics Letters. 398 (2004) 87–92. https://doi.org/10.1016/j.cplett.2004.09.024.
[205] M.J. López, A. Rubio, J.A. Alonso, S. Lefrant, K. Méténier, S. Bonnamy, Patching and Tearing Single-Wall Carbon-Nanotube Ropes into Multiwall Carbon Nanotubes, Physical Review Letters. 89 (2002) 255501. https://doi.org/10.1103/PhysRevLett.89.255501.
[206] H. Zhang, M. Zhao, T. He, X. Zhang, Z. Wang, Z. Xi, S. Yan, X. Liu, Y. Xia, L. Mei, Orientation-selective unzipping of carbon nanotubes, Physical Chemistry Chemical Physics. 12 (2010) 13674–13680. https://doi.org/10.1039/c002719g.
[207] S.M. Lee, E. Kim, C. Kim, Unzipping of single-walled carbon nanotubes: A tight-binding molecular-dynamics study, Journal of the Korean Physical Society. 54 (2009) 682–686. https://doi.org/10.3938/jkps.54.682.
[208] H. Jantoljak, J.-P. Salvetat, L. Forró, C. Thomsen, Low-energy Raman-active phonons of multiwalled carbon nanotubes, Applied Physics A: Materials Science & Processing. 67 (1998) 113–116. https://doi.org/10.1007/s003390050746.
[209] H. Hu, P. Bhowmik, B. Zhao, M.. Hamon, M.. Itkis, R.. Haddon, Determination of the acidic sites of purified single-walled carbon nanotubes by acid–base titration, Chemical Physics Letters. 345 (2001) 25–28. https://doi.org/10.1016/S0009-2614(01)00851-X.
[210] A. Gromov, S. Dittmer, J. Svensson, O.A. Nerushev, S.A. Perez-García, L. Licea-Jiménez, R. Rychwalski, E.E.B. Campbell, Covalent amino-functionalisation of single-wall carbon nanotubes, Journal of Materials Chemistry. 15 (2005) 3334. https://doi.org/10.1039/b504282h.
[211] L.B. Ebert, Science of fullerenes and carbon nanotubes, Carbon. 35 (1997) 437–438. https://doi.org/10.1016/s0008-6223(97)89618-2.
[212] X. Shi, N.M. Pugno, H. Gao, Tunable core size of carbon nanoscrolls, Journal of Computational and Theoretical Nanoscience. 7 (2010) 517–521. https://doi.org/10.1166/jctn.2010.1387.
[213] G. Mpourmpakis, E. Tylianakis, G.E. Froudakis, Carbon nanoscrolls: A promising material for

hydrogen storage, Nano Letters. 7 (2007) 1893–1897. https://doi.org/10.1021/nl070530u.
[214] Z. Liu, J. Wang, H. Ding, S. Chen, X. Yu, B. Lu, Carbon Nanoscrolls for Aluminum Battery, ACS Nano. 12 (2018) 8456–8466. https://doi.org/10.1021/acsnano.8b03961.
[215] M. Shi, P. Nie, Z. Fan, R. Fu, S. Fang, H. Dou, X. Zhang, Tubular Graphene Nano-Scroll Coated Silicon for High Rate Performance Lithium-Ion Battery, Frontiers in Energy Research. 8 (2020). https://doi.org/10.3389/fenrg.2020.00002.
[216] T.S. Li, M.F. Lin, S.C. Chang, H.C. Chung, Optical excitations in carbon nanoscrolls, Physical Chemistry Chemical Physics. 13 (2011) 6138–6144. https://doi.org/10.1039/c0cp02097d.
[217] G. Carotenuto, A. Longo, S. De Nicola, C. Camerlingo, L. Nicolais, A simple mechanical technique to obtain carbon nanoscrolls from graphite nanoplatelets, Nanoscale Research Letters. 8 (2013) 403. https://doi.org/10.1186/1556-276X-8-403.
[218] S.F. Braga, V.R. Coluci, S.B. Legoas, R. Giro, D.S. Galvão, R.H. Baughman, Structure and Dynamics of Carbon Nanoscrolls, Nano Letters. 4 (2004) 881–884. https://doi.org/10.1021/nl0497272.
[219] H. Liu, T. Le, L. Zhang, M. Xu, Carbon nanoscrolls: synthesis and applications, Journal of Materials Science: Materials in Electronics. 29 (2018) 18891–18904. https://doi.org/10.1007/s10854-018-0074-1.
[220] X. Xie, L. Ju, X. Feng, Y. Sun, R. Zhou, K. Liu, S. Fan, Q. Li, K. Jiang, Controlled Fabrication of High-Quality Carbon Nanoscrolls from Monolayer Graphene, Nano Letters. 9 (2009) 2565–2570. https://doi.org/10.1021/nl900677y.
[221] J. Zheng, H. Liu, B. Wu, Y. Guo, T. Wu, G. Yu, Y. Liu, D. Zhu, Production of high-quality carbon nanoscrolls with microwave spark assistance in liquid nitrogen, Advanced Materials. 23 (2011) 2460–2463. https://doi.org/10.1002/adma.201004759.
[222] B. Tang, Z. Xiong, X. Yun, X. Wang, Rolling up graphene oxide sheets through solvent-induced self-assembly in dispersions, Nanoscale. 10 (2018) 4113–4122. https://doi.org/10.1039/c7nr08415c.
[223] B. Sajadi, S. van Hemert, B. Arash, P. Belardinelli, P.G. Steeneken, F. Alijani, Size- and temperature-dependent bending rigidity of graphene using modal analysis, Carbon. 139 (2018) 334–341. https://doi.org/10.1016/j.carbon.2018.06.066.
[224] D.B. Zhang, E. Akatyeva, T. Dumitric, Bending ultrathin graphene at the margins of continuum mechanics, Physical Review Letters. 106 (2011) 3–6. https://doi.org/10.1103/PhysRevLett.106.255503.
[225] N.G. Chopra, L.X. Benedict, V.H. Crespi, M.L. Cohen, S.G. Louie, A. Zettl, Fully collapsed carbon nanotubes, Nature. 377 (1995) 135–138. https://doi.org/10.1038/377135a0.
[226] X. Chen, C. Yi, C. Ke, Bending stiffness and interlayer shear modulus of few-layer graphene, Applied Physics Letters. 106 (2015). https://doi.org/10.1063/1.4915075.
[227] I. Nikiforov, E. Dontsova, R.D. James, T. Dumitrică, Tight-binding theory of graphene bending, Physical Review B - Condensed Matter and Materials Physics. 89 (2014) 1–13. https://doi.org/10.1103/PhysRevB.89.155437.
[228] D.W. Brenner, O.A. Shenderova, J.A. Harrison, S.J. Stuart, B. Ni, S.B. Sinnott, A second-generation reactive empirical bond order (REBO) potential energy expression for hydrocarbons, Journal of Physics Condensed Matter. 14 (2002) 783–802. https://doi.org/10.1088/0953-8984/14/4/312.
[229] Q. Wang, Simulations of the bending rigidity of graphene, Physics Letters, Section A: General, Atomic and Solid State Physics. 374 (2010) 1180–1183. https://doi.org/10.1016/j.physleta.2009.12.063.
[230] R. Nicklow, N. Wakabayashi, H.G. Smith, Lattice Dynamics of Pyrolytic Graphite, Physical Review B. 5 (1972) 4951–4962. https://doi.org/10.1103/PhysRevB.5.4951.
[231] M.J. Bronikowski, P.A. Willis, D.T. Colbert, K.A. Smith, R.E. Smalley, Gas-phase production of carbon single-walled nanotubes from carbon monoxide via the HiPco process: A parametric study,

Journal of Vacuum Science & Technology A: Vacuum, Surfaces, and Films. 19 (2001) 1800–1805. https://doi.org/10.1116/1.1380721.
[232] Q. Lu, M. Arroyo, R. Huang, Elastic bending modulus of monolayer graphene, Journal of Physics D: Applied Physics. 42 (2009) 102002. https://doi.org/10.1088/0022-3727/42/10/102002.
[233] K.N. Kudin, G.E. Scuseria, B.I. Yakobson, (formula presented) BN, and C nanoshell elasticity from ab initio computations, Physical Review B - Condensed Matter and Materials Physics. 64 (2001) 235406. https://doi.org/10.1103/PhysRevB.64.235406.
[234] P. Koskinen, O.O. Kit, Approximate modeling of spherical membranes, Physical Review B. 82 (2010) 235420. https://doi.org/10.1103/PhysRevB.82.235420.
[235] I.W. Chiang, B.E. Brinson, A.Y. Huang, P.A. Willis, M.J. Bronikowski, J.L. Margrave, R.E. Smalley, R.H. Hauge, Purification and characterization of single-wall carbon nanotubes (SWNTs) obtained from the gas-phase decomposition of CO (HiPco process), Journal of Physical Chemistry B. 105 (2001) 8297–8301. https://doi.org/10.1021/jp0114891.
[236] J.L. Li, K.N. Kudin, M.J. McAllister, R.K. Prud'homme, I.A. Aksay, R. Car, Oxygen-driven unzipping of graphitic materials, Physical Review Letters. 96 (2006) 5–8. https://doi.org/10.1103/PhysRevLett.96.176101.
[237] N. Berrada, A. Desforges, C. Bellouard, E. Flahaut, J. Gleize, J. Ghanbaja, B. Vigolo, Protecting Carbon Nanotubes from Oxidation for Selective Carbon Impurity Elimination, Journal of Physical Chemistry C. 123 (2019) 14725–14733. https://doi.org/10.1021/acs.jpcc.8b12554.
[238] W. Chen, H. Li, How Does Carbon Nanoring Deform to Spiral Induced by Carbon Nanotube?, Scientific Reports. 4 (2015) 3865. https://doi.org/10.1038/srep03865.
[239] C.H. Kiang, W.A. Goddard, R. Beyers, D.S. Bethune, Structural modification of single-layer carbon nanotubes with an electron beam, Journal of Physical Chemistry. 100 (1996) 3749–3752. https://doi.org/10.1021/jp952636w.
[240] L.X. Benedict, N.G. Chopra, M.L. Cohen, A. Zettl, S.G. Louie, V.H. Crespi, Microscopic determination of the interlayer binding energy in graphite, Chemical Physics Letters. 286 (1998) 490–496. https://doi.org/10.1016/S0009-2614(97)01466-8.
[241] M.F. Yu, M.J. Dyer, J. Chen, D. Qian, W.K. Liu, R.S. Ruoff, Locked twist in multiwalled carbon-nanotube ribbons, Physical Review B - Condensed Matter and Materials Physics. 64 (2001) 2414031–2414034. https://doi.org/10.1103/physrevb.64.241403.
[242] O.Y. Zhong-can, Z. Bin Su, C.L. Wang, Coil formation in multishell carbon nanotubes: Competition between curvature elasticity and interlayer adhesion, Physical Review Letters. 78 (1997) 4055–4058. https://doi.org/10.1103/PhysRevLett.78.4055.
[243] W. Clauss, D. Bergeron, A. Johnson, Atomic resolution STM imaging of a twisted single-wall carbon nanotube, Physical Review B - Condensed Matter and Materials Physics. 58 (1998) R4266–R4269. https://doi.org/10.1103/PhysRevB.58.R4266.
[244] Y.K. Kwon, D. Tománek, Orientational melting in carbon nanotube ropes, Physical Review Letters. 84 (2000) 1483–1486. https://doi.org/10.1103/PhysRevLett.84.1483.
[245] H. Inoue, T. Yoshiyama, M. Hada, D. Chujo, Y. Saito, T. Nishikawa, Y. Yamashita, W. Takarada, H. Matsumoto, Y. Hayashi, High-performance structure of a coil-shaped soft-actuator consisting of polymer threads and carbon nanotube yarns, AIP Advances. 8 (2018). https://doi.org/10.1063/1.5033487.
[246] O. Mykhailiv, H. Zubyk, M.E. Plonska-Brzezinska, Carbon nano-onions: Unique carbon nanostructures with fascinating properties and their potential applications, Inorganica Chimica Acta. 468 (2017) 49–66. https://doi.org/10.1016/j.ica.2017.07.021.
[247] N. Keller, N.I. Maksimova, V. V. Roddatis, M. Schur, G. Mestl, Y. V. Butenko, V.L. Kuznetsov, R. Schlögl, The catalytic use of onion-like carbon materials for styrene synthesis by oxidative dehydrogenation of ethylbenzene, Angewandte Chemie - International Edition. 41 (2002) 1885–

1888. https://doi.org/10.1002/1521-3773(20020603)41:11<1885::AID-ANIE1885>3.0.CO;2-5.
[248] N. Keller, N.I. Maksimova, V. V. Roddatis, M. Schur, G. Mestl, Y. V. Butenko, V.L. Kuznetsov, R. Schlögl, Zwiebelförmige Kohlenstoffe als Katalysatoren in der Styrolsynthese durch oxidative Dehydrierung von Ethylbenzol, Angewandte Chemie. 114 (2002) 1962. https://doi.org/10.1002/1521-3757(20020603)114:11<1962::aid-ange1962>3.0.co;2-r.
[249] N. Sano, H. Wang, I. Alexandrou, M. Chhowalla, K.B.K. Teo, G.A.J. Amaratunga, K. Iimura, Properties of carbon onions produced by an arc discharge in water, Journal of Applied Physics. 92 (2002) 2783–2788. https://doi.org/10.1063/1.1498884.
[250] C.T. Cioffi, A. Palkar, F. Melin, A. Kumbhar, L. Echegoyen, M. Melle-Franco, F. Zerbetto, G.M.A. Rahman, C. Ehli, V. Sgobba, D.M. Guldi, M. Prato, A Carbon nano-onion-ferrocene donor-acceptor system: Synthesis, characterization and properties, Chemistry - A European Journal. 15 (2009) 4419–4427. https://doi.org/10.1002/chem.200801818.
[251] B. Pradhan, K. Setyowati, H. Liu, D.H. Waldeck, J. Chen, Carbon nanotube-polymer nanocomposite infrared sensor, Nano Letters. 8 (2008) 1142–1146. https://doi.org/10.1021/nl0732880.
[252] M. Terrones, H. Terrones, F. Banhart, J.-C. Charlier, P.M. Ajayan, Coalescence of Single-Walled Carbon Nanotubes, Science. 288 (2000) 1226–1229. https://doi.org/10.1126/science.288.5469.1226.
[253] M.J. López, A. Rubio, J.A. Alonso, Deformations and thermal stability of carbon nanotube ropes, IEEE Transactions on Nanotechnology. 3 (2004) 230–236. https://doi.org/10.1109/TNANO.2004.828522.
[254] K. Méténier, S. Bonnamy, F. Béguin, C. Journetb, P. Bernier, M. Lamy de La Chapelle, O. Chauvet, S. Lefrant, Coalescence of single-walled carbon nanotubes and formation of multi-walled carbon nanotubes under high-temperature treatments, Science. 288 (2000) 1226–1229. https://doi.org/10.1126/science.288.5469.1226.
[255] L.M. Ericson, H. Fan, H. Peng, V.A. Davis, W. Zhou, J. Sulpizio, Y. Wang, R. Booker, J. Vavro, C. Guthy, A.N.G. Parra-Vasquez, M.J. Kim, S. Ramesh, R.K. Saini, C. Kittrell, G. Lavin, H. Schmidt, W.W. Adams, W.E. Billups, M. Pasquali, W.F. Hwang, R.H. Hauge, J.E. Fischer, R.E. Smalley, Macroscopic, neat, single-walled carbon nanotube fibers, Science. 305 (2004) 1447–1450. https://doi.org/10.1126/science.1101398.
[256] S. Park, J. An, I. Jung, R.D. Piner, S.J. An, X. Li, A. Velamakanni, R.S. Ruoff, Colloidal suspensions of highly reduced graphene oxide in a wide variety of organic solvents, Nano Letters. 9 (2009) 1593–1597. https://doi.org/10.1021/nl803798y.
[257] M. Sathyan, M.K. Jayaraj, H. John, Rolling and unrolling of graphene sheets: Via in situ generation of superparamagnetic iron oxide nanoparticles, Physical Chemistry Chemical Physics. 21 (2019) 16413–16417. https://doi.org/10.1039/c9cp01507h.
[258] S.P. Koenig, N.G. Boddeti, M.L. Dunn, J.S. Bunch, Ultrastrong adhesion of graphene membranes, Nature Nanotechnology. 6 (2011) 543–546. https://doi.org/10.1038/nnano.2011.123.
[259] C. Bartlam, S. Morsch, K.W.J. Heard, P. Quayle, S.G. Yeates, A. Vijayaraghavan, Nanoscale infrared identification and mapping of chemical functional groups on graphene, Carbon. 139 (2018) 317–324. https://doi.org/10.1016/j.carbon.2018.06.061.
[260] V. Georgakilas, M. Otyepka, A.B. Bourlinos, V. Chandra, N. Kim, K.C. Kemp, P. Hobza, R. Zboril, K.S. Kim, Functionalization of graphene: Covalent and non-covalent approaches, derivatives and applications, Chemical Reviews. 112 (2012) 6156–6214. https://doi.org/10.1021/cr3000412.
[261] S. Zhu, T. Li, Hydrogenation enabled scrolling of graphene, Journal of Physics D: Applied Physics. 46 (2013) 075301. https://doi.org/10.1088/0022-3727/46/7/075301.
[262] X. Sun, Z. Liu, K. Welsher, J.T. Robinson, A. Goodwin, S. Zaric, H. Dai, Nano-graphene oxide for cellular imaging and drug delivery, Nano Research. 1 (2008) 203–212. https://doi.org/10.1007/s12274-008-8021-8.

[263] Y.K. Kim, D.H. Min, Preparation of scrolled graphene oxides with multi-walled carbon nanotube templates, Carbon. 48 (2010) 4283–4288. https://doi.org/10.1016/j.carbon.2010.07.039.
[264] L. Gao, Z. Zhang, J. Zhao, J. Zhou, Z. Miao, W. Si, S. Zhuo, Controllable synthesis of graphene scrolls and their performance for supercapacitors, RSC Advances. 8 (2018) 19164–19170. https://doi.org/10.1039/C8RA02231C.
[265] Y.P. Gao, Z.B. Zhai, K.J. Huang, Y.Y. Zhang, Energy storage applications of biomass-derived carbon materials: Batteries and supercapacitors, New Journal of Chemistry. 41 (2017) 11456–11470. https://doi.org/10.1039/c7nj02580g.
[266] A. Aqel, K.M.M.A. El-Nour, R.A.A. Ammar, A. Al-Warthan, Carbon nanotubes, science and technology part (I) structure, synthesis and characterisation, Arabian Journal of Chemistry. 5 (2012) 1–23. https://doi.org/10.1016/j.arabjc.2010.08.022.
[267] K. Hata, D.N. Futaba, K. Mizuno, T. Namai, M. Yumura, S. Iijima, Water-assisted highly efficient synthesis of impurity-free single-walled carbon nanotubes, Science. 306 (2004) 1362–1364. https://doi.org/10.1126/science.1104962.
[268] J.-C. Charlier, X. Blase, S. Roche, Electronic and transport properties of nanotubes, Reviews of Modern Physics. 79 (2007) 677–732. https://doi.org/10.1103/RevModPhys.79.677.
[269] K. Balasubramanian, M. Burghard, Chemically Functionalized Carbon Nanotubes, Small. 1 (2005) 180–192. https://doi.org/10.1002/smll.200400118.
[270] K. Mizuno, J. Ishii, H. Kishida, Y. Hayamizu, S. Yasuda, D.N. Futaba, M. Yumura, K. Hata, A black body absorber from vertically aligned single-walled carbon nanotubes, Proceedings of the National Academy of Sciences of the United States of America. 106 (2009) 6044–6047. https://doi.org/10.1073/pnas.0900155106.
[271] Z.-P. Yang, L. Ci, J.A. Bur, S.-Y. Lin, P.M. Ajayan, Experimental Observation of an Extremely Dark Material Made By a Low-Density Nanotube Array, Nano Letters. 8 (2008) 446–451. https://doi.org/10.1021/nl072369t.
[272] W.H. Swartz, L.P. Dyrud, S.R. Lorentz, D.L. Wu, W.J. Wiscombe, S.J. Papadakis, P.M. Huang, E.L. Reynolds, A.W. Smith, D.M. Deglau, The RAVAN CubeSat mission: Advancing technologies for climate observation, in: International Geoscience and Remote Sensing Symposium (IGARSS), IEEE, 2015: pp. 5300–5303. https://doi.org/10.1109/IGARSS.2015.7327031.
[273] J. Lee, D.M. Lee, Y. Jung, J. Park, H.S. Lee, Y.K. Kim, C.R. Park, H.S. Jeong, S.M. Kim, Direct spinning and densification method for high-performance carbon nanotube fibers, Nature Communications. 10 (2019) 1–10. https://doi.org/10.1038/s41467-019-10998-0.
[274] G. Drozdov, I. Ostanin, H. Xu, Y. Wang, T. Dumitrică, A. Grebenko, A.P. Tsapenko, Y. Gladush, G. Ermolaev, V.S. Volkov, S. Eibl, U. Rüde, A.G. Nasibulin, Densification of single-walled carbon nanotube films: Mesoscopic distinct element method simulations and experimental validation, Journal of Applied Physics. 128 (2020) 184701. https://doi.org/10.1063/5.0025505.
[275] X. Yu, X. Zhang, J. Zou, Z. Lan, C. Jiang, J. Zhao, D. Zhang, M. Miao, Q. Li, Solvent-Tunable Microstructures of Aligned Carbon Nanotube Films, Advanced Materials Interfaces. 3 (2016) 1–6. https://doi.org/10.1002/admi.201600352.
[276] P.M. Ajayan, S. Lijima, Smallest carbon nanotube [6], Nature. 358 (1992) 23. https://doi.org/10.1038/358023a0.
[277] M. Majumder, C. Rendall, M. Li, N. Behabtu, J.A. Eukel, R.H. Hauge, H.K. Schmidt, M. Pasquali, Insights into the physics of spray coating of SWNT films, Chemical Engineering Science. 65 (2010) 2000–2008. https://doi.org/10.1016/j.ces.2009.11.042.
[278] R.M. Tromer, L.C. Felix, L.A. Ribeiro, D.S. Galvao, Optoelectronic properties of amorphous carbon-based nanotube and nanoscroll, Physica E: Low-Dimensional Systems and Nanostructures. 130 (2021) 114683. https://doi.org/10.1016/j.physe.2021.114683.
[279] F. Cheng, Y. Hu, Z. Lv, G. Chen, B. Yuan, X. Hu, Z. Huang, Directing helical CNT into chemically-

etched micro-channels on aluminum substrate for strong adhesive bonding with carbon fiber composites, Composites Part A: Applied Science and Manufacturing. 135 (2020) 105952. https://doi.org/10.1016/j.compositesa.2020.105952.

[280] J.G. Hagopian, S.A. Getty, M. Quijada, J. Tveekrem, R. Shiri, P. Roman, J. Butler, G. Georgiev, J. Livas, C. Hunt, A. Maldonado, S. Talapatra, X. Zhang, S.J. Papadakis, A.H. Monica, D. Deglau, Multiwalled carbon nanotubes for stray light suppression in space flight instruments, in: D. Pribat, Y.-H. Lee, M. Razeghi (Eds.), Carbon Nanotubes, Graphene, and Associated Devices III, 2010: p. 77610F. https://doi.org/10.1117/12.864386.

List of Publications

Peer Reviewed International Journal

1. **S. Saini**, S. Reshmi, G.M. Gouda, A. Kumar S., S. K. V., K. Bhattacharjee, 'Low reflectance of carbon nanotube and nanoscroll-based thin film coatings: a case study, **Nanoscale Advances**. (**2021**) 3, 3184–3198. **https://doi.org/10.1039/d0na01058h.**

2. **S. Saini**, S. Reshmi, G.M. Gouda, K. Bhattacharjee 'Emergence of carbon nanoscrolls from single walled carbon nanotubes: an oxidative route', **Physical Chemistry Chemical Physics**. (**2021**), 23, 27437–27448, **https://doi.org/10.1039/D1CP03945H.**

3. S. Reshmi., M. Mohan, **S. Saini**, A Roy, K Bhattacharjee 'Intermediate Cu-O-Si phase in the Cu-SiO_2/Si (111) system: growth, elemental and electrical studies'**, ACS Omega.** (**2021**) 6, 23826–23836, **https://doi.org/10.1021/acsomega.1c02646.**

Submitted

1. **S. Saini**, K. Bhattacharjee and G.M. Gouda, 'Electrical nature of randomly oriented low dimensional structural hybrids of carbon, submitted in **Diamond and Related Materials, 2023**.

Article in Physics Magazine

1. **S. Saini**, G.M. Gouda and K. Bhattacharjee, 'Thin films of 1D, 2D carbon hybrids for stray light control space applications', '**Physics News**' Bulletin of **Indian Physics Association** (**IPA**), **Volume 53, page no 10-13, ISSN: 0253 – 7583,** January-June **2023**.

Conference Proceedings

1. **S. Saini**, K. Bhattacharjee, S Reshmi and G. M. Gouda, 'Fe nanoparticles as catalytic scissors to unzip carbon nanotubes', **accepted**, 66th **DAE (Department of Atomic Energy)** Solid State Physics Symposium, Gandhi Institute of Technology and Management (GITAM) Visakhapatnam, Andhra Pradesh, India, 20-24 December **2023**.

2. **S. Saini**, K. Bhattacharjee and G. M. Gouda, 'Switching behavior of the composite low dimensional structural hybrids of carbon after UV exposure' **accepted,** '**IOP Conference Series: Materials Science and Engineering**', 3rd International conference on Physics of Materials and Nanotechnology (**ICPN**) held during 21-23 September **2023, Mangalore University**.

3. **S. Saini**, S. Reshmi, G. M. Gouda and K. Bhattacharjee, 'Structure assigned optical transitions from single walled carbon nanotube based high absorber composite thin film coatings' 1221 (**2022**) 012042 in '**IOP Conference Series: Materials Science and Engineering**', 2nd International E-conference on Physics of Materials and Nanotechnology (**ICPN**). **Doi:10.1088/1757-899X/1221/1/012042**.

4. **S. Saini**, G.M. Gouda and K. Bhattacharjee, 'Low Dimensional Structural Derivatives of Carbon from HiPCO SWCNTs', in proceedings of the 66th **DAE (Department of Atomic Energy)** Solid State Physics Symposium **Volume (56) 2022**, **page no. 142-144**.

5. **S. Saini**, S. Reshmi, G.M. Gouda and K. Bhattacharjee, 'Correlation between absorption features and optical transitions from SWCNT based thin film coatings', in proceedings of the 65th **DAE (Department of Atomic Energy)** Solid State Physics Symposium **Volume (55) 2021**, **page no. 209-10**, **ISBN No: 81-8372-085-4**.

Award

1. **Best Paper Oral Presentation Award,** received in the **4th ISSE National Conference** (INAC-4) – 2019 on Systems for Transforming India: Challenges & Opportunities; paper titled '*Single walled carbon nanotubes high absorber coatings for space applications'* conference to be held at SAC-ISRO, Ahmedabad during 26-27 September **2019**.

Conferences

1. Poster presentation in the 67th Department of Atomic Energy (**DAE)** Solid State Physics Symposium organized by Bhabha Atomic Research Centre (**BARC**), Government of India at Gandhi Institute of Technology and Management (**GITAM**), Vishakhapatnam, India, during 20-24 December **2023**.

2. Actively participated in the 1st Workshop on Density Functional Theory Modelling of Materials (**DFT-M**) organized by the Centre for Advanced Computational Studies, Delhi via Online Mode from 12-18 October **2023**.

3. Poster presentation in the 3rd International Conference on Physics of Materials and Nanotechnology (**ICPN**) Organized by Department of Physics, Mangalore University, India, on September 21-23, **2023**.

4. Attended **1**st International conference on Spacecraft Mission Operations (**SMOPS**) Bangaluru India, June 8th-9th **2023**.

5. Poster presentation in the 1st National Conference on Advances in Low-dimensional Materials for Optoelectronic and Nano Devices (**ALMOND**); organized by Institute of Physics (**IOP**), Bhubaneswar, India, on 3-5 March **2023**.

6. Poster presentation on 'Thin film coatings of low dimensional functional derivatives of carbon from HiPCO SWCNTs for stray light control space applications' in the Conference on Condensed Matter Physics (**CCMP**) organized by Physical Research Laboratory (**PRL**), Ahmedabad, India, 6-8 February **2023**.

7. Poster presentation in the 66th Department of Atomic Energy (**DAE)** Solid State Physics Symposium organized by Bhabha Atomic Research Centre (**BARC**), Government of India at Birla Institute of Technology (**BIT**), Mesra, India, during 18-22 December **2022**.

8. Selected for the Advanced Training Program (**ATP**) on '**Nanofabrication and Characterization Techniques in Gas Sensing module'** conducted by the Centre for

Nano Science and Engineering (**CeNSE**) at Indian Institute of Science (**IISc**), Bangalore from 15-25 November **2022**.

9. Oral presentation on 'Low reflectance of CNTs and CNS based thin film coatings for stray light control space applications' in conference 'Frontiers in Materials for Technological Applications (**FIMTA**)' organized by Institute of Minerals and Materials Technology (**IMMT**) (Regional Research Laboratory, Bhubaneswar, India) on 3-5 August **2022**.

10. Oral presentation on 'Low Dimensional Structural Derivatives of Carbon from Single Walled Carbon Nanotubes and Applications' in 'X-Ray and Ion-Scattering Methods for Materials Characterization' organized by Indian Institute of Technology, Bhubaneswar (**IITBBS**) and **DST-SERB** held at IITBBS, Odisha, India, during 13-20 June **2022**.

11. Poster presentation in the 1st International Conference on Thin Films and Nanotechnology - Knowledge, Leadership and Commercialization (**ICTN-KLC**) organized by IIT Delhi thin film department on 25 August **2021**.

12. Poster presentation in the International Conference 11th Bengaluru Nano India, March 2-4, **2020**.

13. Attended International Workshop on Advances in 2D Materials, Indian Institute of Science Education and Research (**IISER**), Thiruvananthapuram, India, 22-23 July **2019**.

14. Oral presentation on topic 'Single wall carbon nanotube spray coating: an initial study' in 3rd International Conference on Soft Materials, at Malaviya National Institute of Technology (**MNIT**) Jaipur, 09-14 December, **2018**.

15. Participated in workshop 'The Micro & Nano Fabrication Workshop' at Central Manufacturing Technology Institute (**CMTI**), Bangalore, 15 December **2017**.

16. Attended 3rd International Conference on Soft Materials, at Malaviya National Institute of Technology (MNIT) Jaipur, December, **2016**.